A Microfluidic-Based Microwave Interferometric Inductance Sensor Capable of Detecting Single Micron-Size Superparamagnetic Particles in Flow

by

Szymon Rzeszowski

A Thesis submitted to the Faculty of Graduate Studies of

The University of Manitoba

in partial fulfilment of the requirements of the degree of

MASTER OF SCIENCE

Department of Electrical & Computer Engineering

University of Manitoba

Winnipeg, Manitoba

Canada

UNIVERSITY OF MANITOBA

Faculty of Graduate Studies

Master's Thesis/Practicum Final Report

The undersigned certify that they have read the Master's Thesis/Practicum entitled:

A Microfluidic-Based Microwave Interferometric Inductance Sensor Capable of Detecting Single Micron-Size Superparamagnetic Particles in Flow

submitted by

Szymon Rzeszowski

in partial fulfillment of the requirements for the degree of

Master of Science, Electrical & Computer Engineering

The Thesis/Practicum Examining Committee certifies that the thesis/practicum (and oral examination if required) is:

APPROVED

(Approved or Not Approved)

[X] **Thesis** [ ] **Practicum**

Dr. G. Bridges, Dept. of Elec. & Comp. Eng., Advisor
(Advisor)

(Co-Advisor)

Dr. D. Oliver, Dept. of Elec. & Comp. Eng.
(Examining Committee member)

Dr. C.-M. Hu, Dept. of Physics & Astronomy
(Examining Committee member)

(Examining Committee member)

(Examining Committee member)

(External Examining Committee member)

Date: Thu, 05 May 2012

Abstract

A microfluidic-based inductance sensor operating at 1.5 GHz is presented that can detect single 4.5 μm superparamagnetic particles flowing in a microfluidic channel. The particles are detected as they pass over a micron-sized planar gold loop electrode, with a maximum signal-to-noise ratio of 26.3 dB for an 80 μm/s flow rate; the magnetic beads are simultaneously observed with microscope images. The sensor consists of a coupled-line resonator and microwave interferometric system coupled to the loop electrode that is integrated within a polydimethylsiloxane-on-glass microfluidic chip assembly. A time-averaged inductance change caused by a single particle is related to the real part of its magnetic Clausius-Mossotti factor. The effective real part of the magnetic permeability for a particular particle is estimated to be 1.13 at 1.5 GHz. The sensor detects magnetic particles in flow and does not require an external biasing magnetic field, which distinguishes it from other magnetic microparticle sensors.

Acknowledgements

I would first like to thank my advisor Greg Bridges for giving me the opportunity to work with him and for his invaluable help and guidance. I would also like to thank. Douglas Thompson, Graham Ferrier, Marija Nikolic-Jaric, Tim Cabel, and Sean Romanuik for their support and input throughout this project.

I thank Jun Hui for his contribution in the microfabrication of the gold electrodes; Dwayne Chrusch for his help in the microfabrication process, Matt Pilapil and Aminur Rahman for their help with the electrochemical deposition of gold, James Dietrich for his continued guidance and for his help with resonator fabrication, Cory Smit for his help with machining various mechanical fixtures, as well as Francis Lin and Jing Li for their help with the fabrication of the PDMS microfluidic channels. I would also like to thank the technical staff in the department of Electrical and Computer Engineering for their continued help throughout this project.

I thank Manitoba Research and Innovation Fund, Canadian Institute for Advanced Research (CIFAR), the Natural Sciences and Engineering Research Council of Canada (NSERC), and CMC for their financial support.

Finally, I would like to thank my parents Wojtek Rzeszowski and Bozena Rzeszowska for their moral and financial support throughout my academic career, and my girlfriend Tess Spence-Sing for her constant support and help throughout my graduate studies.

Table of Contents

List of Figures vii

List of Tables xiii

List of Copyrighted Material for which Permission was Obtained xiv

Chapter 1: Introduction 1

1.1 Motivation for Single Magnetic Bead Detection 1

1.2 Magnetic Sensor Technologies 4

1.3 Magnetic Bead Inductance Change Sensor Work and Contribution Presented in this Thesis 9

1.4 Thesis Organization 10

Chapter 2: Superparamagnetic Beads 13

2.1 Superparamagnetic Bead Composition and Complex Magnetic Susceptibility 13

Chapter 3: Sensor Operation and Apparatus 21

3.1 Overview of Detection System 23

3.2 Fluid Suspension Injection and Control 28

Chapter 4: Induced Inductance Change 33

4.1 Solution of Laplace`s Equation for the Scalar Magnetic Potential Inside and Outside of a Homogeneous Magnetic Sphere, Subjected to a Uniform Sinusoidal Steady-State Magnetic Field 34

4.2 Inductance Change Caused by a Single Superparamagnetic Sphere 39

Chapter 5: Loop Electrode Design 45

5.1 Current Density and Maximum H Field 45

5.2 Comsol® Simulations for Loop Electrode Design 47
5.3 Comsol® Energy Simulations 51
5.4 Comsol® Simulations of Fabricated Electrodes 54

Chapter 6: Electrode and Microfluidic Chip Fabrication 59

6.1 Photolithography 59
6.2 Gold and Titanium Layer Etching 62
6.3 Electrochemical Deposition 62
6.4 PDMS Channel Mold Fabrication 66
6.5 Series Resistance of Fabricated Loop Electrodes 72

Chapter 7: Half-Wave Resonator Design and Fabrication.....75

7.1 Introduction 75
7.2 Theoretical Rate of Change of Phase with Inductance 77
7.3 Half-Wave Resonator Design 82
7.4 Half-Wave Resonator Fabrication and Measurement 90

Chapter 8: Single 4.5 µm Dynabead® Measurements and Results 94

8.1 Single 4.5 µm Dynabead® Detection Using Loop 1 94
8.2 Single 4.5 µm Dynabead® Detection Using Loop 2 101
8.3 Estimation of Sensor Sensitivity, Resolution, and the Real Part
of the Magnetic Permeability of a Single Bead 106

Chapter 9: Conclusion and Recommended Future Work 111

9.1 Conclusion 111
9.2 Recommended Future Work 112

References 114

List of Figures

Figure 1-1: *Positive isolation of cells using superparamagnetic Dynabeads®* 4

Figure 1-2: *Sandwich assay sensor. (A)Antibody molecules are grown on the sensor surface. (B)A passing target antigen will bind one of these antibodies. (C)Magnetic markers are then introduced and will bind to any antigens present on the sensor surface. Sensor output will be proportional to concentration of bound antigens.* 6

Figure 1-3: *Spin valve sensor thin-film stack (left). The bead is magnetized by a biasing field, and the stray field from the bead affects the free ferromagnetic layer, thereby causing a change in resistance. The resistance is a function of the free layer magnetization direction (right).* 8

Figure 2-1: *Mass magnetization (magnetization divided by 1600 kg/m^3 mass density) versus applied field, $\mu_0 H$, at room temperature for M-450 Dynabeads. Inset shows response to smaller magnitude fields. Measurement time was approximately 10 s [Fon05].* 15

Figure 2-2: *Normalized complex susceptibility as a function of frequency for different values of external polarizing magnetic field H. The sample consists of a suspension of maghemite particles, of meanradius 10 nm, in octane. The top, solid line represents the real part of the susceptibility without the presence of an external polarizing field [Fan06]* 20

Figure 3-1: *Figure 3-1: Sensor Operation. a) A coupled line resonator, whose centre line consists of a section of transmission line that is a half wavelength at the resonant frequency, is used to detect changes in load inductance of a planar gold loop electrode at the bottom of a microfluidic channel. As a single magnetic bead flows over the loop electrode, it becomes magnetized by the ac magnetic field, which is generated in the loop by a 1.5 GHz induced centre transmission line current. As the bead becomes magnetized, there is a resulting net change in stored magnetic energy, and therefore inductance, in the volume around the loop. b) Top and longitudinal section views of a 4.5 μm superparamagnetic bead flowing through a microfluidic channel above a planar gold loop electrode, and the resulting inductance change profile with horizontal bead position. The maximum change in inductance for a particular bead elevation occurs at the centre of the loop electrode.* 22

Figure 3-2: *Resonator transmission magnitude and phase response curves showing a resonant frequency shift due to a change in load inductance inside the channel for $\Delta L=0$ (black curves), and for ΔL (blue curves). At the original resonant frequency, f_{01}, the magnitude change due to a resonant frequency shift is negligible, whereas the change in phase, $\Delta\Phi$, is proportional to the slope of the phase response, $\partial\Phi/\partial f$, near the resonant frequency.* 23

Figure 3-3: *Microwave interferometer, resonant sensor, and microfluidic device. A 1.5 GHz signal is split between a reference path and a resonator path. Paths are 90° out of phase so that the mixer output is null in the absence of a magnetic bead. A Ground-Signal probe is used to terminate the resonator with a particular gold loop electrode, which is situated at the bottom of a microfluidic channel. As magnetic bead flows above a planar loop electrode, the load inductance changes, changing the transmission phase of the resonator. The mixer output is proportional to the change in transmission phase. The reference path is modulated at the same frequency as the lock-in-amplifier to filter out noise outside of a narrow bandwidth.* 24

Figure 3-4: *Microwave interferometer, resonant sensor, microfluidic device, and microscope located inside an EMI enclosure (left). Signal source, LIA, syringe apparatus, and computer interface (right).* 27

Figure 3-5: *Close-up of the microwave resonator and probe attached to an XYZ positioner. The microwave probe is used to touch down onto the desired electrode loop on the microfluidic chip. An LED light is reflected off of a metal surface to provide backlighting through the bottom of the channel, in addition to the light through the microscope lens.* 28

Figure 3-6: *Microfluidic Device. H-channel design used to control the fluid-flow direction and rate in the small cross channel (P_L to P_R), based on the altitude differential of two syringes. The suspension of magnetic beads is introduced into port P_1, and deionized water is introduced into P_4. Ports P_2 and P_3 are output ports that have their tubing placed in a beaker. Blue arrows represent fluid-flow direction, assuming that the pressure at P_1 is greater than at P_4.* 29

Figure 3-7: *Fluidic control set-up. Fluid-flow direction and rate is controlled by the differential altitude of two syringes. Solenoid clamps acting as valves at the output ports can be used to purge the channel of any remaining beads or to quickly fill the cross channel with the new sample suspension.* 30

Figure 3-8: *H-channel fluid flow schematic. R represents the resistance to flow between two points and P represents the pressure at a particular point. P_1 and P_4 represent the pressure at the two syringe fluid input points, whereas P_2 and P_3 represent the pressure at the output points inside the beaker.* 32

Figure 4-1: *A homogeneous magnetic sphere, centred at the origin, is subjected to a uniform sinusoidal steady-state magnetic field. The wavelength of the applied field is assumed to be much greater than the total volume radius.* 34

Figure 4-2: *The magnetic sphere occupies a volume V_{sphere} inside the solution volume V_{tot}.,and is assumed to be subjected to a uniform, sinusoidal steady-state magnetic field intensity $\bar{H}_0$.* 39

Figure 4-3: *A magnetic sphere located at (0, 0, z) is subjected to an approximately uniform magnetizing field, equal to $H_0(z, x = 0)e^{j\omega t}\bar{a}_z$over the volume of*

the sphere, which is generated by two infinite conductors situated symmetrically about the origin at $x=x_1$ and $x= -x_1$, carrying current I in opposite directions. 43

Figure 5-1: *A cross-sectional view of a 3D Comsol arrow plot of the normalized magnetic field density $\bar{B}_0$. At x=0, the applied field generated by current, I, is directed in the $\bar{a}_z$ direction, along the length of the loop electrode (far enough away from the ends of the loop).* 47

Figure 5-2: *Longitudinal section of channel. Geometry and boundary conditions used for 2D Comsol® quasi-statics perpendicular induction currents module simulations.* 48

Figure 5-3: *3D Comsol® Quasi-EM model used to simulate change in magnetic energy caused by the presence of a 2.25 µm sphere of relative magnetic permeability, $\mu_r = 1.2$.*.....52

Figure 5-4: *2D (left) and 3D (right) Comsol® models of magnetizing field variation at a constant 4.5 µm elevation above an electrode loop that is 5 µm wide, 1 µm thick, and spaced 5 µm apart.* 54

Figure 5-5: *Magnetizing field variation for constant elevations above the Loop 1 electrode due to a 0.25 mA current. The top curve and bottom curve represent the field variation at a 0.25 µm elevation and 4.5 µm elevation, respectively.* 55

Figure 5-6: *Magnetizing field variation for constant elevations above the Loop 2 Electrode due to a 0.25 mA current. The top curve and bottom curve represent the field variation at a 0.25 µm elevation and 4.5 µm elevation, respectively.* 56

Figure 5-7: *Inductance change profile for constant bead elevations. (a) Loop 1 inductance change profile for a bead with effective permeability, $\mu_r=1.2$. (b) Loop 2 inductance change profile for a bead with effective permeability, $\mu_r=1.2$. .* 58

Figure 6-1: *Planar gold electrode and PDMS channel mould fabrication steps (Dimensions are not to scale).* 61

Figure 6-2: *Electrochemical Deposition of Au. An Ag/AgCl reference electrode, Pt counter electrode, and Glass sample with Au electrode layer (working electrode) immersed in a beaker with Au solution. A bipotentiostat workstation was used to record and control the deposition speed and duration.*.....64

Figure 6-3: *Au electrode array. Electrochemical deposition of Au increased the thickness to approximately 1.1 µm. The connection bar shown at the bottom was later isolated using a wafer saw.*.....65

Figure 6-4: *Au electrode loop electrode. This loop is approximately 5µm wide, 110µm long (excluding the wider end portion at the top), with 7µm spacing (designed for 5 µm width and 10 µm spacing). The contact pads are 150µm wide.* 66

Figure 6-5: *PDMS channel design using L-edit CAD software. Four separate microfluidic channel designs lie inside a 3" Si wafer outline. Outer channels represent vacuum channels. Each design has a cut line used as a guide when cutting with a knife along the bottom cross-channel.* 67

Figure 6-6: *Fabricated PDMS mould reversibly bonded to a glass slide. Microfluidic channels are located at the bottom of the PDMS mould.* 69

Figure 6-7: *(a) Alignment of microfluidic channels with Au electrode loop array. (b) Fabricated PDMS mould reversibly bonded to a glass slide. Microfluidic channels are located at the bottom of the PDMS mould.* 71

Figure 6-8: *Loop 1(left electrode) and Loop 2 (right electrode) dimensions.*.....72

Figure 7-1: *Three broadside-coupled microstrip transmission lines (left). The centre microstrip line together with the SMA connector, GS probe, and Au electrode are a half-wavelength at the resonant frequency. A flowing magnetic bead changes the load inductance of the centre transmission line, causing a shift in resonant frequency.* 76

Figure 7-2: *The centre resonator line can be approximated by a transmission line terminated by a small series resistance and variable inductance (top). The centre line behaves like a series RLC resonator. The current is a maximum at the input and load end if the loop is approximated as a perfect short (bottom).* 77

Figure 7-3: *Three broadside-coupled microstrip transmission lines (left). Centre microstrip line together with the SMA connector, GS probe, and Au electrode are a half-wavelength at the resonant frequency. Spacing, S, determines the coupling between the centre line and the input and output lines, and affects the insertion loss. Length, L, affects the resonant frequency and, to a lesser extent, the insertion loss.* 83

Figure 7-4: *Half-wave coupled-line resonator model used for Ansoft Designer simulation.* 85

Figure 7-5: *Resonator simulation showing resonant frequency as a function of microstrip trace length L.* 88

Figure 7-6: *Resonator simulation showing effect of L on $20\log_{10}\|S21\|$ for various values of trace spacing, s.* 88

Figure 7-7: *Resonator simulation showing effect of L on resonator quality factor.* 89

Figure 7-8: *Resonator simulation comparing various design dimensions by the product |V2/V1| x Q.* 89

Figure 7-9: *Fabricated λ/2 resonator. 3 broadside-coupled microstrip transmission lines milled out on a 1/16" Cu-Clad TLX-9 Taconic Laminate board. Centre microstrip line together with the SMA connector, GS probe, and Au electrode (not shown) are a half-wavelength at the resonant frequency.* 87

Figure 7-10: *Power transmission response of measured resonator (terminated by Loop 1 and Loop 2) and simulated Ansoft model (R_L=2 Ω, and R_L =3 Ω).* 91

Figure 7-11: *Measured phase response of the resonator terminated by Loop 1 (green) and Loop 2 (red). The path length phase dependence has been subtracted from the phase response.* 92

Figure 8-1: *Signals due to 3 single 4.5 μm Dynabeads®. Average bead flow rate is 280 μm/s. The RMS noise is 20 mV for a 5 sec window between 6 s and 11 s.* 95

Figure 8-2: *Video snapshot of magnetic bead crossing events corresponding to beads A, B, and C from Fig. 8-1.*.....97

Figure 8-3: *Close-up of video snapshots showing the different colour and transparency of a magnetic Dynabead® (top two snapshots) compared to an aggregate of PSSs (two bottom snapshots). All PSSs look dark and opaque as they flow over the electrode loop, while the Dynabeads® look semi-transparent.*.....98

Figure 8-4: *155 mV signal due to 2 closely-spaced single 4.5 μm Dynabeads® followed by a 110 mV single due to a single 4.5 μm Dynabead®. Average bead flow rate is 80 μm/s.* The RMS noise is 20 mV for a 5 sec window between 5 s and 10 s. 99

Figure 8-5: *Video snapshots of bead crossing events corresponding to A and B in Fig. 8-4.* 100

Figure 8-6: *Signal due to a single 4.5 μm Dynabead®(top). Square of the magnetizing field above Loop 1 for an elevation of 2.5 μm (bottom), as simulated using Comsol (see Fig. 5-5). The shape of the signal follows the square of the magnetizing field above the loop.* 101

Figure 8-7: *Signals and video snapshot of two single 4.5 μm Dynabeads®. The 207 mV signal from the bead labeled B was the strongest signal obtained in this experiment, possibly due to its having a higher magnetization or due to the low elevation at which it was flowing (100 mV signals were also recorded, suggesting that some beads were flowing at higher elevations or had smaller effective magnetizations).* 103

Figure 8-8: *Video snapshots of a single PSS flowing near the electrode. PSSs did not produce any signals.* 104

Figure 8-9: *Signal and video snapshot of a 4.5 μm Dynabead® attached to a 6 μm PSS. The signal peak was 154mV with a flow rate of approximately 80 μm/s. The RMS noise was approximately 10 mV (for a 4 second window between 25 s and 29 s).*.....105

Figure 8-10: *Sensor schematic showing power levels and gains.* 107

List of Tables

Table 5-1: *Gold electrode loop dimensions and simulated maximum magnetizing field at an elevation of 2.5 μm above the loop electrode for a 250 μA current. Shaded region represents optimum dimensions.. .....*50

Table 7-1: *Ansoft Designer simulation results of the coupled-line resonator, for different spacing distances (S in Fig. 7-1) and different lengths (L in Fig. 7-1). *87

Table 7-2: *Power transmission response of measured resonator (terminated by Loop 1 and Loop 2) and simulated Ansoft model (R_L=2 Ω, and R_L =3 Ω). *92

List of Copyrighted Material for which Permission was Obtained

G. Fonnum, C. Johansson, A. Molteberg, S. Mørup, and E. Aksnes, “Characterization of Dynabeads by magnetization measurements and Mössbauer spectroscopy,” J. Magn. Magn.Mater., vol. 293, pp. 41-47, 2005.

Used as Figure 2-1 on page 15 of this thesis.

P.C. Fannin, L. Cohen-Tannoudji, E. Bertrand, A.T. Giannitsis, C. Mac Oireachtaigh, and J. Bibette “Investigation of the complex susceptibility of magnetic beads containing maghemite nanoparticles,” J. Magn. Magn.Mater., vol. 303, pp. 141-152, 2006.

Used as Figure 2-2 on page 20 of this thesis.

Chapter 1
Introduction

1.1 Motivation for Single Magnetic Bead Detection

When trying to identify the presence or concentration of a particular target analyte; such as a biological cell, bacteria, or protein; in a biological sample, a common approach is to use markers. A marker, or label, is a detectable particle or molecule that is target specific, and which attaches itself or enters the target analyte. Fluorescent particles, enzymes, radioisotopes, or magnetic beads, are all examples of markers that can be used as a means of tagging an analyte. The signal produced by the marker can then be used to count, separate, or transport the tagged analyte, making it possible to automate and scale down many biological laboratory functions that are normally performed manually, and at much larger sample volumes. In order to make the detection specific to a particular type of analyte, each marker must have high affinity for a specific molecular site, called an epitope, which is present in the target analyte and not in the rest of the sample solution. One method is to coat each marker with molecules called antibodies. When mixed into a sample solution, the antibodies will bind to an epitope on the surface of a target analyte, called an antigen. This technique of detecting an analyte by means of antibody-antigen reactions is called an immunoassay [Wil05]. Applications for immunoassay sensors include medical research and diagnostics, environmental monitoring, food safety, bioterrorism prevention, and biological research [Per03].

Immunoassay sensors are developing in conjunction with the field of microfluidics. Microfluidics is a fast-growing, multidisciplinary field that involves the manipulation and control of fluids at the sub-millimeter scale [Gra93, Mit01]. By combining microfluidics and microelectromechanical systems (MEMS), the small-scale integration and automation of various laboratory processes onto a single chip or device, known as "lab-on-a-chip" [Mar09], can be made possible.

One type of immunoassay is a radioimmunoassay (RIA), which uses radioisotopes that can be used to detect small amounts of analyte. RIAs have been employed for many decades [Cur79], but the obvious problems with using radioactive materials for diagnostic purposes limit their usefulness. A fluorescent immunoassay (FIA) is a more commonly used technique that provides highly sensitive signals. One drawback of FIAs is that detection is achieved using optical equipment, which can be bulky and expensive to integrate with the microfluidic device.

A Magnetic immunoassay (MIA) is a method in immunology of detecting the presence or concentration of a target analyte by conjugating a magnetic marker with either the antigen or the antibody that forms the antigen-antibody pair in a sample mixture. The magnetic signal is then used as a means of detecting the analyte in the sample under test. MIAs lend themselves well to lab-on-a-chip technology because the magnetic markers can be manipulated and detected on-chip, without the need for expensive and bulky optical equipment. Once the target analyte is bound to a magnetic marker, it can be precisely moved using on-chip magnetic fields [Pam04, Ton01].

Magnetic markers that are spherical and monodisperse are called magnetic beads. They are usually composed of nanoparticles of iron-oxide. Due to the small size of the

individual nanoparticles (2nm-10nm), thermal energy at room temperature is high enough to randomly flip their magnetic moment. The matrix of nanoparticles inside the bead, therefore, exhibits superparamagnetic behavior, which is described further in Chapter 2. Consequently, the beads have no magnetization in the absence of an applied field, thereby preventing clustering, and exhibit large magnetization in an applied field; the magnetization is many orders of magnitude larger than in paramagnetic materials. Magnetic beads provide good signal specificity when used as biological markers as there is little background magnetic noise in biological solutions. Superparamagnetic beads come in many sizes and are used for various applications. The beads can be coated (functionalized) with a specific molecule (ligand) such as a protein, antibody, antigen, or any molecule that shows high affinity towards a specific analyte. The sizes of the superparamagnetic microbeads range from less than 1 μm to 10 μm. For an example list of sizes, coatings, and detection methods of various magnetic microbeads, see [Hsi07].

Superparamagnetic microbeads are widely used for fast, reliable, and gentle isolation of biological cells, proteins, and other biomolecules from solution using a magnetic field [Saf99]. The 4.5 μm Dynabeads® used in this work are particularly suitable, for example, in the isolation, stimulation and expansion of T cells, while smaller 2.8 μm Dynabeads® are most suitable for isolating proteins [Neu07].

A typical bulk process for the positive isolation of cells using superparamagnetic beads is shown in Fig. 1-1. The beads are pre-coated with a suitable ligand for the target cell. A fluid sample is collected and mixed with a pre-coated bead solution. After a certain incubation period, the target cells will bind to the ligand-coated beads. The required incubation time varies depending on such factors as ligand concentration and

affinity, as well as sample volume and bead surface area. The bead-bound cells are then gently pulled towards a magnet, while the supernatant containing the rest of the sample is removed. The bead-bound cells are then re-suspended and ready for analysis. If desired, the cells can be detached from the magnetic beads by breaking the ligand-cell bond.

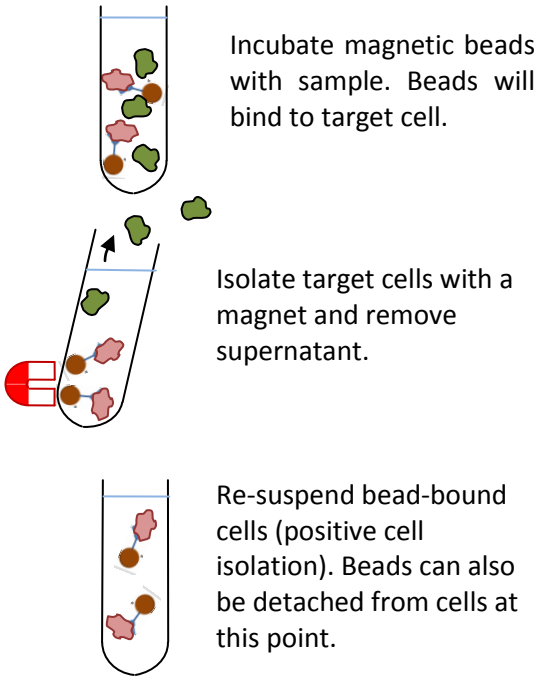

Figure 1-1: Positive isolation of cells using superparamagnetic Dynabeads®.

1.2 Magnetic Sensor Technologies

There are several techniques used for single or small volume magnetic particle detection. Various types of magnetic sensors that detect the presence of magnetic beads are presented in several reviews [Koh09, Tam08]. A magnetic relaxation switch is a type of magnetic sensor that uses superparamagnetic nanoparticles (NPs) or microparticles (MPs) as magnetic resonance contrast agents. As the NPs bind to a target analyte in solution, they aggregate around it, causing changes in transverse spin-spin relaxation

times, which are detected as changes in the MR contrast [Koh09, Ebe08]. The change in MR contrast can be related to the concentration of bound NPs, which in turn can be related to the concentration of analyte.

An inductive sensor is a type of magnetic sensor that uses an inductive coil to measure the concentration of many magnetic beads. Typically, antibodies are first grown on a solid-support surface located above an inductor. As a sample is introduced, the target analyte will flow over the sensor area and bind to the antibodies. Subsequently, magnetic beads flow over the sensor and will bind to another epitope site of the analyte to form a sandwich assay. An illustration of a sensor employing a sandwich assay is shown in Fig. 1-2. Any unbound beads will flow past the sensor and the remaining bead concentration will be proportional to the analyte concentration. Finally, the change in inductance of the coil is related to the concentration of target analyte.

Kiely et al. developed an inductive sandwich-assay sensor that measured an induction signal that is proportional to the concentration of many beads bound to a solid-support surface [Kie07]. This sensor could detect 62.5 μg of magnetic beads (Seradyn Inc.) with a diameter of 0.824 μm. This translates to roughly 1.5×10^8 beads, assuming a 1.4 g/cm^3 density for each bead. Nikitin et al. developed inductive sandwich-assay sensors that detected concentrations of magnetic beads at two measurement frequencies, attaining a sensitivity of approximately 100, 2.8 μm diameter, Dynabeads® [Nik07].

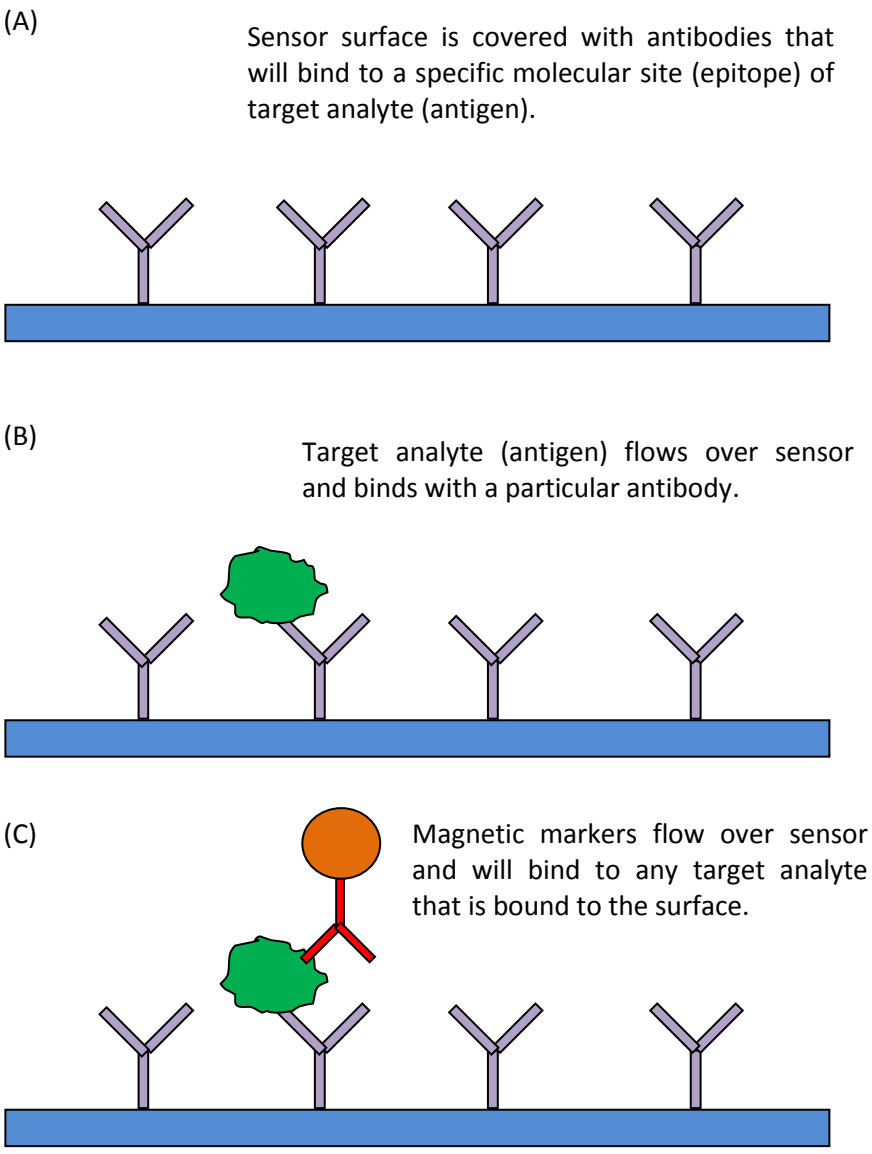

Figure 1-2: Sandwich assay sensor. (A)Antibody molecules are grown on the sensor surface. (B)A passing target antigen will bind one of these antibodies. (C) Magnetic markers are then introduced and will bind to any antigens present on the sensor surface. Sensor output will be proportional to concentration of bound antigens.

Sensors with single-magnetic-bead-sensitivity mostly employ sandwich assays to determine the concentration of an analyte. There are several kinds of sensors that can detect single magnetic MPs. Superconducting quantum interference sensors (SQUID),

have been shown to detect single nanoparticles with an average diameter of 150 nm [Hao11]. Although they exhibit extremely high sensitivities, SQUID sensors require extensive cooling and are therefore not a good candidate for lab-on-a-chip applications. Hall-effect sensors are very sensitive sensors that can detect single magnetic MPs. However, these sensors are usually quite complex. Kazakova et al. demonstrated a micro-sized scanning Hall sensor [Kaz07], which can detect single magnetic MPs down to 1 μm in size. Hall-effect sensors that rely on thin-film spin valve stacks (explained below) have demonstrated sensitivities down to a single 150 nm diameter FePt nanobead [Kaz10]. Giant magnetoresistance (GMR) sensors [Tam08], which are based on hard disk drive technology, and a variation of GMR called spin valve sensors [Meg05], are very common magnetic sensors with high sensitivity. Both sensor types use thin films with alternating magnetic and non-magnetic layers. Spin valve sensors have a linear response to magnetization and can provide the direction of the magnetic moment as well as its magnitude. A typical spin valve layer stack is shown in Fig. 1-3. A spin valve stack has alternating magnetic and non-magnetic layers much like a GMR stack; however, a spin-valve stack employs an anti-ferromagnetic layer. The top of the stack consists of a free ferromagnetic layer in which the magnetic moment direction is changed by the stray field of a magnetic bead that is bound above the stack. The presence of a bead is detected as a change in resistance. The resistance approximately follows the curve shown in Fig. 1-3.

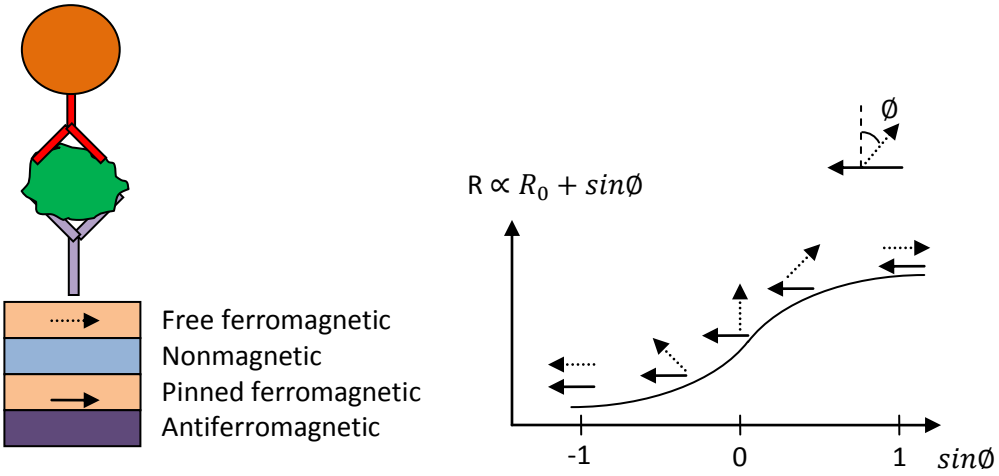

Figure 1-3: Spin valve sensor thin-film stack (left). The bead is magnetized by a biasing field, and the stray field from the bead affects the free ferromagnetic layer, thereby causing a change in resistance. The resistance is a function of the free layer magnetization direction (right).

A spin valve sensor [Lou09] was reported that detected beads flowing inside a microfluidic channel. The sensor detected single 2 µm Micromer-M beads flowing at cm/s velocities. The sensor required a large external magnetic biasing field (90 mT) to magnetize the particles and required post processing to extract the signal output information. Indeed, one of the drawbacks of GMR and spin-valve type sensors is that they require a large dc biasing magnetic field in order to magnetize each magnetic bead.

Single magnetic particle detection has been reported using embedded inductive coils [Du10]. The particles were detected in-flow, similar to the sensor presented in this thesis. However, the particles were large 50 to 100 µm iron particles and 125 µm copper particles immersed in an oil solution. A CMOS inductive coil frequency shift sensor [Wan09] was reported to be able to detect single 4.5 µm, 2.8 µm, and even 1 µm Dynabeads® captured onto a sensor surface. The sensor did not require an external

biasing magnetic field, but the signal was averaged for 90 seconds in order to detect the resonant frequency shift caused by the presence of the 1 μm beads. However, this sensor is not suited to in-flow detection of suspended particles.

1.3 Magnetic Bead Inductance Change Sensor and Contributions Presented in this Thesis

The inductance sensor presented in this thesis is designed to detect inductance changes caused by single superparamagnetic beads as they flow through a microfluidic channel. The advantages of this sensor are that it does not require an external biasing magnetic field, the microfabrication recipe is simple when compared to the thin-film stacks found in GMR and spin valve sensors, and the detection is done in-flow. Although the beads were not bound to any cells during detection, the sensor would operate by detecting bead-bound analytes in flow, thereby providing a means for automated counting or separation of analyte populations. The sensing electrode simply consists of a planar gold electrode loop bonded to a glass slide, making the embedded electrode simple to fabricate. Detection of single 4.5 μm Dynabeads® in-flow has been demonstrated with this prototype sensor.

The work done on the sensor has consisted of using an existing microwave interferometric system [Fer09], which was originally designed to detect capacitance changes, and modifying it to detect inductance changes caused by single 4.5 μm magnetic beads. The work began with the design and fabrication of a microstrip resonator that could be terminated to detect inductance changes within a microfluidic channel, replacing the resonator used for capacitance change detection. Another aspect of the work consisted

of developing and researching the theoretical equations used to model and simulate the anticipated inductance change caused by single superparamagnetic beads when flowing over a planar electrode loop. The theoretical framework needed to model the high frequency magnetic susceptibility of superparamagnetic beads consisting of ferrimagnetic single-domain particles was also researched.

The loop electrode design was modeled and simulated in Comsol Multiphysics, and the resonator design was simulated using Ansoft Designer. Several iterations of electrode designs were then fabricated and tested. Earlier versions were designed using Cadence and fabricated by Sensonit through CMC. The final versions were designed using L-edit and fabricated with the help of Jun Hui and Dwayne Chrusch at the Nanosystems Fabrication Laboratory at the University of Manitoba. Finally, prototype testing and experiments were performed to successfully detect single 4.5 μm superparamagnetic Dynabeads®.

1.4 Thesis Organization

This thesis is organized into the following chapters:

- Chapter 2 describes the composition and properties of the superparamagnetic beads detected in this thesis. The theory briefly describing the frequency response of the complex magnetic susceptibility is also presented.
- Chapter 3 gives an overview of the inductance sensor. The chapter describes the microwave interferometer on which the sensor is based: the

sensing electrode inside the microfluidic channel, sample injection and flow control, and the sensor apparatus.

- Chapter 4 derives the scalar magnetic potential equations and the time-averaged change in inductance caused by a magnetic sphere when subjected to a uniform sinusoidal steady-state magnetic field. The derived equations will provide a basis for the loop electrode designs in Chapter 5 used to maximize the sensor sensitivity.
- Chapter 5 covers the loop electrode designs and simulations and compares the inductance change values found using the theoretical equations derived in Chapter 3 to those found using 3D energy simulations. The inductance change profiles for the two loops used to detect single 4.5 μm Dynabeads® are shown.
- Chapter 6 focuses on the fabrication of the gold electrodes on a glass substrate, as well as the microfluidic channel fabrication.
- Chapter 7 describes the design and fabrication of the coupled transmission line resonator. A comparison between simulations and measurements is made. The rate of change of phase with inductance is provided for the two loops used to detect single 4.5 μm magnetic beads in this thesis.
- Chapter 8 provides the measurement results for the 2 loops. The sensor sensitivity and resolution is calculated and the real part of the magnetic permeability of a single 4.5 μm magnetic bead is derived from experimental measurements.

- Chapter 9 provides concluding remarks and potential future work and applications.

Chapter 2

Superparamagnetic Beads

2.1 Superparamagnetic Bead Composition and Complex Magnetic Susceptibility

The magnetic beads (4.5 μm Dynabeads®) detected in this work are composed of nanometre-sized particles of iron-oxide embedded inside a polymer matrix [Saf99]. The iron-oxide nanoparticles (NPs) are grown and magnetized inside monodisperse porous polymer beads, which are then coated in a polystyrene layer [Fon05]. The beads have a 20% iron volume fraction. Maghemite (γ-Fe_2O3) was found to be "the predominant crystalline phase" of iron-oxide inside superparamagnetic Dynabead® spheres, determined through Mössbauer spectroscopy, and the mean diameter of the NPs was found to be 8 nm [Fon05]. The NPs are small enough that they behave like single magnetic domains, and the thermal energy at room temperature randomly orients the magnetic moments of each NP along one of two directions of their easy axis, assuming uniaxial anisotropy [Fan06]. The random orientation of moments among the ensemble of NPs inside the bead causes the whole bead to have a net magnetic moment of zero in the absence of an applied field [Saf99]. When a magnetic field is applied, there is a net magnetization of the bead due to the response of the single-domain NPs to the applied field. The properties of the beads are therefore similar to paramagnetic materials, except that the beads show no remnant magnetization at room temperature (well below the Curie temperature) and often exhibit more than five orders of magnitude larger magnetization than paramagnetic materials.

The magnetic susceptibility, χ_m, of a magnetically linear, isotropic material, subjected to a dc magnetic field, $\bar{H}$, is a scalar quantity given by [Jon95]

$$\chi_m = \mu_r - 1 = M/H, \tag{2-1}$$

where M is the magnetization within the material, which is parallel to the applied field. Figure 2-1 [Fon05] shows the mass magnetization (magnetization, in A/m, divided by the 1600 kg/m^3 density of the M-450 bead) response of a superparamagnetic, M-450 Dynabead® at room temperature as a function of applied field (μ_0H). The inset shows the response to field magnitudes smaller than 15 mT. The response was analyzed with a 10 s timescale. The slope of the curve at a given point represents the scalar magnetic susceptibility

$$\chi_m = dM/dH. \tag{2-3}$$

The susceptibility value that is often cited for M-450 magnetic beads is $\chi_m = 0.24$ [Red96]. The initial magnetization provided by Fonnum et. al., corresponding to the initial slope at zero field of the curve in Fig. 2-1, is $\chi_m = 1.63$ [Fon05]. The slope in Fig. 2-1 falls to $\chi_m = 0.26$ at 100 mT, and down to $\chi_m = 0.03$ at 1 T. As is seen in Fig. 2-1, the response shows no hysteresis. Therefore, the magnetic beads exhibit a relatively large initial magnetization in the presence of an applied magnetic field while showing no remnant magnetization in the absence of the field. Although the individual NPs are made up of a ferrite material, the magnetic properties of the whole bead are superparamagnetic due to the small size of each NP domain [Kal03].

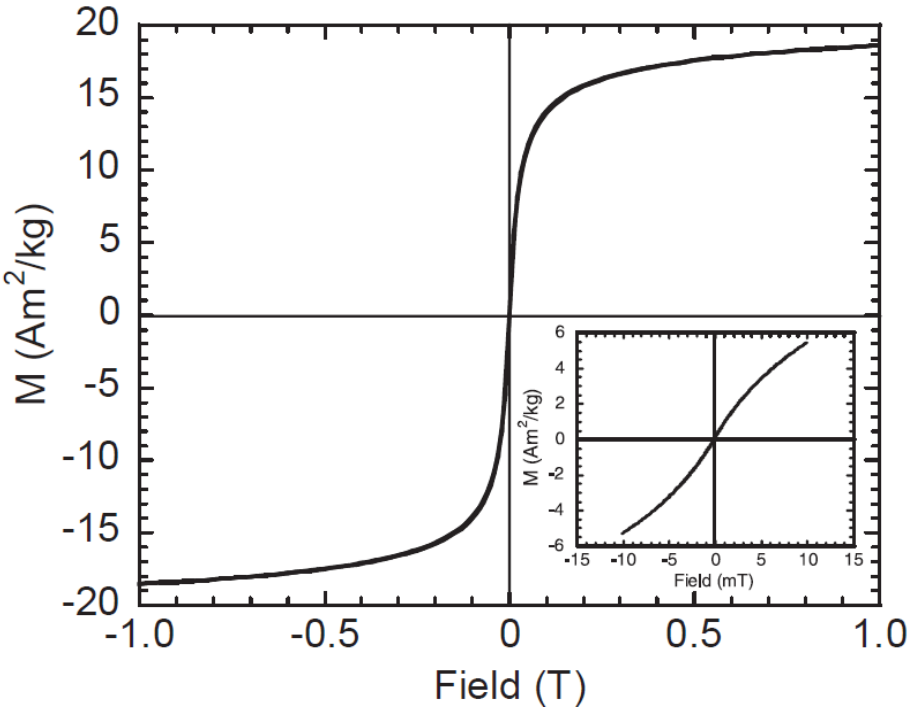

Figure 2-1: Mass magnetization (magnetization divided by 1600 kg/m^3 mass density) versus applied field, $\mu_0 H$, at room temperature for M-450 Dynabeads. Inset shows response to smaller magnitude fields. Measurement time was approximately 10 s [Fon05].

Each NP inside a superparamagnetic bead has a magnetic moment magnitude [Fan06]

$$m_{NP} = M_s v, \tag{2-3}$$

where M_s is the saturation magnetization, and v is the particle's magnetic volume. In equilibrium, the moment will be directed along the easy axis of the NP's internal anisotropy field, $\bar{H}_A$, which can be considered uniaxial in the case of single-domain maghemite NPs [Fan06]. The Néel relaxation time [Neel49],

$$\tau_N = \tau_0 \exp\left(\frac{Kv}{k_B T}\right), \tag{2-4}$$

determines the mean time between magnetic moment reversals. Kv is an energy barrier (K is the anisotropy energy density), which must be overcome for moment reversal to occur. For sufficiently small volumes, such as those represented by the NPs, this reversal will occur randomly at room temperature [Kal03]. Therefore, for measuring times much greater than τ_N, the average magnetic moment of each NP will be zero. As an applied field is increased, more NPs become aligned with the field, increasing the overall magnetization of the bead. The overall magnetization response is a function of the ensemble of NPs, complicated by the size and shape distribution of the NPs. Moreover, although the iron-oxide NPs are separated by a polymer matrix, they are influenced by inter-particle interactions [Fon05].

In this work, magnetic beads are detected in the GHz-frequency regime. The complex magnetic susceptibility of the ensemble of NPs embedded in the bead [Fan99]

$$\chi_m(\omega) = \chi_m'(\omega) - j\chi_m''(\omega) \tag{2-5}$$

will have a real part and an imaginary part. The complex magnetic susceptibility function $\chi_m(\omega)$ encapsulates the overall bead response, including the complicated dynamics of the internal NPs. Although the individual NPs have anisotropic internal fields, the bead as a whole will have a random distribution and orientation of these NPs, and can be approximated as an isotropic material. The field produced by the bead will be treated as though it were produced by a point dipole at the centre of the bead that has an identical single effective moment as the bead [Lan04]. In this model, the whole bead will be approximated as homogeneous.

As will be shown in Chapter 4, the component of the complex susceptibility that contributes to inductance changes in magnetic particles is the real part of the magnetic susceptibility, $\chi_m'(\omega)$. Due to a lack of microwave-frequency response measurements involving this type of magnetic bead, it is difficult to predict the value of χ_m' at the 1.5 GHz detection frequency used in this work. With the goal of understanding the frequency response in the GHz-frequency regime, the susceptibility of an ensemble of non-interacting NPs with a random orientation of anisotropy axes can be expressed in terms of longitudinal and transverse components [Fan99, Rai75], respectively,

$$\chi_m(\omega) = 1/3[\chi_{||}(\omega) + 2\chi_{\perp}(\omega)] \,, \tag{2-6}$$

where $\chi_{||}(\omega)$ is the susceptibility in a an ac field that is parallel to the easy axis, and $\chi_{\perp}(\omega)$ is the susceptibility in an ac field that is perpendicular to the easy axis [Rai75].

The longitudinal magnetic susceptibility component exhibits a relaxational response and depends on the ability of the single domains (moments) to align themselves with the applied field (Brownian relaxation) or to overcome an energy barrier within the NP and flip direction (Néel relaxation). The longitudinal response can be expressed using Debye's equation as [Fan99]

$$\chi_{||}(\omega) = \frac{\chi_{||}(0)}{1+j\omega\tau_{||}}, \tag{2-8}$$

where $\tau_{||}$ is the combination of the Brownian and Néel relaxation times of the distribution of NPs. Because the NPs inside the bead are encased in a polymer matrix, the time constant will be mostly due to the Néel relaxation. At higher frequencies, where the time constant is smaller than $\tau_{||}$, the magnetic domains cannot follow the applied field and the

real part of the longitudinal (relaxational) response tends to zero [Rai75]. The imaginary part of the overall magnetic susceptibility, $\chi_m{}''(\omega)$, has a maximum at $\omega_{max} = 1/\tau_{||}$ [Rai75]. This can be shown by first assuming that $\chi_\perp(\omega_{max}) = 0$ at this low frequency. The imaginary susceptibility, $\chi_m{}''(\omega)$, can now be expressed as

$$\chi_m{}''(\omega) = -\frac{\chi_{||}(0)\omega\tau_{||}}{1+\omega^2{\tau_{||}}^2}$$

$$= -\chi_{||}(0)(\omega^{-1}{\tau_{||}}^{-1} + \omega\tau_{||})^{-1}. \quad (2\text{-}9)$$

The maximum for $\chi_m{}''(\omega)$ occurs when

$$\omega_{max} = 1/\tau_{||}. \quad (2\text{-}10)$$

The direction of each NP's internal field is called the easy axis. Under equilibrium conditions, the magnetic moment and the internal anisotropy field of an individual NP are parallel [Fan99]. The transverse susceptibility response, $\chi_\perp(\omega)$, has a resonant character, and is caused by a deviation of the NP's magnetic moment from the easy axis of its internal field, inducing a precession of the moment about the easy axis [Fan06]. The easy axis is directed along the NP's internal field $H_A = 2K/M_s$, where K is the uniaxial magnetic anisotropy, and M_s is the saturation magnetization of the NP. For low temperatures or high internal fields, and therefore small angles of precession, the intrinsic angular resonance frequency, ω_{res}, can be expressed as [Fan99, Fan06]

$$\omega_{res} = \gamma H_A\ , \quad (2\text{-}11)$$

where γ is the gyromagnetic ratio. Due to a distribution of NP sizes in the magnetic bead, there will also be a distribution of resonant frequencies [Fan99]. The resonant frequency

represents the natural precession frequency of an NP. Precession can be induced by a transverse sinusoidal field [Rai75]. Since the real part of the longitudinal susceptibility tends to zero at higher frequencies, the transverse susceptibility will contribute the most to the real part of the effective magnetic susceptibility of the bead at GHz frequencies. The analytical expression for the transverse susceptibility [Fan95], which includes stochastic components, accounts for size and shape distributions, and is coupled with the relaxational response, has been characterized by Raikher and Schlomis [Rai75] but is not included here. It should be noted at this point that eddy currents are not expected to form and oppose the applied magnetic field inside the beads because the electrical conductivity of maghemite (γ-Fe_2O_3) is on the order of $1x10^{-10}$ S/cm [Vij03].

Fannin et al. performed GHz-frequency measurements, shown in Fig. 2-2 [Fan06], of the complex susceptibility of ferrofluids containing maghemite (γ-Fe_2O3) particles with a mean diameter of 10 nm inside octane. The top solid line represents the real part of the magnetic susceptibility where there is no external static polarizing field. The other solid lines represent measurements with varying strengths of polarizing field. At GHz frequencies, the real part of the normalized magnetic susceptibility decreases to a fraction of the value at low frequencies, and turns negative at the resonant frequency. It should be noted that a ferrofluid of maghemite nanoparticles will exhibit much larger susceptibility at low frequencies than at higher frequencies because the maghemite NPs are free to align themselves with the applied field by rotating inside the fluid. For M-450 beads, the maghemite NPs are embedded inside a polymer matrix, and cannot cooperatively rotate to align with the applied field. Furthermore, because the mean radius of the NPs in Fig. 2-2 is 10 nm whereas the NPs in M-450 beads have a mean radius of

4nm, the longitudinal susceptibility will contribute more to the real part of the susceptibility at 1.5 GHz for M-450 magnetic beads. Therefore the shape of the response of the real part of the susceptibility, $\chi_m'(\omega)$, will not necessarily closely follow the plot for the top solid line in Fig. 2-2. Assuming a 1.63 value for $\chi_m'(0)$ for M-450 beads, and the same response as in Fig. 2-2, the estimated real part of the susceptibility at 1.5 GHz is $\chi_m'(1.5\ GHz) \cong 0.3$. It must be stressed, however, that the susceptibility function for M-450 beads is unknown and the value of $\chi_m'(\omega)$ for each bead at 1.5 GHz can only be determined experimentally.

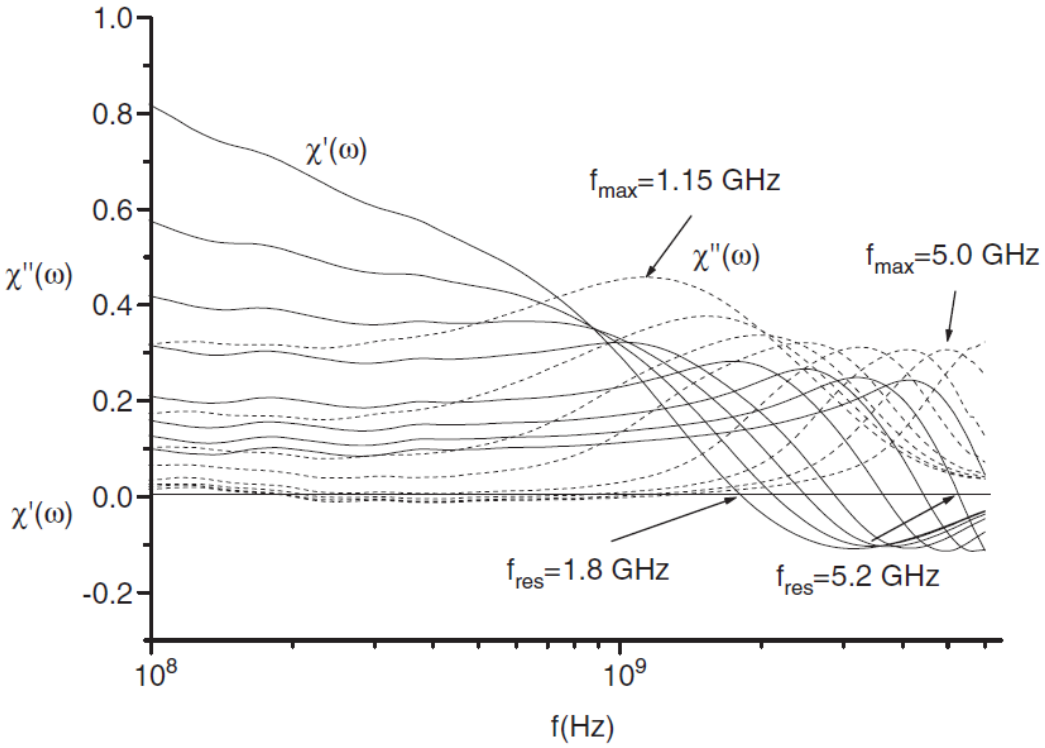

Figure 2-2: Normalized complex susceptibility as a function of frequency for different values of external polarizing magnetic field, H. The sample consists of a suspension of maghemite particles, of mean radius 10 nm, in octane. The top, solid line represents the real part of the susceptibility without an external polarizing field [Fan06].

Chapter 3
Sensor Operation and Apparatus

This chapter gives an overview of the inductance change sensor and apparatus. The basic operation of the sensor is depicted in Fig. 3-1. The sensor detects resonance changes caused by the presence of flowing magnetic beads inside a microfluidic channel. A planar gold loop electrode sits at the bottom of a microfluidic channel. The loop electrode terminates a transmission line, which acts like a half-wave ($\lambda/2$) resonator. A 1.5 GHz sinusoidal signal is coupled to the transmission line, inducing a current in the loop, and the resulting magnetic field magnetizes a passing bead. The magnetized bead causes a net change in stored magnetic energy in the volume around the loop, resulting in a net change in inductance of the loop electrode. The change in load inductance due to a passing bead causes a change in resonant frequency of the coupled-line $\lambda/2$ resonator, resulting in a change in the transmission phase, $\Delta\Phi(\Delta L)$, of the resonator, as shown in the idealized resonator response in Fig. 3-2. Because the slope of the magnitude response is approximately zero at the resonant frequency, a change in load inductance will have a very small effect on the amplitude of the output signal. A microwave interferometer is used to monitor the change in phase of the resonator caused by a single passing magnetic bead.

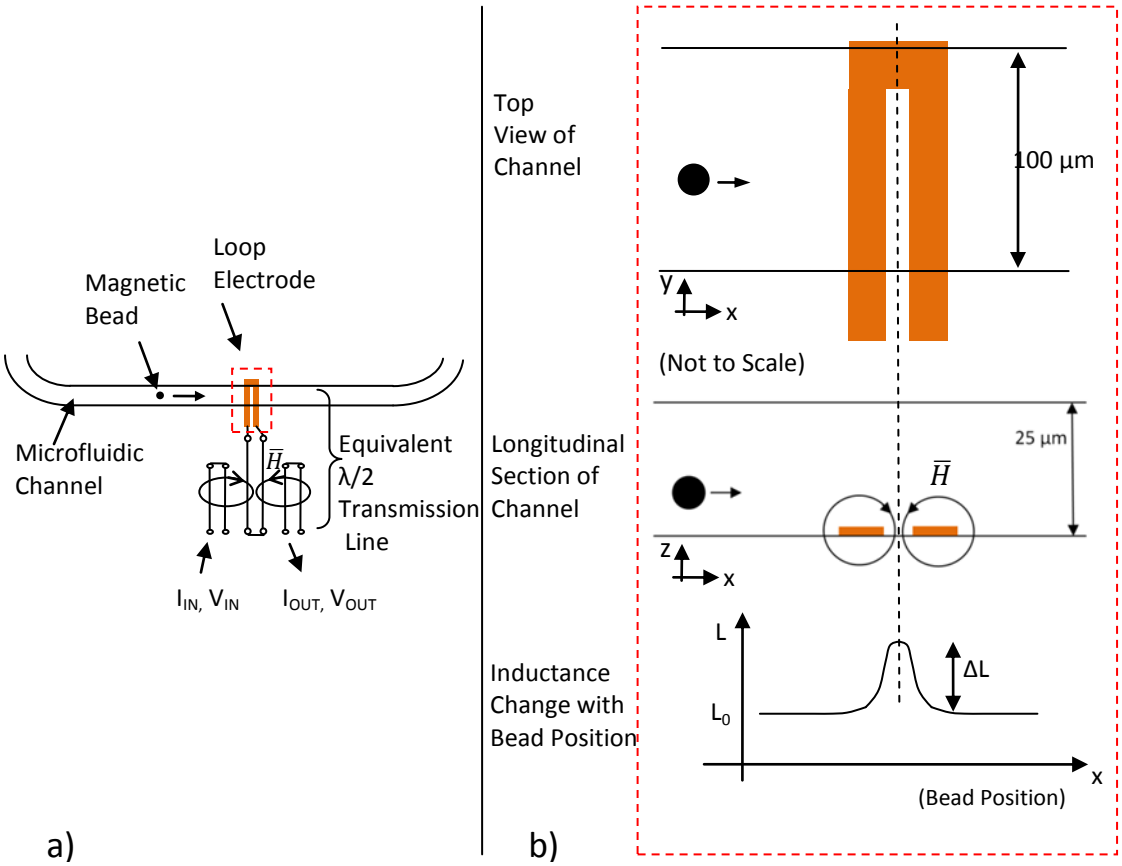

Figure 3-1: Sensor Operation. a) A coupled line resonator, whose centre line consists of a section of transmission line that is a half wavelength at the resonant frequency, is used to detect changes in load inductance of a planar gold loop electrode at the bottom of a microfluidic channel. As a single magnetic bead flows over the loop electrode, it becomes magnetized by the ac magnetic field, which is generated in the loop by a 1.5 GHz induced centre transmission line current. As the bead becomes magnetized, there is a resulting net change in stored magnetic energy, and therefore inductance, in the volume around the loop. b) Top and longitudinal section views of a 4.5 µm superparamagnetic bead flowing through a microfluidic channel above a planar gold loop electrode, and the resulting inductance change profile with horizontal bead position. The maximum change in inductance for a particular bead elevation occurs at the centre of the loop electrode.

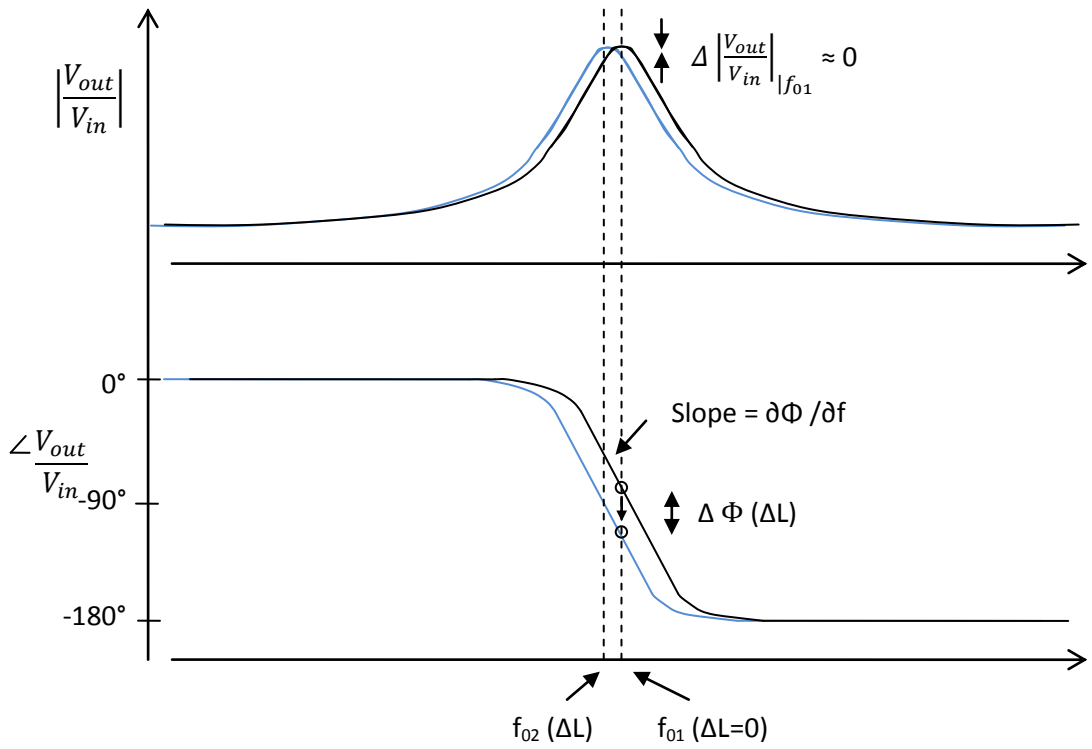

Figure 3-2: Resonator transmission magnitude and phase response curves showing a resonant frequency shift due to a change in load inductance inside the channel for ΔL=0 (black curves), and for ΔL (blue curves). At the original resonant frequency, f_{01}, the magnitude change due to a resonant frequency shift is negligible, whereas the change in phase, ΔΦ, is proportional to the slope of the phase response, ∂Φ/∂f, near the resonant frequency.

3.1 Overview of Detection System

The inductance change detection system is based on a microwave interferometric system [Fer09] used for capacitive flow cytometry. The schematic of the microwave interferometer, resonator, and microfluidic device is presented in Fig. 3-3. A 1.5 GHz signal is divided between a reference path and a resonator path and subsequently

combined using a mixer. The interferometer operates as a phase detector at the resonant frequency of a half-wave, coupled transmission-line resonator (the resonator is described

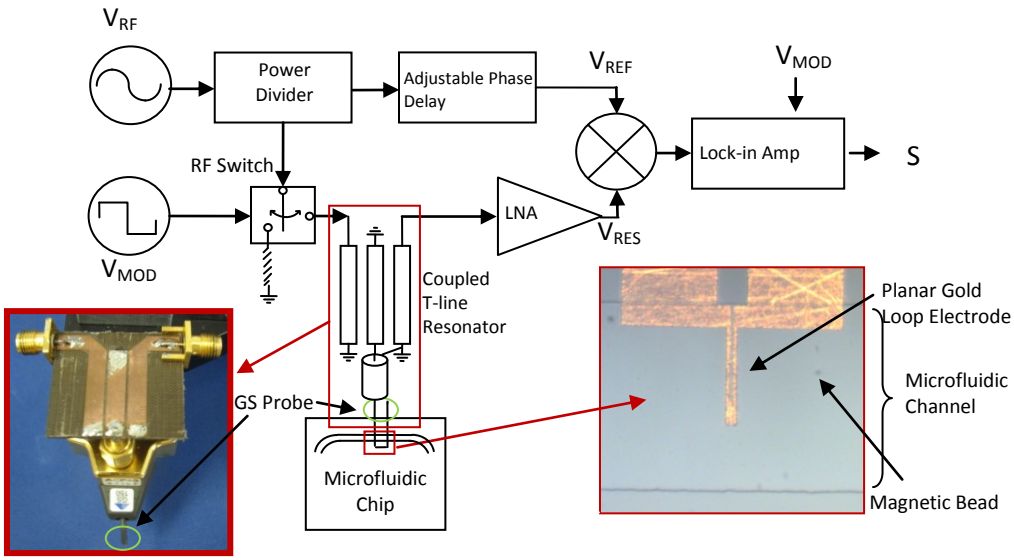

Figure 3-3: Microwave interferometer, resonant sensor, and microfluidic device. A 1.5 GHz signal is split between a reference path and a resonator path. Paths are 90° out of phase so that the mixer output is null in the absence of a magnetic bead. A Ground-Signal probe is used to terminate the resonator with a particular gold loop electrode, which is situated at the bottom of a microfluidic channel. As a magnetic bead flows above a planar loop electrode, the load inductance changes, changing the transmission phase of the resonator. The mixer output is proportional to the change in transmission phase. The reference path is modulated at the same frequency as the lock-in-amplifier to filter out noise outside of a narrow bandwidth.

in detail in Chapter 7). As a magnetic bead passes over the loop electrode, the change in load inductance, L+ΔL, induces a shift in the resonant frequency of the resonator, changing the transmission phase of the resonator, and results in a change in phase, ΔΦ, in the resonator path. The voltage at the resonator path input to the mixer can be expressed as

$$V_{RES} = |V_{RES}|_{\mathrm{pk}} \cos\left(\omega_{RF} t + \Phi_{RES} + \Delta\Phi\right), \tag{3-1}$$

where Φ_{RES} is the phase delay in the resonator path and $\Delta\Phi$ is the change is transmission phase of the resonator due to an inductance change caused by a passing magnetic bead. The voltage at the reference path input to the mixer is phase delayed by a manually adjustable phase delay until it is 90° out of phase with the resonator path, and can be expressed as

$$V_{REF} = -|V_{REF}|_{\text{pk}} \sin(\omega_{RF} t + \Phi_{RES}). \tag{3-2}$$

After filtering out the $2\omega_{RF}$ component, the mixer output becomes

$$\begin{aligned} V_{REF} V_{RES} &= -|V_{REF}||V_{RES}| \sin(\omega_{RF} t + \varphi_{RES} - \omega_{RF} t - \varphi_{RES} - \Delta\Phi) \\ &= |V_{REF}||V_{RES}| \sin(\Delta\Phi), \end{aligned} \tag{3-3}$$

where $|V_{REF}|$ and $|V_{RES}|$are the rms magnitude values. The output of the mixer is fed into a lock-in amplifier. The resonator path and the lock-in amplifier are modulated by a 91.5 kHz square wave. The time-averaged lock-in amplifier output, S, can be expressed as

$$S = G|V_{REF}||V_{RES}| \sin(\Delta\Phi), \tag{3-4}$$

which for small $\Delta\Phi$ becomes

$$S \cong G|V_{REF}||V_{RES}|\Delta\Phi, \tag{3-5}$$

where G is overall gain of the mixer and lock-in amplifier. The change in resonator transmission phase due to an inductance change can be expressed as

$$\Delta\Phi \cong \left(\frac{\partial\varphi}{\partial L}\right)|_{f_o}(\Delta L), \tag{3-6}$$

$$\Delta\Phi \cong \left(\frac{\partial\varphi}{\partial f}\right)|_{f_o}\left(\frac{\partial f}{\partial L}\right)|_{f_o}(\Delta L), \tag{3-7}$$

where $(\partial f/\partial L)|_{f_o}$ is the rate of change in frequency with inductance, and $(\partial \emptyset/\partial f)|_{f_o}$ is the rate of change in phase with frequency. The output signal can therefore be expressed as

$$S \cong G|V_{REF}||V_{RES}|\left(\frac{\partial \varphi}{\partial f}\right)|_{f_o}\left(\frac{\partial f}{\partial L}\right)|_{f_o}(\Delta L). \tag{3-8}$$

The signal due to a magnetic bead is very small and would be totally obscured by the noise of the system. To detect this signal, the resonator path is modulated by a 91.5 kHz square wave. The mixer output is fed into a lock-in-amplifier (LIA) that locks to the 91.5 kHz signal and rejects noise outside a preselected bandwidth as determined by the time-constant, τ, of the LIA. The output of the LIA is proportional to the mean output of the mixer. Reducing the bandwidth reduces the noise at the output but it also affects the ability to detect fast-flowing beads (the LIA time constant is inversely proportional to the bandwidth and the faster that a bead flows, the smaller the time constant that is required). In this work, a time constant of $\tau = 3$ ms is chosen, so the bandwidth is 42 Hz.

The interferometer RF electronics are located inside an EMI chamber along with a microscope and camera to simultaneously record the video of the bead crossing events. The LIA is located outside the EMI chamber along with the signal generator and computer interface. The entire setup is shown in Fig. 3-4. A close-up of the XYZ positioner, microwave resonator, probe and microfluidic device is shown in Fig. 3-5. The probe can be positioned onto the desired electrode loop on the microfluidic device. The microfluidic channel and loop electrodes are lit from the top through the microscope lens and are backlit using an LED light reflected off of a metal reflector.

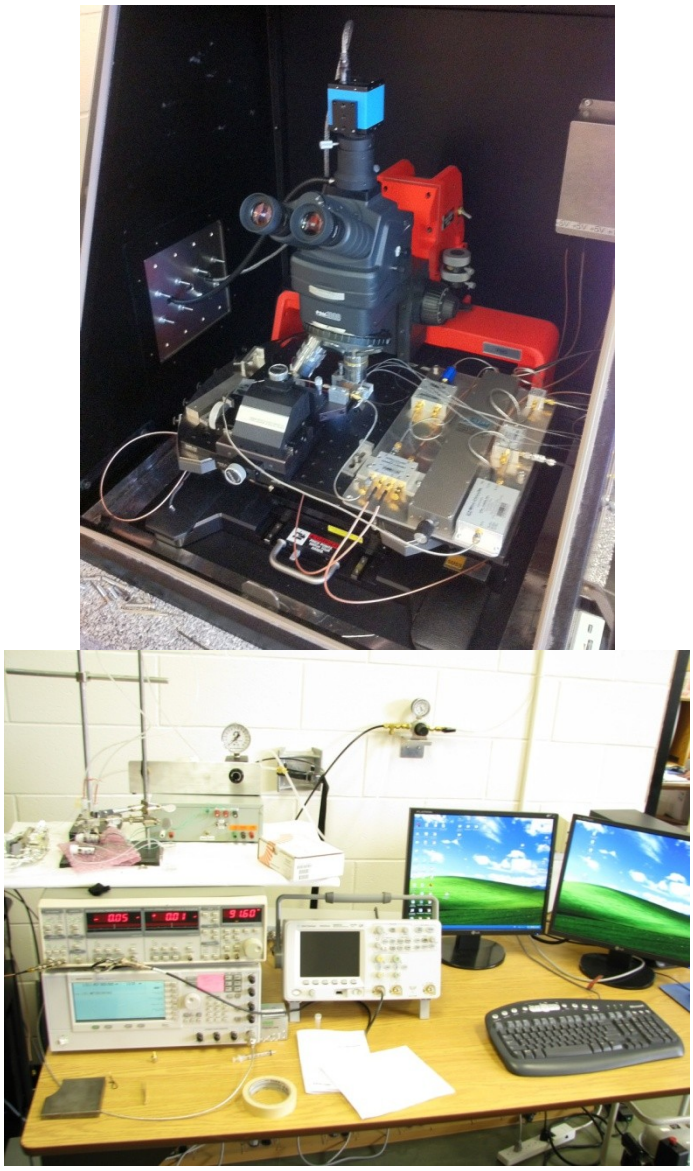

Figure 3-4: Microwave interferometer, resonant sensor, microfluidic device, and microscope located inside an EMI enclosure (top). Signal source, LIA, syringe apparatus, and computer interface (bottom).

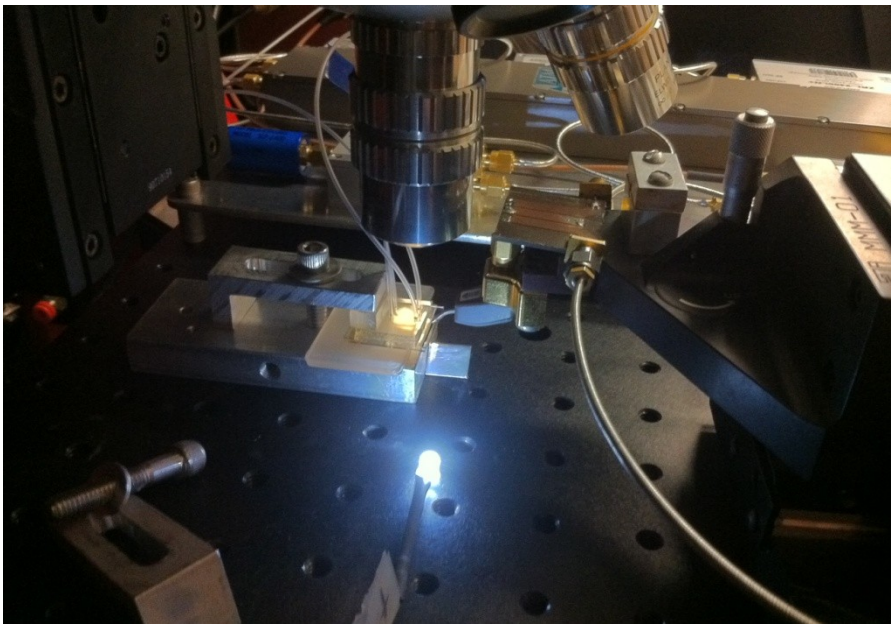

Figure 3-5: Close-up of the microwave resonator and probe attached to an XYZ positioner. The microwave probe is used to touch down onto the desired electrode loop on the microfluidic chip. An LED light is reflected off of a metal surface to provide backlighting through the bottom of the channel, in addition to the light through the microscope lens.

3.2 Fluid Suspension Injection and Control

The suspension of magnetic beads diluted in deionized water is introduced into the microfluidic chip ports P_1 and P_4 (Fig. 3-6) using syringes connected to polyethylene tubing (see Fig. 3-7). One syringe contains the diluted sample, and the other contains deionized water. The relative elevation of the syringes provides a gravity-induced pressure differential across the small channel in which the loop electrode is located. Referring to Fig. 3-6, ports P_1 and P_4 are the input ports connected to the syringes through tubing. The pressure in the syringes can be set through a pressure tank and valve connected through separate tubing. The output ports P_2 and P_3 are connected to tubing that leads to a disposal beaker. Two 15 psi solenoid clamps are connected to the output

tubing of P2 and P_3. The clamps are used to divert the flow entirely through the cross channel by acting as a valve at the output of either port. The pressure tank and the valves enable quick introduction of a new sample into the cross-channel or as a way of purging the channel of any remaining sample by flushing water through it. The fluid control set-up is shown in Fig. 3-7.

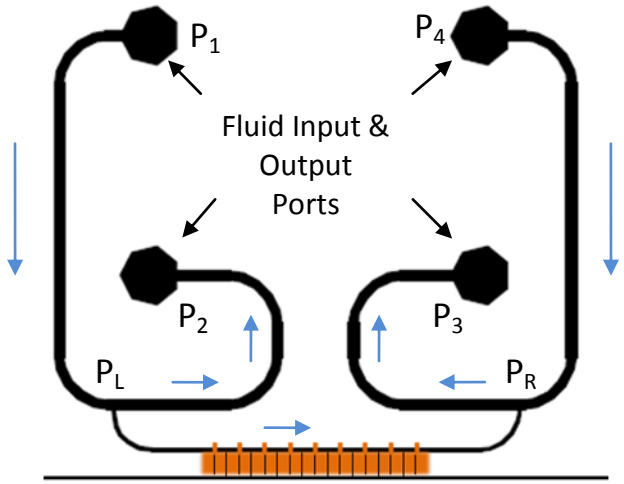

Figure 3-6: Microfluidic Device. H-channel design used to control the fluid-flow direction and rate in the small cross channel (P_L to P_R), based on the altitude differential of two syringes. The suspension of magnetic beads is introduced into port P_1, and deionized water is introduced into P_4. Ports P_2 and P_3 are output ports that have their tubing placed in a beaker. Blue arrows represent fluid-flow direction, assuming that the pressure at P_1 is greater than at P_4.

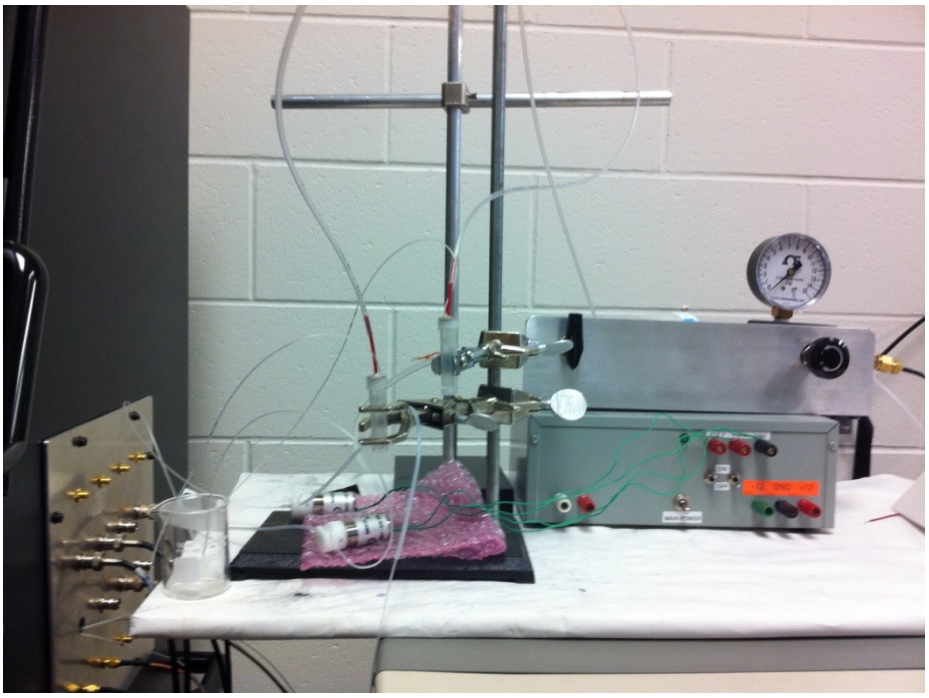

Figure 3-7: Fluidic control set-up. Fluid-flow direction and rate is controlled by the differential altitude of two syringes. Solenoid clamps acting as valves at the output ports can be used to purge the channel of any remaining beads or to quickly fill the cross-channel with the new sample suspension.

Figure 3-8 shows the equivalent H-channel schematic for the microfluidic device configuration shown in Fig. 3-6 [Nik10]. In this schematic, it is assumed that points P_1 through P_4 represent the points at the syringes and the beaker and not at the microfluidic device input and output ports. Here p refers to pressure. The volumetric fluid flow between two points can be expressed as

$$F_{ij} = (p_i - p_j)/R, \tag{3-9}$$

where R is the resistance to flow and p is the pressure at a particular point. Assuming an incompressible fluid, the flow at a junction will sum to zero. At the cross channel points L and R, respectively, we have [Nik10]

$$(p_1 - p_2)/R_A + (p_2 - p_L)/R_B + (p_R - p_L)/R_C = 0, \quad (3\text{-}9)$$

$$(p_4 - p_R)/R_A + (p_3 - p_R)/R_B + (p_L - p_R)/R_C = 0. \quad (3\text{-}10)$$

Using Eq. 3-9 and Eq. 3-10, the pressure differential across the cross channel can be expressed as

$$p_L - p_R = \left[\frac{(p_1 - p_4)}{R_A} + \frac{(p_2 - p_3)}{R_B}\right]\left[\frac{R_A R_B R_C}{(R_A + R_B)R_C + 2R_A R_B}\right]. \quad (3\text{-}11)$$

Since the output ports are placed in an open beaker, $p_2 = p_3 = 0$. Therefore the cross channel differential pressure becomes

$$p_L - p_R = (p_1 - p_4)\left[\frac{R_B R_C}{(R_A + R_B)R_C + 2R_A R_B}\right]. \quad (3\text{-}12)$$

From Eq. 3-12, it can be seen that the cross-channel pressure is proportional to the differential pressure between P_1 and P_4 (between the two syringes). From the fact that it takes 1 bar of pressure to lift a column of water approximately 10 m, a 1 cm difference in elevation between the two syringes would produce approximately 1 mbar or 100 Pa of pressure.

In some of the experiments presented in this thesis, the electrodes were aligned inside a larger channel and only two ports were used as fluid input and output ports; the other two microfluidic ports were sealed. One syringe was used to inject the suspension of magnetic beads, and the output tube was placed in a beaker. Since two clamps were used to hold down the tubing at the input and output ports instead of 4, this setup reduced problems with fluid leakage.

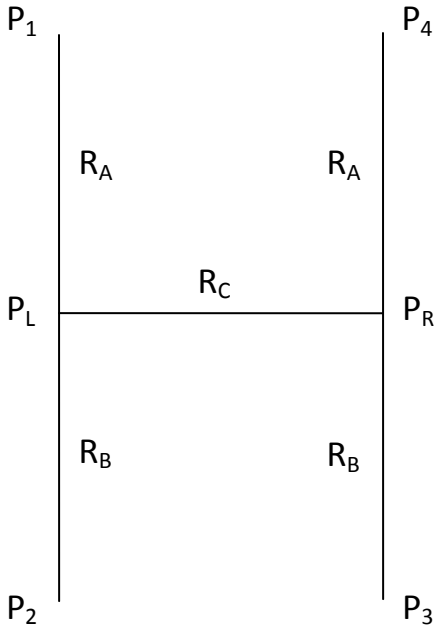

Figure 3-8: H-channel fluid flow schematic. R represents the resistance to flow between two points and P represents the pressure at a particular point. P_1 and P_4 represent the pressure at the two syringe fluid input points, whereas P_2 and P_3 represent the pressure at the output points inside the beaker.

CHAPTER 4

INDUCED INDUCTANCE CHANGE

This chapter will provide the theoretical background and derivation of the time-averaged inductance change caused by the presence of a homogeneous magnetic sphere, when subjected to a uniform sinusoidal steady-state magnetic field. The scalar magnetic potentials inside and outside of the sphere will first be derived. The time-averaged change in magnetic energy, and the resulting change in inductance of the sensing loop, will then be derived using these scalar magnetic potentials. This time-averaged change in inductance will be proportional to the signal caused by an individual magnetic bead as it passes over the sensing electrode.

4.1 Solution of Laplace's Equation for the Scalar Magnetic Potential Inside and Outside of a Homogeneous Magnetic Sphere Subjected to a Uniform Sinusoidal Steady-state Magnetic Field

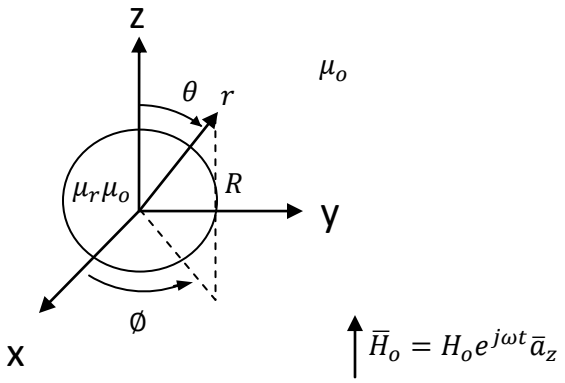

Figure 4-1: A homogeneous magnetic sphere, centred at the origin, is subjected to a uniform sinusoidal steady-state magnetic field. The wavelength of the applied field is assumed to be much greater than the total volume radius.

In this analysis, we consider a magnetic sphere of radius, R, and with a homogeneous permeability, $\mu_r\mu_o$, suspended in a fluid with permeability, μ_o. The sphere is assumed to be magnetically linear. The wavelength, λ, of the sinusoidal steady-state field, $\overline{H}_o$, is assumed to be much greater than the entire volume radius, preserving the uniformity of the applied field. Current sources are not present in the solution volume, therefore $\nabla \times \overline{H} = 0$, and we can employ the magnetic scalar potential, Ψ, where $\overline{H} = -\nabla\Psi$ (since $\nabla \times (\nabla U) \equiv 0$). Using the effective magnetic moment method used by Jones [Jon95], we will define an effective moment, $\overline{m}_{eff}$, as being equivalent to a single

magnetic dipole moment that, when placed at the centre of the sphere, produces the same magnetostatic potential. The sphere is taken to have zero net volume magnetization, $\overline{M}$, in the absence of an external field.

The potential inside and outside of the homogeneous magnetic sphere is solved using Laplace's equation in spherical coordinates;

$$\nabla^2\Psi = \frac{1}{r^2}\frac{\partial}{\partial r}\left(r^2\frac{\partial\Psi}{\partial r}\right) + \frac{1}{r^2 sin\theta}\frac{\partial}{\partial\theta}\left(sin\theta\frac{\partial\Psi}{\partial\theta}\right) + \frac{1}{r^2 sin^2\theta}\frac{\partial}{\partial\theta}\left(\frac{\partial^2\Psi}{\partial\emptyset^2}\right) = 0 \qquad (4\text{–}1)$$

For the dipole approximation, when $R \ll \lambda$, we assume azimuthal symmetry and the potential becomes

$$\nabla^2\Psi = \frac{1}{r^2}\frac{\partial}{\partial r}\left(r^2\frac{\partial\Psi}{\partial r}\right) + \frac{1}{r^2 sin\theta}\frac{\partial}{\partial\theta}\left(sin\theta\frac{\partial\Psi}{\partial\theta}\right) = 0 \qquad (4\text{–}2)$$

Assuming $\Psi(r,\theta) = \Psi'(r)\Psi''(\theta)$, using separation of variables,

$$\nabla^2\Psi(r,\theta) = \frac{1}{r^2}2r\frac{d\Psi'(r)}{dr}\Psi''(\theta) + \frac{d^2\Psi'(r)}{dr^2}\Psi''(\theta) + \frac{1}{r^2 sin\theta}\left(cos\theta\frac{d\Psi''(\theta)}{d\theta}\Psi'(r) + \frac{d^2\Psi''(\theta)}{d\theta^2}\Psi'(r)sin\theta\right) = 0$$

$$\frac{2r}{\Psi'(r)}\frac{d\Psi'(r)}{dr} + \frac{r^2}{\Psi'(r)}\frac{d^2\Psi'(r)}{dr^2} + \frac{1}{\Psi''(\theta)sin\theta}\left(cos\theta\frac{d\Psi''(\theta)}{d\theta} + \frac{d^2\Psi''(\theta)}{d\theta^2}sin\theta\right) = 0.$$

Solving for the radial component,

$$\frac{r^2}{\Psi'(r)}\frac{d^2\Psi'(r)}{dr^2}+\frac{2r}{\Psi'(r)}\frac{d\Psi'(r)}{dr}=k^2=l(l+1) \tag{4-3}$$

where $k^2=l(l+1)$ and l is a natural number. Assuming a solution of the form $\Psi(r)=Cr^m$, and employing this in Eq. (4-3), we can solve the auxiliary equation for m.

$$2rmr^{m-1}+r^2m(m-1)r^{m-2}=r^ml(l+1)$$

$$m(m-1)+2m=l(l+1)$$

$$m(m+1)=l(l+1)$$

leading to the solution $m=l$, or $-l-1$, and finally

$$\Psi'(r)=C_1r^l+C_2r^{-l-1} \quad ; \quad C_1,C_2\in\mathbb{R}. \tag{4-4}$$

Solving for the $\Psi''(\theta)$ component of the scalar potential,

$$\frac{1}{\Psi''(\theta)sin\theta}\left(cos\theta\frac{d\Psi''(\theta)}{d\theta}+\frac{d^2\Psi''(\theta)}{d\theta^2}sin\theta\right)=-k^2=-l(l+1)$$

$$\frac{d^2\Psi''(\theta)}{d\theta^2}+\frac{cos\theta}{sin\theta}\frac{d\Psi''(\theta)}{d\theta}+l(l+1)\Psi''(\theta)=0 \tag{4-5}$$

Equation (4-5) is in the form of Legendre's differential equation whose solutions are Legendre polynomials, $P_l(cos\theta)$. Taking the product of $\Psi'(r)\ and\ \Psi''(\theta)$ yields

$$\Psi(r,\theta)=(C_1r^l+C_2r^{-l-1})\,P_l(cos\theta).$$

Treating the magnetic sphere as a homogeneous sphere with a single effective magnetic dipole moment at its centre, $\bar{m}_{eff} = m_{eff}\bar{a}_z$, the scalar magnetic potential, $\Psi(r,\theta)$, will be represented by the $l = 1$ term only, and thus by the first Legendre polynomial $P_1(cos\theta) = cos\theta$. Therefore, the scalar magnetic potential can be expressed as

$$\Psi(r,\theta) = (C_1 r cos\theta + C_2 r^{-2} cos\theta)\ . \tag{4-6}$$

To determine the constants C_1 and C_2, Eq. (4-6) has to be considered separately inside and outside of the sphere ($r < R$ and $r > R$). For the $r > R$ case, the first constant, ${C_1}^{(o)} = -H_o e^{j\omega t}$, since for $r \gg R$, the r^{-2} term vanishes and $\bar{H}(r \gg R, \theta = 0) = -\nabla\Psi(r,0) \cong H_o e^{j\omega t}\bar{a}_z$. For the $r < R$ case, the second constant ${C_1}^{(i)} = 0$; otherwise the potential would approach infinity at the centre of the sphere. Therefore the scalar magnetic potentials inside and outside of the sphere can then be expressed as [Jon95]

$$\Psi_1(r,\theta) = -{C_1}^{(i)} r cos\theta \quad , \quad r < R \tag{4-7a}$$

$$\Psi_2(r,\theta) = (-H_o e^{j\omega t} r cos\theta + -{C_2}^{(o)} r^{-2} cos\theta) \quad , \quad r > R. \tag{4-7b}$$

The remaining constants ${C_1}^{(i)}$ and ${C_2}^{(o)}$ can be solved by equating

$$\Psi_1(R,\theta) = \Psi_2(R,\theta)$$

and

$$B_{r1}(R,\theta) = B_{r2}(R,\theta)$$

at the particle-fluid boundary, $r = R$, where $B_{r1}(R,\theta)$ and $B_{r2}(R,\theta)$ are the normal magnetic flux density components inside and outside of the sphere, respectively.

$$\Psi_1(R,\theta) = -\,C_1{}^{(i)} R\cos\theta = -H_o e^{j\omega t} R\cos\theta + C_2{}^{(o)} \cos\theta R^{-2} = \Psi_2(R,\theta) \tag{4-8}$$

$$B_{r1}(R,\theta) = \mu_o \mu_r (-\partial\Psi_1(R,\theta)/\partial r) = \mu_o \mu_r\, C_1{}^{(i)} \cos\theta, \tag{4-9}$$

$$B_{r2}(R,\theta) = \mu_o (-\partial\Psi_2(R,\theta)/\partial r) = \mu_o H_o e^{j\omega t}\cos\theta + 2\mu_o\, C_2{}^{(o)} \cos\theta R^{-3}. \tag{4-10}$$

Using equations (4-9) and (4-10),

$$C_2{}^{(o)} = \frac{1}{2}\mu_r C_1 R^3 - \frac{1}{2} H_o e^{j\omega t} R^3. \tag{4-11}$$

Using equation (4-11) with equation (4-8),

$$-\,C_1{}^{(i)} R\cos\theta = -H_o e^{j\omega t} R\cos\theta + (\tfrac{1}{2}\mu_r\, C_1{}^{(i)} R^3 - \tfrac{1}{2} H_o e^{j\omega t} R^3)\cos\theta R^{-2} \quad ,$$

$$C_1{}^{(i)} = -H_o e^{j\omega t} + (\tfrac{1}{2}\mu_r\, C_1{}^{(i)} - \tfrac{1}{2} H_o e^{j\omega t}) \,,$$

$$C_1{}^{(i)} = 3H_o e^{j\omega t}/(\mu_r + 2). \tag{4-12}$$

$$C_2{}^{(o)} = \frac{1}{2}\frac{[3\mu_r - (\mu_r + 2)]}{(\mu_r + 2)} H_o e^{j\omega t} R^3,$$

$$C_2{}^{(o)} = \frac{(\mu_r - 1)}{(\mu_r + 2)} H_o e^{j\omega t} R^3 \tag{4-13}$$

Finally, the scalar magnetic potentials inside and outside of the sphere become

$$\Psi_1(r,\theta) = -3[H_o e^{j\omega t}/(\mu_r + 2)] r\cos\theta \quad , \quad r < R \tag{4-14}$$

$$\Psi_2(r,\theta) = (-H_o e^{j\omega t} r\cos\theta + H_o e^{j\omega t} R^3 \tfrac{(\mu_r - 1)}{(\mu_r + 2)} r^{-2}\cos\theta) \quad , \quad r > R. \tag{4-15}$$

4.2 Inductance Change Caused by a Single Superparamagnetic Sphere

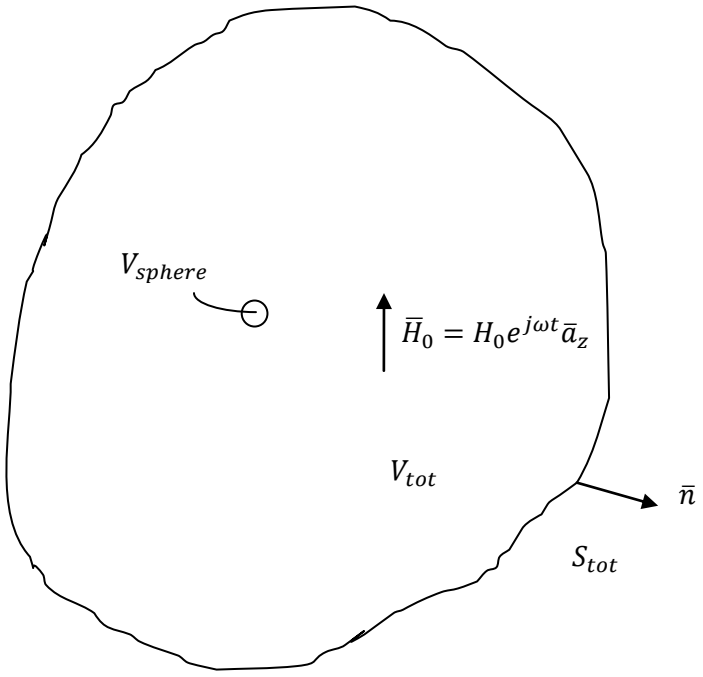

Figure 4-2: The magnetic sphere occupies a volume V_{sphere} inside the solution volume, V_{tot}, and is assumed to be subjected to a uniform, sinusoidal steady-state magnetic field intensity $\bar{H}_0$.

The superparamagnetic sphere perturbs a volume of free-space, V_{tot}, that is subjected to a uniform sinusoidal steady-state magnetic field, $\bar{H}_0 = H_0 e^{j\omega t}\bar{a}_z$, as shown in Fig. 4-2. Using Eq. 4-14 and Eq. 4-15, the magnetic field intensities inside and outside of a homogeneous magnetic sphere of effective complex permeability $\mu_r\mu_o$ and radius R become

$$\bar{H}_1 = -\nabla\Psi_1 = \frac{3H_o e^{j\omega t}}{\mu_r+2}(cos\theta\bar{a}_r - sin\theta\bar{a}_\theta) = \frac{3H_o e^{j\omega t}}{\mu_r+2}\bar{a}_z \quad , \quad r < R \qquad (4\text{-}16a)$$

$$\bar{H}_2 = -\nabla\Psi_2 \; =$$

$$H_o e^{j\omega t}\left(cos\theta + 2R^3\frac{(\mu_r-1)}{(\mu_r+2)}r^{-3}cos\theta\right)\bar{a}_r + H_o e^{j\omega t}\left(-sin\theta + R^3\frac{(\mu_r-1)}{(\mu_r+2)}r^{-3}sin\theta\right)\bar{a}_\theta \;, \qquad r > R$$

$$= H_o e^{j\omega t}cos\theta\bar{a}_r - H_o e^{j\omega t}sin\theta\bar{a}_\theta = H_o e^{j\omega t}\bar{a}_z \quad , \qquad r \to \infty. \tag{4-16b}$$

The first terms in each component of $\bar{H}_2$ add up to the applied (unperturbed) magnetic field $\bar{H}_o = H_o e^{j\omega t}\bar{a}_z$. The second terms are the added perturbed field components due to the magnetic sphere for $r > R$. The second terms decrease quickly with r due to their r^{-3} dependence.

The time-averaged stored magnetic energy within a free-space volume, V_{tot}, due to a steady-state sinusoidal field $\bar{H}_o$, when the magnetic sphere is not present, can be expressed as [Poz98a]

$$W_{mo} = \left(\frac{1}{4}\right) Re\left\{\int_{V_{tot}} \bar{H}_o \cdot \bar{B}_o^* \, dV\right\}. \tag{4-17}$$

Note that the field quantities are amplitudes and not rms quantities. The change in the time-averaged stored magnetic energy due to the presence of the magnetic sphere is

$$\Delta W_m = W_m - W_{mo}, \tag{4-18}$$

where W_m is the new time-averaged stored magnetic energy within the entire volume, V_{tot}, when the magnetic sphere is present, and is expressed as

$$W_m = \left(\frac{1}{4}\right) Re\left\{\int_{V_{tot}} \bar{H} \cdot \bar{B}^* \, dV\right\}. \tag{4-19}$$

The time-averaged change in magnetic energy is thus expressed as

$$\Delta W_m = \left(\frac{1}{4}\right) Re\left\{\int_{V_{tot}} (\bar{H} \cdot \bar{B}^* - \bar{H}_o \cdot \bar{B}_o^*) dV\right\}. \tag{4-20}$$

Using the vector identities,

$$\bar{H} \cdot \bar{B}^* - \bar{H}_o \cdot \bar{B}_o^* \equiv (\bar{H}_o \cdot \bar{B}^* - \bar{H} \cdot \bar{B}_o^*) + (\bar{B}^* + \bar{B}_o^*) \cdot (\bar{H} - \bar{H}_o)$$

$$\Delta W_m = \left(\frac{1}{4}\right) Re\left\{\int_{V_{tot}} (\bar{H}_o \cdot \bar{B}^* - \bar{H} \cdot \bar{B}_o^*) \, dV\right\} + \left(\frac{1}{4}\right) Re\left\{\int_{V_{tot}} (\bar{B}^* + \bar{B}_o^*) \cdot (\bar{H} - \bar{H}_o) \, dV\right\}. \tag{4-21}$$

Let the second integral component of Eq. 4-21 be denoted

$$A = \left(\frac{1}{4}\right) Re\left\{\int_{V_{tot}} (\bar{B}^* + \bar{B}_o^*) \cdot (\bar{H} - \bar{H}_o) \, dV\right\}.$$

Since the current density inside the volume is zero and there is a linear relationship between $\bar{B}$ and $\bar{H}$, $\nabla \times (\bar{B}^* + \bar{B}_o^*) = 0$ and we can denote $-\nabla \Phi = (\bar{B}^* + \bar{B}_o^*)$, where Φ is a scalar potential. A can then be expressed as [Jac75]

$$A = \left(\frac{1}{4}\right) Re\left\{\int_{V_{tot}} -\nabla \Phi \cdot (\bar{H} - \bar{H}_o) \, dV\right\}$$

$$= \left(\frac{1}{4}\right) Re\left\{\int_{V_{tot}} -\nabla \cdot [\Phi(\bar{H} - \bar{H}_o)] \, dV + \int_{V_{tot}} \Phi \nabla \cdot (\bar{H} - \bar{H}_o)] \, dV\right\}.$$

Using the divergence theorem on the left integral,

$$A = \left(\frac{1}{4}\right) Re\left\{ \oiint_{S_{tot}} -[\Phi(\bar{H} - \bar{H}_o)] \cdot \bar{a}_n \, dS_{tot} + \int_{V_{tot}} \Phi \nabla \cdot (\bar{H} - \bar{H}_o)] \, dV \right\}.$$

Since $\bar{H} = \bar{H}_o$ on S_{tot} when $r \gg R$, and $\nabla \cdot (\bar{H} - \bar{H}_o) = \frac{1}{\mu_r \mu_0} \nabla \cdot \bar{B} - \frac{1}{\mu_0} \nabla \cdot \bar{B}_o = 0$ in V_{tot}, we can specify $A = 0$. With $A = 0$, only the left side integral in Eq. 4-21 remains, and the time-averaged change in stored magnetic energy becomes

$$\Delta W_m = \left(\tfrac{1}{4}\right) Re\left\{ \int_{V_{tot}} (\bar{H}_o \cdot \bar{B}^* - \bar{H} \cdot \bar{B}_o^*) \, dV \right\}. \tag{4-22}$$

We can define $V_{tot} = V_{outside} \cup V_{sphere}$ for regions outside and inside the magnetic sphere, respectively. Outside the volume of the magnetic sphere ($V_{outside}$), $\bar{B}^* = \mu_o \bar{H}^*$. Therefore,

$$\left(\frac{1}{4}\right) Re\left\{ \int_{V_{outside}} (\bar{H} \cdot \bar{B}_o^* - \bar{H}_o \cdot \mu_o \bar{H}^*) \, dV \right\} = \left(\frac{1}{4}\right) Re\left\{ \int_{V_{outside}} (\bar{H} \cdot \bar{B}_o^* - \bar{B}_o \cdot \bar{H}^*) \, dV \right\}$$

$$= \left(\tfrac{1}{4}\right) Re\left\{ \int_{V_{outside}} (\bar{H} \cdot \bar{B}_o^* - \bar{H} \cdot \bar{B}_o^*) \, dV \right\} = 0.$$

The time-averaged change in magnetic energy can now be expressed as an integral over the volume of the sphere (V_{sphere}) only,

$$\Delta W_m = \left(\frac{1}{4}\right) Re\left\{ \int_{V_{sphere}} (\bar{H}_0 \cdot \bar{B}_1^* - \bar{H}_1 \cdot \bar{B}_0^*) \, dV \right\}$$

$$\Delta W_m = \left(\frac{1}{4}\right) Re\left\{ \int_{V_{sphere}} (\mu_r \mu_o \bar{H}_o \cdot \bar{H}_1^* - \mu_o \bar{H}_1 \cdot \bar{H}_o^*) \, dV \right\}.$$

Using Eq. 4-16a,

$$\Delta W_m = \left(\frac{1}{4}\right) Re\left\{ \int_{V_{sphere}} (\mu_r - 1)\mu_o \frac{3}{(\mu_r + 2)} \bar{H}_o \cdot \bar{H}_o^* \, dV \right\}$$

$$\Delta W_m = \left(\frac{1}{4}\right) Re\left\{ \int_{V_{sphere}} (\mu_r - 1)\mu_o \frac{3}{(\mu_r + 2)} {H_o}^2 \, dV \right\}$$

$$\Delta W_m = \pi \mu_o \mathrm{R}^3 Re\left\{\frac{(\mu_r - 1)}{(\mu_r + 2)}\right\} {H_o}^2. \tag{4-23}$$

Here the factor $Re\left\{\frac{(\mu_r-1)}{(\mu_r+2)}\right\}$ represents the real part of the magnetic Clausius-Mossotti factor [Jon95], $K_M = \frac{(\mu_r-1)}{(\mu_r+2)}$.

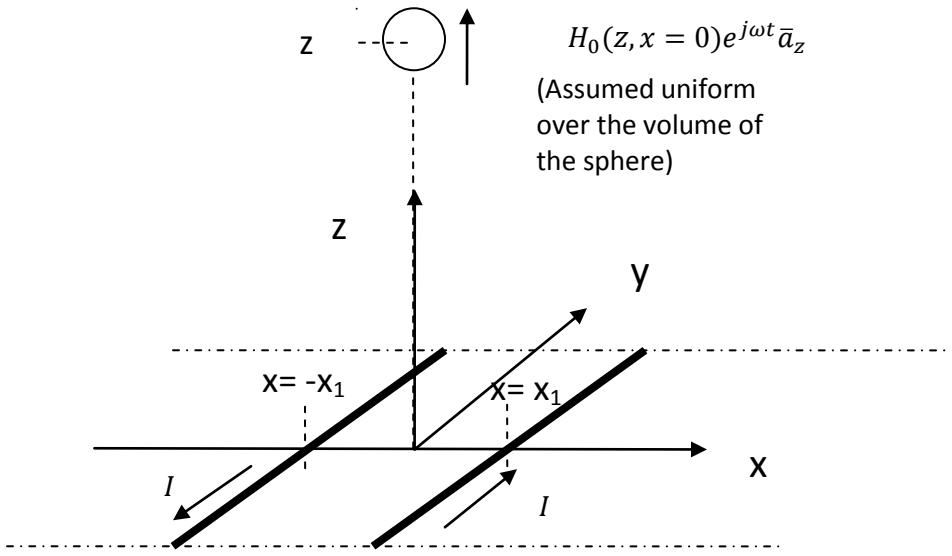

Figure 4-3: A magnetic sphere located at (0, 0, z) is subjected to an approximately uniform magnetizing field, equal to $H_0(z, x = 0)e^{j\omega t}\bar{a}_z$ over the volume of the sphere, which is generated by two infinite conductors situated symmetrically about the origin at $x=x_1$ and $x= -x_1$, carrying current I in opposite directions.

Figure 4-3 depicts a model of the magnetic sphere in the microfluidic channel, suspended over the loop electrode. The magnetic sphere is at an elevation of, z, from the origin along the z-axis. The loop electrode is modeled by two infinite wires carrying a sinusoidal current of magnitude, I, in opposite directions, situated symmetrically about the origin at x = x_1 and x = -x_1, respectively. The magnetizing field generated by the equal but opposite currents is oriented in the $\bar{a}_z$ direction for all elevations for the sphere located at x = 0. The magnetizing field has magnitude $H_o(z, x = 0)$ at an elevation of z, and for spheres with radii, $r \ll x_1,$ is considered uniform over the volume of the sphere. The time-averaged change in inductance, due to a sinusoidal current of magnitude I, can be related to the change in magnetic energy by

$$\Delta L = 4\frac{\Delta W_m}{I^2}. \tag{4-24}$$

Finally, using Eq. 4-24 and referring to Fig. 4-3, the time-averaged change in inductance of the loop due to a single magnetic sphere at elevation z, due to a sinusoidal steady-state current of magnitude I, becomes

$$\Delta L = 4\pi\mu_o \mathrm{R}^3 Re\left\{\frac{(\mu_r - 1)}{(\mu_r + 2)}\right\}\frac{H_o(z, x = 0)^2}{I^2}. \tag{4-25}$$

The field $\bar{H}_0(z, x = 0)$ due to the two infinite, parallel current carrying conductors located at $-x_1$ and x_1 is

$$\bar{H}_0(z, x = 0) = \frac{I}{\pi}\left(\frac{1}{\sqrt{{x_1}^2 + z^2}}\frac{{x_1}^2}{\sqrt{{x_1}^2 + z^2}}\right)e^{j\omega t}\bar{a}_z$$

$$= \frac{I}{\pi}\left(\frac{{x_1}^2}{{x_1}^2 + z^2}\right)e^{j\omega t}\bar{a}_z. \tag{4-26}$$

Chapter 5
Loop Electrode Design

This chapter describes the design of the planar loop electrode, which sits at the bottom of the microfluidic channel, and terminates the centre half-wave transmission line of the coupled-line resonator. The inductance change sensitivity of the whole sensor is determined by the dimensions and the series resistance of this loop electrode. Section 5.1 describes the design of the loop electrode and will emphasize the importance of maximizing the current density and minimizing the resistance. The 2D simulations of various loop electrode dimensions are shown in section 5.2, providing various electrode design constraints. Section 5.3 compares the 3D energy simulations with the 2D model to justify the use of the inductance change equation (Eq. 4-25) derived in Chapter 4. Finally, section 5.4 focuses on the fabricated loops that were used for single magnetic bead detection in this thesis, and provides the magnetic field and inductance change profiles for both loops.

5.1 Current Density and Maximum H field

The half-wave coupled-line resonator that forms the basis of the magnetic inductance sensor is terminated by a planar electrode loop. The series resistance of the loop must be minimized in order to maximize the quality factor of the resonator. The output voltage of the sensor is proportional to the inductance change caused by a single superparamagnetic bead as it passes over the loop electrode. Early experiments,

performed using a large (55 μm wide) loop electrode, showed that the inductance change due to a single bead was very small, as barely noticeable signals were observed even as dozens of beads passed over the previous loop electrode design. The loop electrodes in this thesis were designed to obtain the maximum possible signal from a single bead. It was shown in Chapter 4 that the inductance change caused by a single magnetic sphere was proportional to the factor $\Delta L \propto {H_o}^2/\mathrm{I}^2$, which represents the square of the magnitude of the applied magnetic intensity divided by the square of the magnitude of the current flowing through the loop. The results in Chapter 4 assumed a uniform sinusoidal applied magnetic field $\bar{H}_0 = H_0 e^{j\omega t}\bar{a}_z$. The field inside the magnetic sphere was shown to have azimuthal symmetry (it did not have a $\bar{a}_\emptyset$ component). The applied magnetic field above a loop electrode does not have this symmetry unless the field is far enough away from the ends of the loop. The maximum field lies on or between the inner edges of the electrode loop, and is directed along $\bar{a}_z$ at x=0 (see Fig. 5.1). The magnitude of the applied field $\bar{H}_o$ is not constant but falls off with increasing elevation above the electrode loop (increasing z direction) as shown in Eq. 4-26 for the idealized case of two infinite, opposite and parallel, current-carrying wires. Equation 4-25 can be used for the planar electrode loop case by approximating the applied field by the magnetic field magnitude H_0 (in the absence of the bead) at the elevation of the bead's centre. If the sphere is small compared to the gradient of the applied field, the applied field magnitude can be approximated to be constant throughout the volume of the magnetic sphere.

Increasing the total current through the loop does not increase the inductance change because the magnetizing field scales proportionally with the increase in current. In order to maximize inductance change, the current density must be increased. One

constraint is that the resistance of the loop electrode must be kept low so that the quality factor of the resonator, and therefore the sensor sensitivity, do not become prohibitively low.

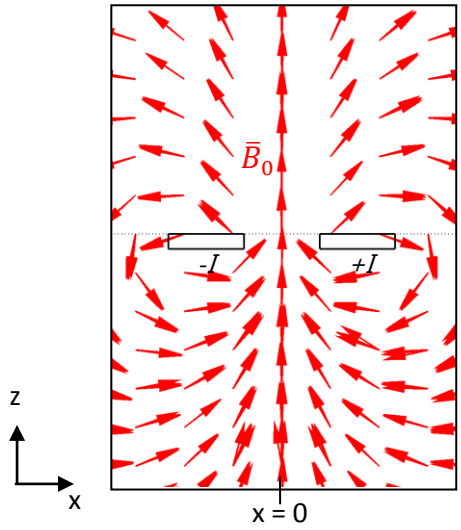

Figure 5-1: A cross-sectional view of a 3D Comsol arrow plot of the normalized magnetic field density $\bar{B}_0$. At x=0, the applied field generated by current, I, is directed in the $\bar{a}_z$ direction, along the length of the loop electrode (far enough away from the ends of the loop).

5.2 Comsol® Simulations for Loop Electrode Designs

The magnetic fields above the planar loop electrode were modeled using 2D Comsol® Multiphysics simulations because the solution is symmetric in the y-direction, referring to Fig. 5.1, assuming that the fields being solved for are a sufficient distance from the ends of the loop electrode. The AC/DC, quasi-statics Perpendicular Induction Currents module was used at a frequency of 1.5 GHz. A 250 μA total current was chosen for each simulation. The electrical conductivity was set to zero everywhere except in the gold conductors, where the conductivity was 4.5×10^7 Siemens/m (see section 6.5). The

geometry used in the 2D Comsol® simulation is shown in Fig. 5.2. The regions outside the electrode were assumed free-space. The parameters considered for the electrode design were the width, thickness, and spacing. The channel height was set to 40 µm above and below the top of the loop electrode, and the channel length was set to 100 µm. Magnetic insulation ($\bar{n}\,X\,\bar{A}=0$) was assumed at the top and side wall boundaries because the boundaries were far enough from the electrode that this was a reasonable approximation to an infinite free-space enclosure.

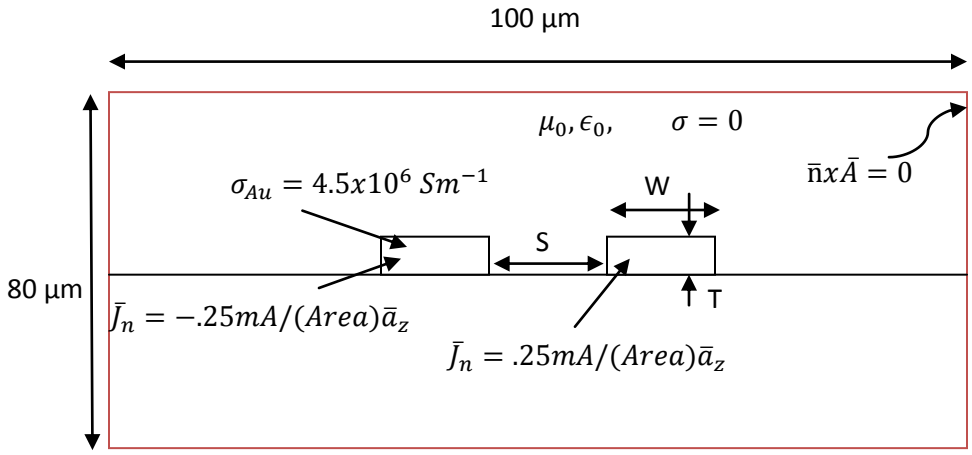

Figure 5-2: Longitudinal section of channel. Geometry and boundary conditions used for 2D Comsol® quasi-statics perpendicular induction currents module simulations.

To determine the maximum possible magnetic field intensity for a total current of 250 µA, several loop designs were simulated, and the square of the magnitude of the magnetizing field, $|\bar{H}|^2$, was compared at an elevation of 2.5 µm above the top of the electrode. This elevation is approximately the radius of an M-450 Dynabead® sphere, which flows near the bottom of the channel for small flow velocities due to its large mass density. Table 5.1 shows the maximum field at a 2.5 µm elevation, ${H_{max}}^2|_{h=2.5\mu m}$, for

various loop dimensions. A reduction in loop spacing has the effect of increasing the maximum field. Increased spacing, however, makes the magnetic field above the electrodes less sensitive to elevation, which has the effect of reducing signal variability for beads flowing at different elevations. From theoretical resistance calculations, a minimum cross-sectional area of approximately 3 μm^2 was chosen to keep the theoretical loop resistance below 2 Ω. This cross-sectional area would result in a resistance of approximately twice that amount, as the deposited Au conductivity from previous fabricated electrode loops was half the bulk value. The current density was therefore limited to 83.33 x 10^6 [Am^{-1}] for a 250 μA total current. Reducing the width of the electrode loop increased the maximum field substantially, as did reducing the thickness, albeit to a lesser extent. The minimum feature size that could be reliably fabricated in the NSFL clean room was approximately 3 μm, therefore the lower limit for the designed loop width and thickness was chosen to be 3 μm and 1 μm, respectively. Given the constraints stated above, the highlighted boxes in Table 5.1 represent the optimal design dimensions for the loop electrode, which produced the maximum change in inductance. To reduce the number of fabrication steps, glass slides were purchased that had a 100nm thick gold layer. As will be explained in Chapter 6, to increase the thickness of the electrode, gold was electrochemically deposited to the thickness specified by the final design. A minimum loop spacing of 5 μm was chosen to avoid a short between the electrodes after the deposition of gold. Gold deposition would lead to decreased spacing due to the isotropic nature of the deposition process. The smallest dimensions that were chosen for fabrication were a loop with a 3 μm width and 5 μm spacing, and a loop with a 5 μm width and 5 μm spacing. An array of other loop electrodes was also designed with

varying dimensions, in increments of 5 μm. The final electrode thickness was designed to be 1000 nm after gold deposition.

Width (μm)	Spacing (μm)	Thickness (nm)	$H_{max}{}^2\|_{h=2.5\ \mu m}$ (A^2/m^2)	$(H_{max}{}^2/I^2)$ (m^{-2})	$\Delta L(\mu_r=1.2)$ (fH)
30	30	1000	1	$16x10^6$	0.2
30	30	100	16	$256\ x10^6$	2.9
30	15	100	19	$304\ x10^6$	3.4
30	5	100	28	$448x10^6$	5.0
15	15	200	43	$688x10^6$	7.7
15	5	200	60	$960x10^6$	10.8
10	5	300	84	$1344x10^6$	15.1
5	5	600	120	$1920x10^6$	21.6
5	3	600	133	$2128x10^6$	23.9
4	3	750	136	$2176x10^6$	24.4
3	5	1000	124	$1984x10^6$	22.3
3	3	1000	133	$2128x10^6$	23.9
2	3	1500	112	$1792\ x10^6$	20.1

Table 5-1: Gold electrode loop dimensions and simulated maximum magnetizing field at an elevation of 2.5 μm above the loop electrode for a 250 μA current. Shaded region represents optimum dimensions.

5.3 Comsol® Energy Simulations

In order to verify the validity of using a 2D model for simulating the field above the electrode loop, a 3D Comsol® Quasi-EM model was used to simulate the change in magnetic energy due to a magnetic bead. The simulation involves the calculation of the total magnetic energy change due to a 2.25 μm radius sphere (centred at x = 0 at an elevation of z = 4.5 μm, with a relative magnetic permeability of μ_r = 1.2). To avoid errors arising from using varying mesh elements, the total magnetic energy in the volume outside the electrode loop is calculated for two cases: magnetic energy calculation in the presence of a 2.25 μm radius sphere with μ_r = 1.2, and magnetic energy calculation in the presence of a 2.25 μm radius sphere with μ_r = 1. The 3D Comsol® model is shown in Fig. 5-3. The top, bottom and side ($x = \pm 50\mu m$) wall boundary conditions are all magnetic insulation ($\bar{n} \times \bar{A} = 0$) boundaries, since the wall boundaries are far enough from the loop electrode that the fields there are negligible. Because $\bar{B} = \nabla \times \bar{A}$, and $\bar{B}$ is tangential to the front and back wall boundaries ($y = 0\ \mu m, 40\mu m$), $\bar{a}_y \times \bar{A} = 0$, resulting in magnetic insulation boundaries.

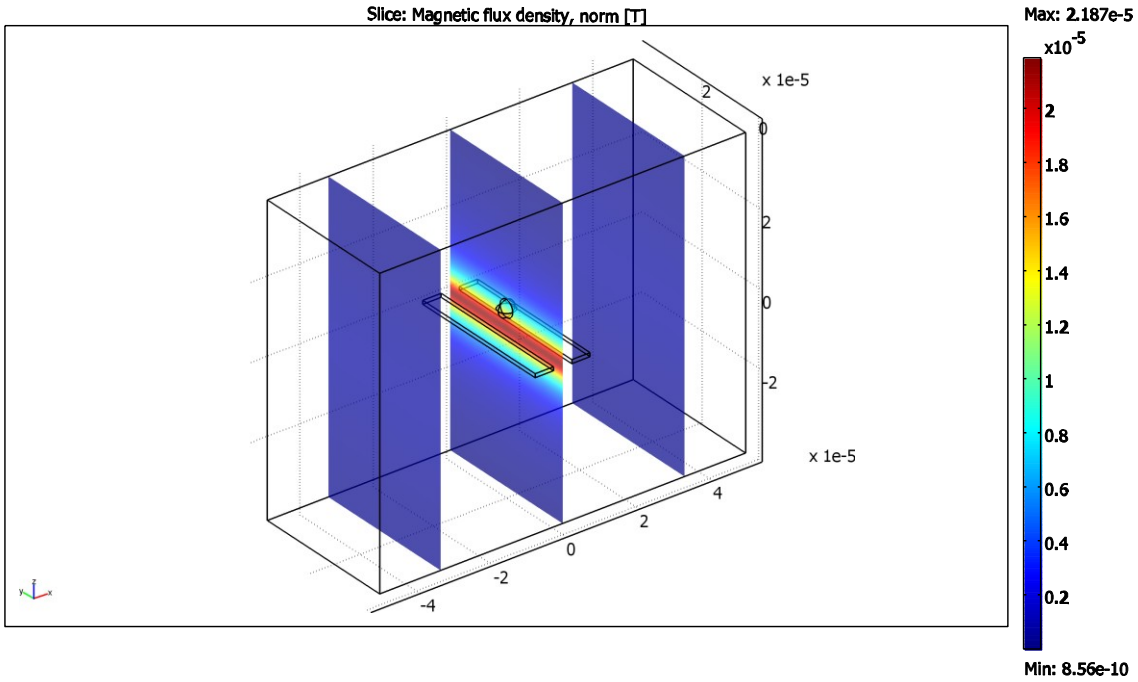

Figure 5-3: 3D Comsol® Quasi-EM model used to simulate change in magnetic energy caused by the presence of a 2.25 μm sphere of relative magnetic permeability, μ_r = 1.2.

The electrode loop was modeled as two 5 μm wide, and 1 μm thick sections of metal ($\sigma = 27\ x\ 10^6\ Sm^{-1}$), spaced 5 μm apart. The electrode wall boundaries are current densities equal to the current densities inside the electrode, where the right electrode in Fig. 5-3 has a current density of $\bar{J}$ = 50x10^6 $\bar{a}_y$ A/m^2, and the left electrode has a current density of $\bar{J}$ = -50x10^6 $\bar{a}_y$ A/m^2. The total magnetic energy was calculated using subdomain integration of the magnetic energy density within the volume outside of the electrodes for the $\mu_{r(sphere)}$ =1.2 and $\mu_{r(sphere)}$ = 1 cases. The change in magnetic energy was calculated by subtracting the two energy values, yielding

$$\Delta W_m \cong 1.61x10^{-22}\ \text{J}.$$

Fig. 5-4 shows a comparison of the magnetizing field variation at a constant 4.5 μm elevation (without the presence of a magnetic bead) using the 2D and 3D models. The 3D model field variation shows some error due to inadequate mesh element refinement. However, the two models are in close agreement with each other. The maximum field at a 4.5 μm elevation for the 2D and 3D models is approximately ${H_{max}}^2 \cong 56\, A^2 m^{-2}$. Using this value in Eq. 4-23, the estimated change in magnetic energy is

$$\Delta W_m = \pi \mu_o \mathrm{R}^3 \mathrm{Re}\left\{\frac{(\mu_r - 1)}{(\mu_r + 2)}\right\} {H_o}^2$$

$$\Delta W_m = \pi \mu_o (2.25\mathrm{x}10^{-6})^3 (\tfrac{0.2}{3.2})(56) \cong 1.57x10^{-22}\mathrm{J}.$$

The estimated change in magnetic energy using Eq. 4-23 is therefore within 2.5% of the value obtained using 3D energy calculations. Using the magnetic field, calculated using the 2D model without the sphere, at the centre of the magnetic sphere with Eq. 4-23 therefore provides a good approximation to the change in magnetic energy caused by a single magnetic sphere, even when the size of the sphere is large compared with the gradient of the field.

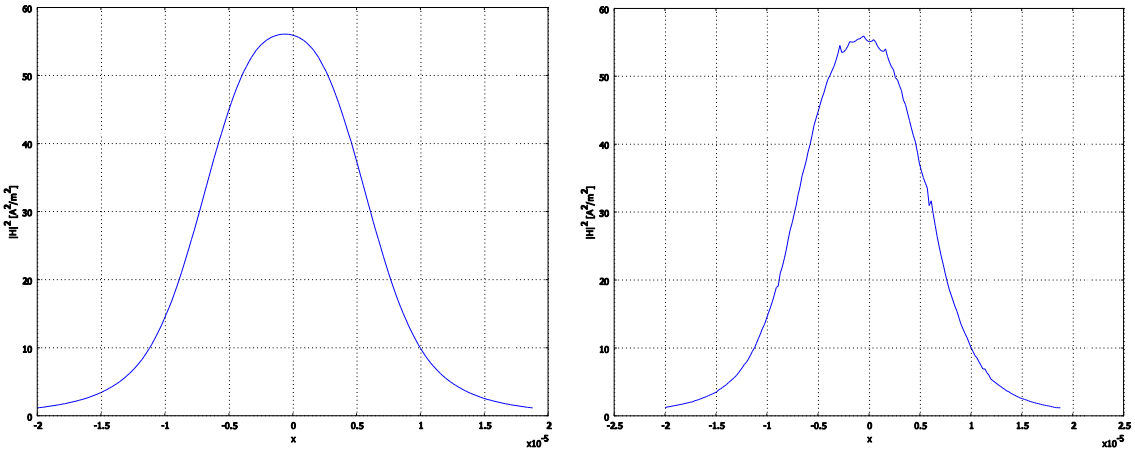

Figure 5-4: 2D (left) and 3D (right) Comsol® models of magnetizing field variation at a constant 4.5 μm elevation above an electrode loop that is 5 μm wide, 1 μm thick, and spaced 5 μm apart.

5.4 Comsol® Simulation of Fabricated Electrodes

The two loop electrodes used to detect single 4.5 μm magnetic beads were designed to have 5 μm spacing, and 3 μm and 5 μm widths, respectively. After fabrication, the larger loop (which will be called Loop 1) had a 5.7 μm width and 2.3 μm spacing. After fabrication, the 3 μm width loop (which will be called Loop 2) had a 3.4 μm width, and spacing of 2.8 μm. All the loops had a 1.1 μm total thickness after electrochemical deposition (described in Chapter 6). The measured conductivity of the fabricated gold loop electrode is $27x10^6\ Sm^{-1}$. The square of the magnetizing field variations,$|\overline{H}|^2$, for constant elevations above Loop 1, due to a 0.25 mA current, are shown in Fig. 5.5. The elevations would represent different possible flow trajectories for the particles as they pass over the electrode. The elevations range from 0.25 μm to 4.5 μm. Although the centre of magnetic bead cannot be lower than 2.25 μm, it is worth

noting that the average field throughout the bead as it crosses the inner electrode region could be higher or lower than the value at its centre. The square of the magnetizing field variations,$|\bar{H}|^2$, for constant elevations above Loop 2 are shown in Fig. 5.6. The magnetizing field gradient for Loop 2 is greater than for Loop 1, resulting in greater inductance change sensitivity to bead elevation.

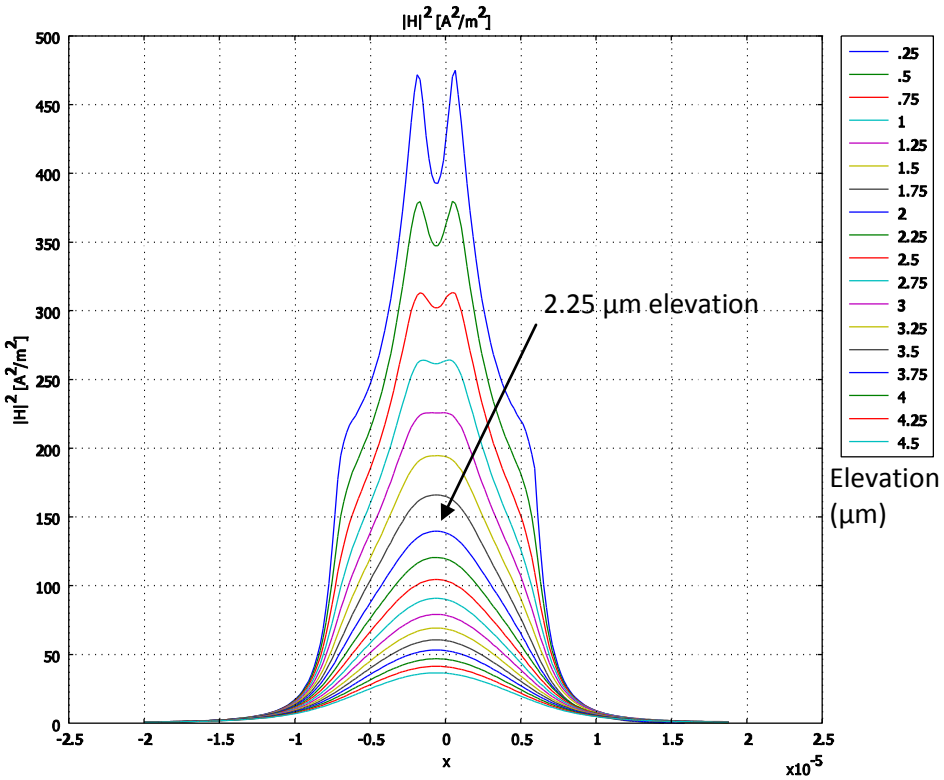

Figure 5-5: Magnetizing field variation for constant elevations above the Loop 1 electrode due to a 0.25 mA current. The top curve and bottom curve represent the field variation at a 0.25 µm elevation and 4.5 µm elevation, respectively.

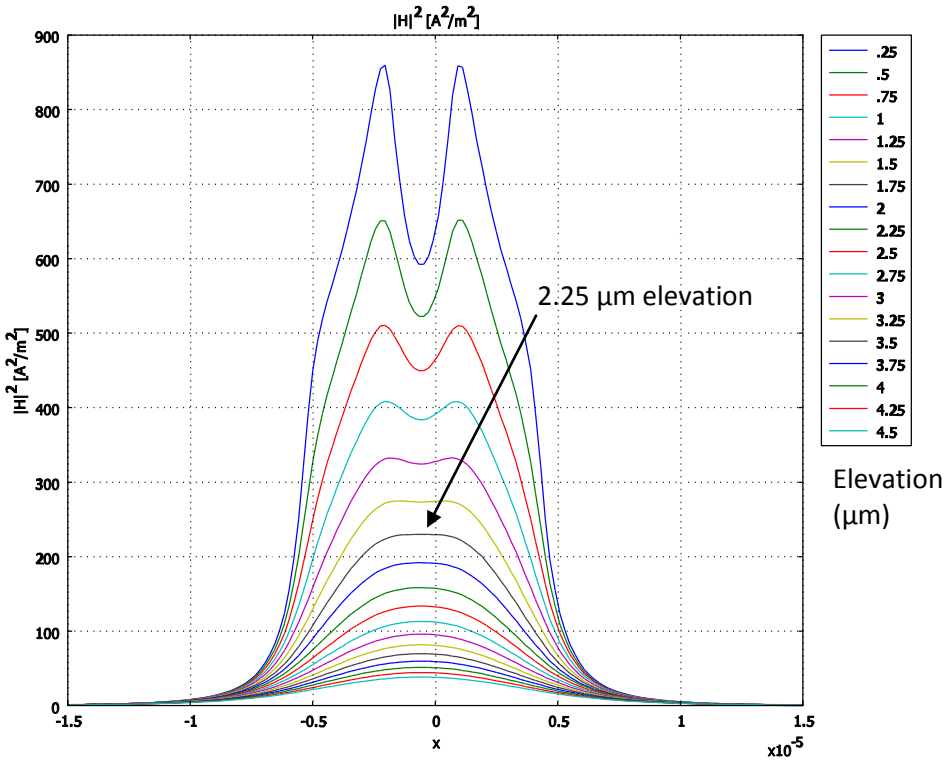

Figure 5-6: Magnetizing field variation for constant elevations above the Loop 2 electrode for a 0.25 mA current. The top curve and bottom curve represent the field variation at a 0.25 µm elevation and 4.5 µm elevation, respectively.

For a 4.5 µm diameter bead flowing at the minimum elevation of 2.25 µm (vertical distance from the top of the electrode loop to the centre of a bead), and for a current of I = 0.25 mA, the square of the magnitude of the external field at a position between the electrodes (x=0) is 108 A^2m^{-2} for Loop 1 and 138 A^2m^{-2} for Loop 2. The maximum change in inductance for each loop electrode caused by a single passing magnetic bead can be estimated using Eq. 4-25,

$$\Delta L = 4\pi\mu_o R^3 \mathrm{Re}\left\{\frac{(\mu_r-1)}{(\mu_r+2)}\right\}\frac{{H_o}^2}{I^2}.$$

The change in magnetic energy, estimated using equation 4-23 and an external magnetizing field of 138 A^2m^{-2} at an elevation of 2.5 μm, is

$$\Delta W_m = \pi\mu_o \mathrm{R}^3 \frac{0.2}{3.2}(138) \cong 3.88x10^{-22} \text{ J.}$$

The change in magnetic energy for the Loop 2 geometry was verified using the 3D Comsol® model described in section 5.3. The bead elevation was set to 2.5 μm and centered between the inner electrode edges. The bead had an effective relative permeability of $\mu_r = 1.2$. The simulated change in magnetic energy for Loop 2 was

$$\Delta W_{m(Loop2)} \cong 3.677x10^{-22} \text{ J.}$$

The estimated value is approximately 5.5 % too high but provides a reasonably accurate result, despite the high magnetic field gradient of Loop 2. The 3D simulation energy value could be slightly inaccurate due to finite mesh errors.

The estimated change in magnetic energy corresponds to a time-averaged change in inductance of

$$\Delta L_{|Loop2} = \frac{4\Delta W_m}{I^2} = 4\,\pi\mu_o \mathrm{R}^3 \frac{0.2}{3.2}(138)/(.25x10^{-3})^2 \cong 3.88x10^{-22} \cong 25 \text{ fH,}$$

for a bead elevation of 2.5 μm. The inductance change profiles for Loop 1 and Loop 2 are shown in Fig 5-7, starting from the minimum bead centre elevation of 2.25 μm. The bead is assumed to be homogeneous with a real relative permeability of $\mu_r = 1.2$.

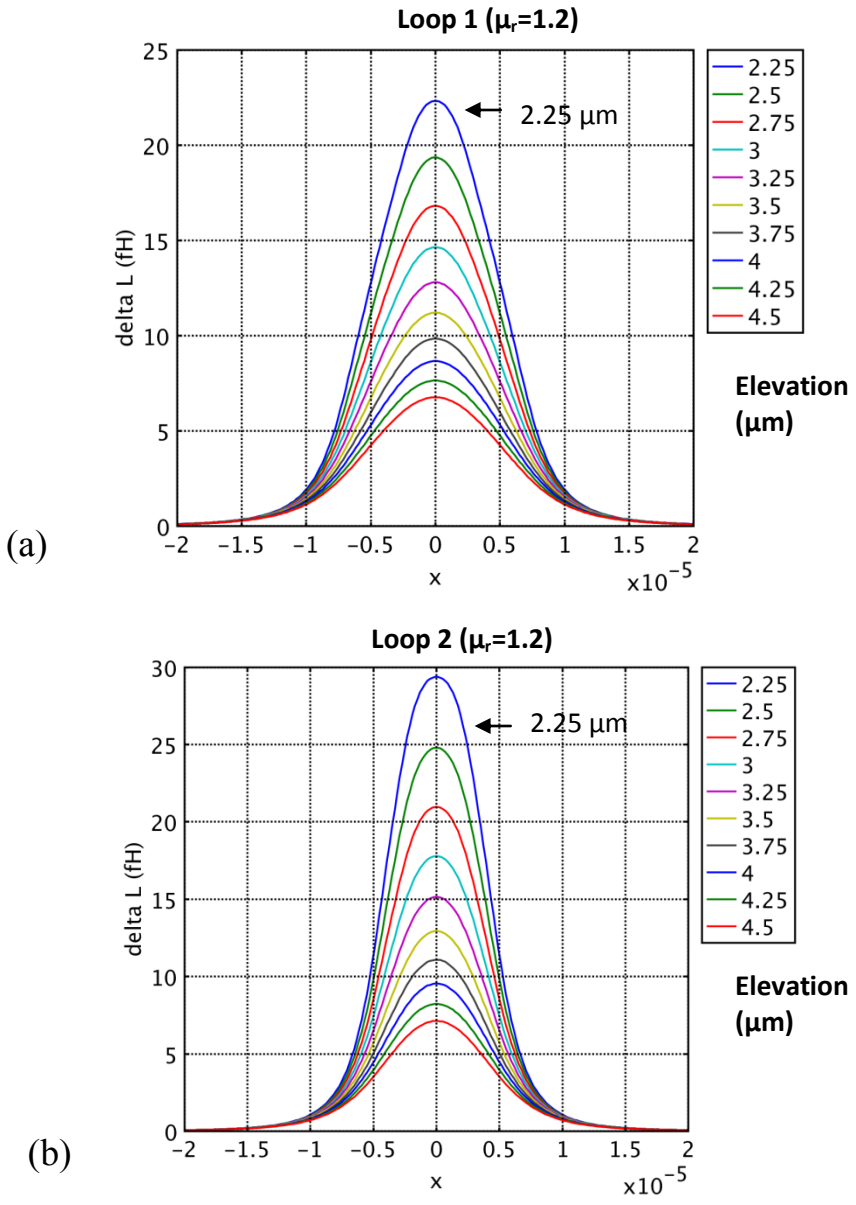

Figure 5-7: Inductance change profile for constant bead elevations. (a) Loop 1 inductance change profile for a bead with effective permeability, μ_r=1.2. (b)Loop 2 inductance change profile for a bead with effective permeability, μ_r=1.2.

Chapter 6
Electrode & Microfluidic Chip Fabrication

The fabrication of the planar electrode array is described in sections 6.1 and 6.2. Section 6.3 describes the electrochemical gold deposition procedure used to increase the electrode layer thickness. Section 6.4 describes the PDMS channel mould fabrication steps, and the assembly of the microfluidic chip. The last section covers the series resistance measurements of the two loops.

6.1 Photolithography

The basic fabrication steps for the microfluidic chip assembly are depicted in Fig. 6-1. A positive chrome mask (chrome mask on a glass substrate) was designed using L-edit CAD software. An array of electrode loops was drawn with various loop widths and spacing. The smallest loop was designed to have a 3 μm width and 5 μm spacing. The CAD design was sent to the University of Alberta for fabrication of the mask. The fabricated chrome mask was then used in the clean room facilities of the Nanosystems Fabrication Laboratory (NSFL) to perform photolithography and to etch the electrodes with the help and guidance of Dr. Jun Hui and Dwayne Chrusch.

Three 45 mm x 15 mm glass slides with a 10 nm titanium adhesion layer and a 100 nm gold surface layer were purchased. Each slide was placed on a spinner and spun at 500 rpm for 5 seconds while pouring positive photoresist (HPR 504). The spin speed

was increased to 4000 rpm for 30 seconds to achieve a uniform photoresist thickness of approximately 1.4 to 1.5 μm. A soft bake was then performed at 100° C for 100 seconds. The slide was fixed in place and the positive chrome mask design was aligned over the glass slide. The design was exposed to a UV light source for 10 seconds. For positive photoresist, the exposed photoresist surface is removed with developer while the unexposed photoresist, corresponding to the mask design, remains.

Following UV exposure, a hard bake was performed at 120° C for 20 minutes. The slide was subsequently immersed in 701 developer for 30 seconds then washed with water and dried with compressed air. If there was a problem with photoresist uniformity (there was a tendency for build-up near some corners of the rectangular glass slide) the photoresist was washed off with acetone into a funnel, followed by isopropanol, and deionized (DI) water. The photoresist was then re-applied as needed.

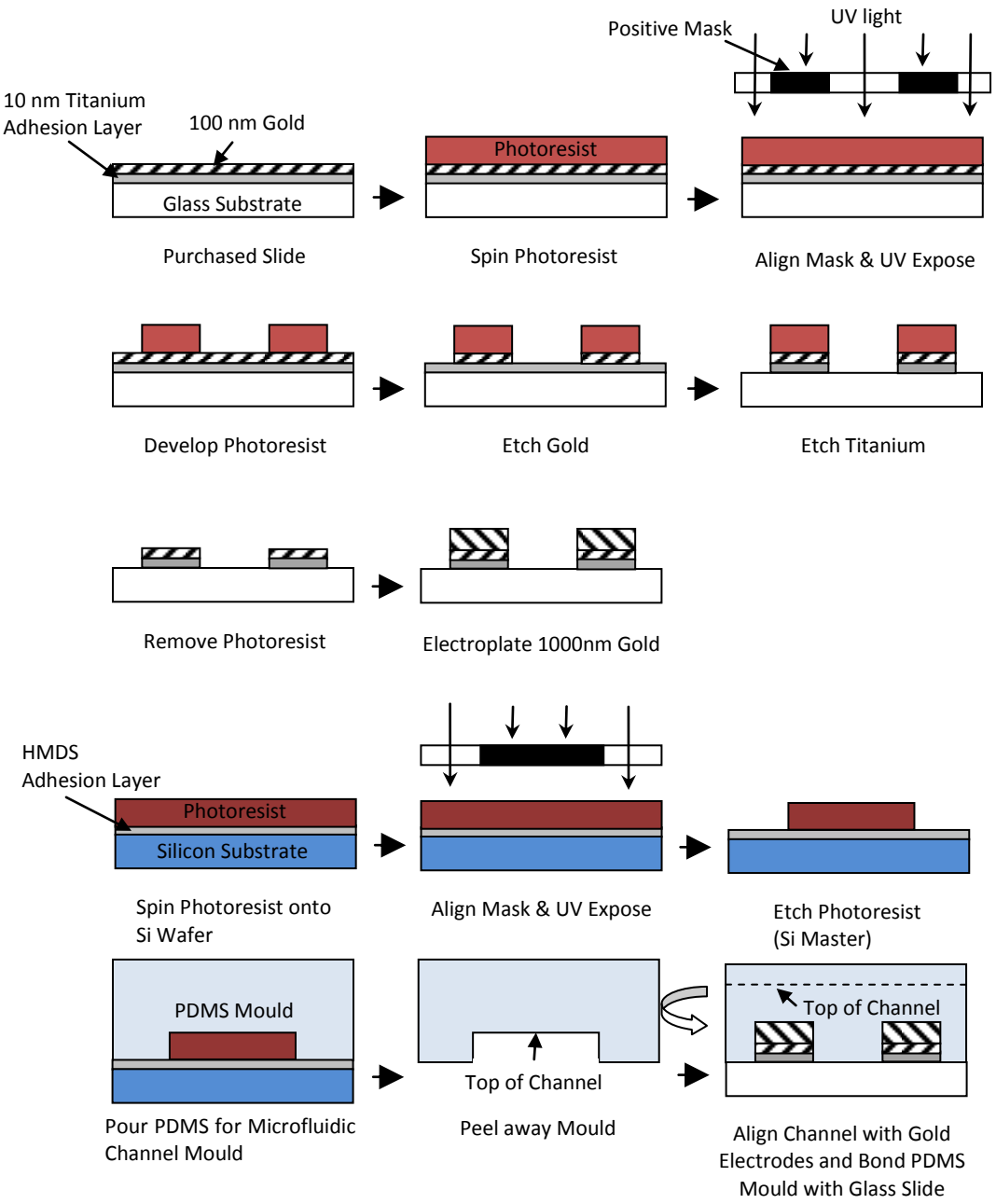

Figure 6-1: Planar gold electrode and PDMS channel mould fabrication steps (Dimensions are not to scale).

6.2 Gold and Titanium Layer Etching

Before etching the gold (Au) at wet deck #1 in the NSFL, the plenum flush was turned on to ensure proper ventilation before using the Au and Ti etches. The gold etch that was used was potassium iodide (KI) with a mixing ratio of $I_2 : KI : H_2O = 1\ g : 4\ g : 40\ mL$. The glass slide was immersed in a beaker containing 400 mL of KI solution for 20 seconds to etch approximately 100 nm of Au. The slide was removed and washed with DI water. The beaker contents were poured into a storage bottle and the beaker was then washed with DI water.

The Ti layer was etched using a buffered-oxide etch (BOE) containing hydrofluoric acid (HF). The glass slide was placed into a labeled BOE beaker for approximately 1 minute to etch the 10 nm Ti layer, and was then placed into a beaker of DI water. Each slide was rinsed thoroughly. The BOE was poured back into the bottle and capped. BOE neutralizer was poured into the labeled BOE beaker and dumped. The beaker was then rinsed with DI water and dumped a total of 5 times to ensure that no BOE remained. The plastic holders used for each slide were rinsed and replaced by clean metal holders to ensure that no remnant BOE remained on the holders and slides. Finally, the remaining photoresist was removed using acetone, followed by isopropanol, and DI water.

6.3 Electrochemical Deposition

Following etching, the total thickness of the Au layer was 100 nm. Given the small loop dimensions, the loop series resistance was too high for such a thin layer. To

provide an acceptable resistance value, the thickness of the electrodes was increased by approximately 1 μm. The extra thickness was achieved by electrochemical deposition of Au. The electrode array was originally designed with electrochemical deposition in mind. Each electrode loop was designed to be shorted by a 15mm x 1 mm Au strip to facilitate the bonding of a copper wire. The wire bond was covered with PVC glue to avoid electroplating the connection. The copper wire was then attached to an alligator clip so that it could be immersed in the Au solution. Sulphuric Acid, at a concentration of 0.5 M, was used to clean the Au electrodes. A mixture of one part Oromerse SO Part B with 10 parts 1.7 M Na_2SO_4 was used to make the Au solution. This was diluted to a 1:20 solution. A PH greater than 8.9 was ensured for the Na_2SO_4 solution to enable even plating [Pil10].

Figure 6-2 shows the basic setup for electrochemically depositing Au onto a sample electrode surface. A CH Instruments (CHI-760C) bipotentiostat workstation was used to maintain a constant potential between a silver chloride (AgCl) reference electrode and the glass sample (working electrode). Any change in potential between the reference and working electrodes is cancelled by the current passing through a Platinum counter electrode. Using a technique called cyclic voltammetry (CV), a current versus potential curve was recorded using a computer interface for a scanning potential window of 0 to -1.1 V, at a rate of 50 $mV \cdot s^{-1}$. A potential of -0.9 V was used for electrochemical deposition. This value was arrived at based on the previous electrochemical Au deposition experience of Matt Pilapil [Pil10]. A higher potential would increase the deposition rate but would also cause a more uneven deposited Au layer and would increase the resistivity. Furthermore, at potentials less than -1.0 V, H_2 evolution was

reported to occur by Pilapil and his colleagues, causing the destruction of the Au and Ti seed layers. The estimated Au electrode surface area of the sample was estimated to be 0.27 cm^2. It was reported by Pilapil and his colleagues that 0.8 C of charge was required per cm^2 of surface to electroplate a 1 μm thick layer of Au. Therefore, electrochemical deposition was performed until a total charge of 0.8 x 0.27 = 216 mC was reached in order to plate 1 μm. The total Au thickness was measured to be 1.1 μm using the profilometer in the NSFL.

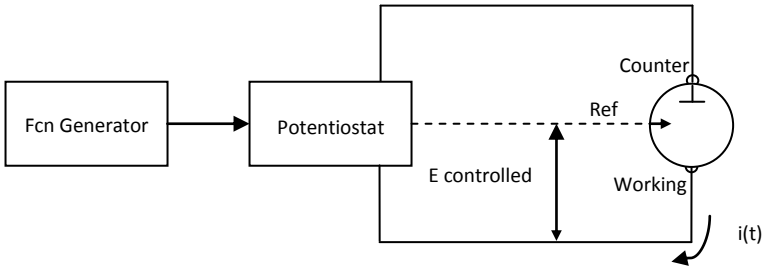

Figure 6-2: Electrochemical Deposition of Au. An Ag/AgCl reference electrode, Pt counter electrode, and Glass sample with Au electrode layer (working electrode) immersed in a beaker with Au solution. A bipotentiostat workstation was used to record and control the deposition speed and duration.

The fabricated Au electrode loop array is shown in Fig. 6-3. Note that the loops are shorted by a 1mm wide strip of Au that was used to connect all the loops with a wire when immersing the sample in the Au solution during electrochemical deposition. This strip was later removed using a wafer saw. A close-up of one of the loop electrodes is shown in Fig. 6-4. This loop was designed to be 5 μm wide with 10 μm spacing. Using a microscope, the fabricated dimensions were estimated to be 5 μm wide with 7 μm spacing. The spacing was usually smaller than the design spacing because of the isotropic electroplating of Au. The two electrode loops used in this thesis to detect single 4.5 μm

superparamagnetic Dynabeads® were designed to be 3 µm wide with 5 µm spacing and 5 µm wide with 5 µm spacing, respectively. The fabricated loops were measured using a microscope. The measured dimensions of the smaller loop electrode (Loop 2) were approximately 3.4 µm for the loop width and 2.8 µm for the loop spacing. The larger loop electrode (Loop 1) had a measured width of 5.7 µm, with 2.3 µm loop spacing.

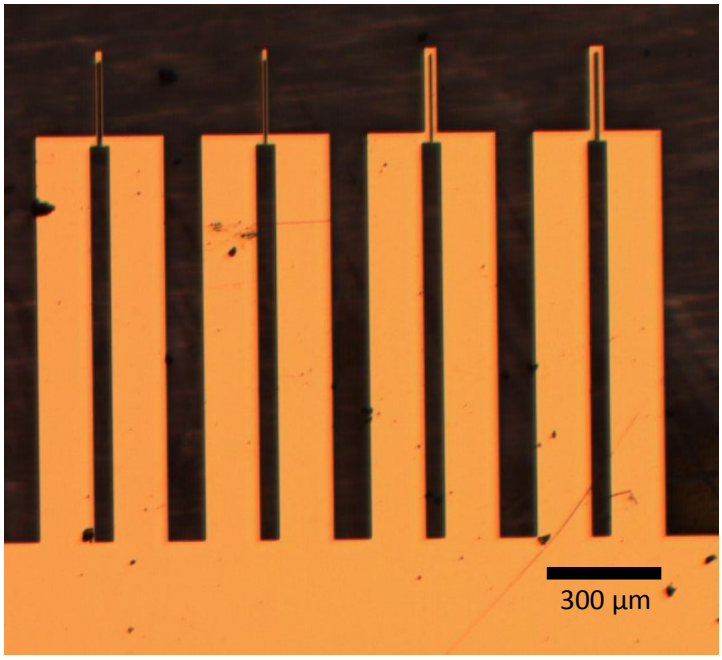

Figure 6-3. Au electrode array. Electrochemical deposition of Au increased the thickness to approximately 1.1 µm. The connection bar shown at the bottom was later isolated using a wafer saw.

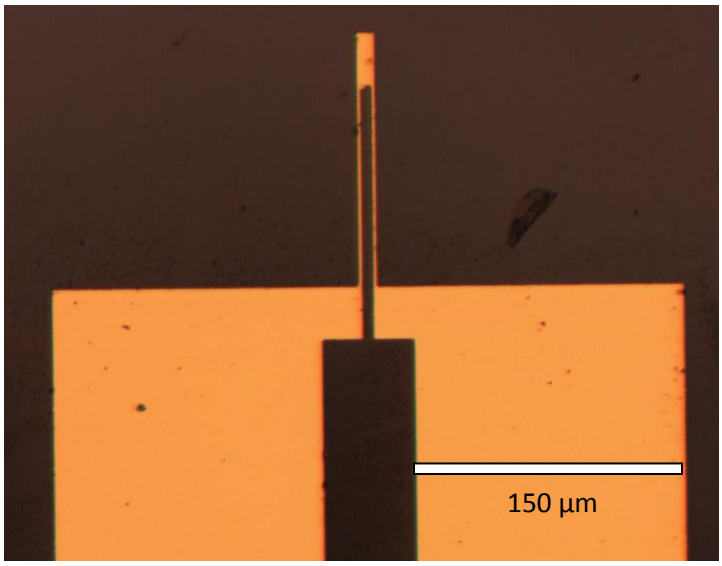

Figure 6-4. Au electrode loop electrode. This loop is approximately 5µm wide, 110µm long (excluding the wider end portion at the top), with 7µm spacing (designed for 5 µm width and 10 µm spacing). The contact pads are 150µm wide.

6.4 PDMS Channel Mold Fabrication

The microfluidic channels were fabricated using polydimethylsiloxane (PDMS) in the NSFL clean room facility. PDMS is a clear and soft material, and the channels can be fabricated and tested with a quick turnaround time, which is important when designing a prototype. Furthermore, since the electrodes were electroplated and were not flush with the glass substrate, PDMS was a good material to use because it molded around the contours of the electrodes and ensured proper sealing.

The channels were designed using L-edit CAD software. A negative transparency mask was drawn at 2400 dpi. The transparency was fabricated by OCT digital. The CAD

design is shown in Fig. 6-5. Certain designs incorporated vacuum channels around the microfluidic channels to increase the reversible bond strength by using a vacuum pump. This approach was not successfully used in this thesis, however. The channels were fabricated by first fabricating a photoresist mould master on a 3" Si wafer. Multiple microfluidic channels could then be fabricated by pouring PDMS over the Si master and peeling the channels away after curing.

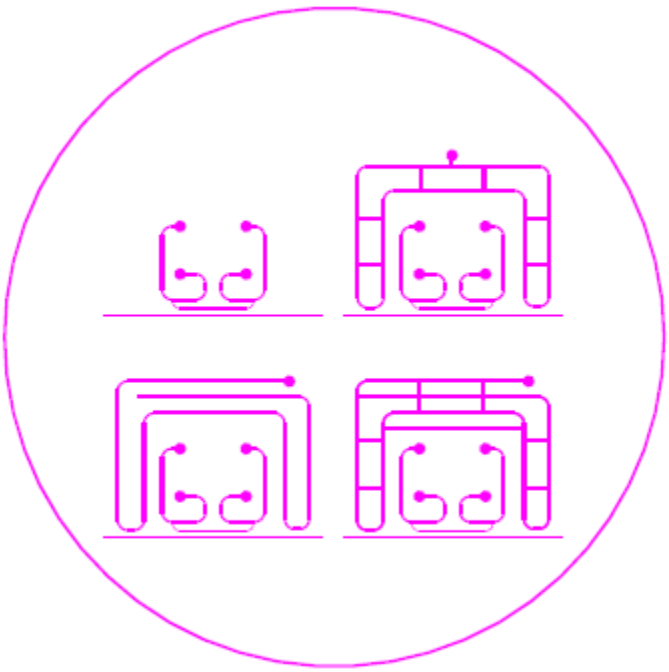

Figure 6-5: PDMS channel design using L-edit CAD software. Four separate microfluidic channel designs lie inside a 3" Si wafer outline. Outer channels represent vacuum channels. Each design has a cut line used as a guide when cutting with a knife along the bottom cross-channel.

The 3" Si wafers were first cleaned with H_2SO_4 and H_2O_2 (4:1) for 5 minutes. An HMDS layer was deposited to ensure proper adhesion of the SU-8 photoresist to the wafer when peeling off the PDMS. The transparency masks were cut and taped flat to a

piece of glass. The wafers were pre-baked at 65˚ C for 2 minutes to remove moisture. SU-8 2025 was poured slowly onto each wafer, ensuring that the bottle was close to the wafer to minimize bubble formation. The SU-8 covered glass was then spun at 1000 rpm for 30 seconds (for a 25-30 micron thickness). A soft bake was performed for 5 minutes at 95˚ C. The design was exposed to UV light for 20 seconds, baked for 5 minutes at 95˚ C, and then developed for 2 minutes and 30 seconds. Several Si master designs were fabricated

The PDMS was made by combining 25 mL Sylgard 184 Si Elastomer base with 2.5 mL Sylgard 184 Si Elastomer curing agent in a beaker. The solution was mixed for 3 to 4 minutes then poured onto the Si master designs inside of a Petri dish. The dish was subsequently placed inside a dessicator for 5 minutes to get rid of bubbles, and pressurized canned air was used to gently remove any remaining surface air bubbles. Upon removal of all the bubbles, the Petri dish was placed in an oven and baked for 2 hours at 70˚ C. An Exacto knife was then used to cut around the designs. The PDMS was then gently peeled away from the Si master. The designs were placed on a clean glass surface, and any dust or photoresist residue was removed from the PDMS with scotch tape. Port openings were created by punching holes through the PDMS. The port openings were covered with tape to prevent dust from entering the channels. The front edge (where the microfluidic channel is less than 1 mm away from the edge of the PDMS) of each PDMS design was cut using the cut line as a guide. Figure 6-6 shows the PDMS design reversibly bonded to a glass slide with polyethylene tubing inserted into the port openings.

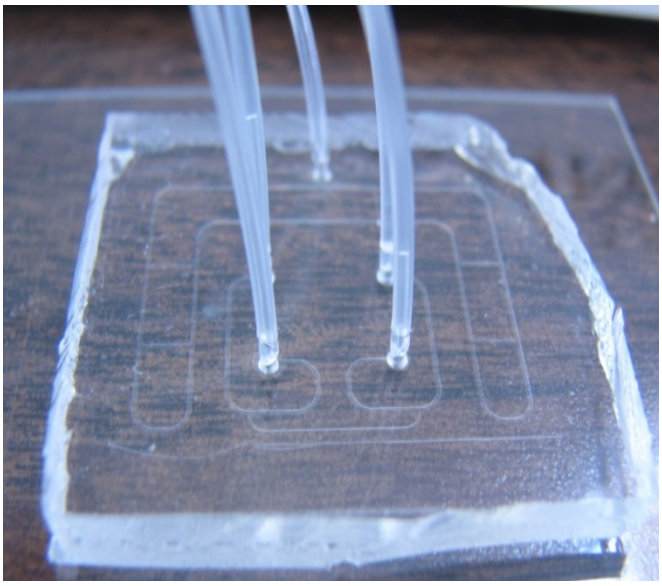

Figure 6-6: Fabricated PDMS mould reversibly bonded to a glass slide. Microfluidic channels are located at the bottom of the PDMS mould.

The microfluidic chip used in this thesis was built by reversibly bonding the PDMS channel design to the glass electrode array. Scotch tape was used to ensure clean PDMS channel and glass surfaces. The two surfaces were then bonded by aligning and pressing them together by hand. A microscope was used to align the PDMS with the glass sample so that the electrode loops spanned the cross-channel. This approach provided for a water-tight seal but the bond could not withstand much pressure (approximately 5 psi); since PDMS channels are hydrophobic, this presents a serious draw-back. The reversible-bond approach was used because only one deposited electrode array that was fabricated had acceptably low loop series resistance values. The benefit of using this reversible approach lies in being able to reuse the same electrode and even the same PDMS channel design by cleaning, drying, and re-bonding both surfaces after a leak occurs, or in order to clean and remove particle debris in the channel after use. A more reliable approach

would be to place the PDMS and the glass in an ozone plasma chamber, and then carefully aligning and irreversibly bonding them together.

After proper alignment and bonding, holes were drilled in a Plexiglas block (for the channel port openings) which was then placed on top of the PDMS design. These holes were made slightly bigger to ensure that polyethylene tubing could be easily inserted through the block and into the PDMS ports. The microfluidic chip was then fastened inside the EMI probing chamber. Finally, small clamps were fastened inside the EMI enclosure and used to apply downward pressure on the tubing to ensure proper channel sealing. Figure 6-7 (a) illustrates the alignment of the microfluidic channel with the electrode array. The final microfluidic chip assembly is shown in Fig. 6-7 (b). An alternative alignment was also used for some measurements, where the electrode array was aligned with one of the larger channels.

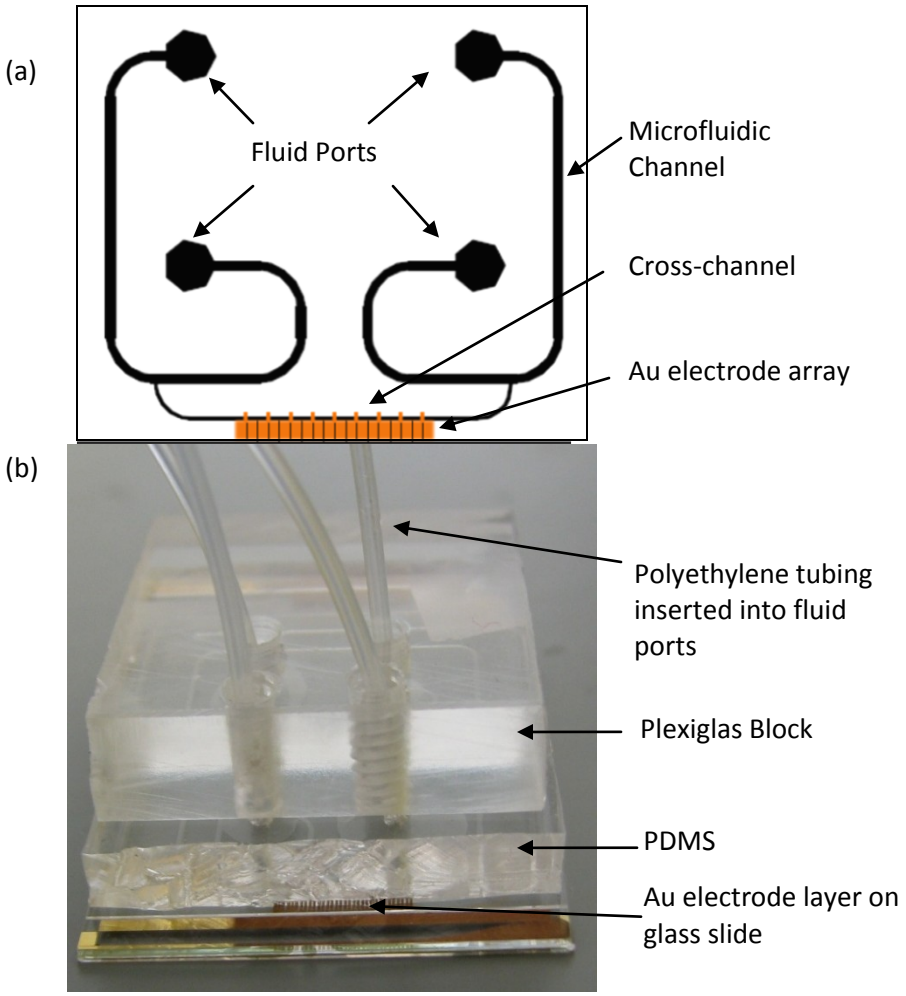

Figure 6-7: (a) Alignment of microfluidic channels with Au electrode loop array. (b) Fabricated PDMS mould reversibly bonded to a glass slide. Microfluidic channels are located at the bottom of the PDMS mould.

6.5 Series Resistance of Fabricated Loop Electrodes

At 1.49 GHz, the skin depth in a gold conductor with a bulk theoretical resistivity $\rho = 2.44\, x10^{-8}\Omega \cdot m$ is $\delta_s = (\rho/\pi f \mu_0)^{1/2} \cong 2\ \mu m$. Therefore, the resistance in a 1.1 µm thick gold electrode is approximately equal to its dc resistance. Figure 6.8 shows the dimensions (not to scale) of the two loops used to detect single 4.5 μm magnetic beads in this work. The theoretical dc resistance of the Loop 1 electrode in Fig. 6-8 (between the two lower edges of the large contact pads) is

$$R_{Loop1} \cong \frac{2\rho 400}{(1.1x10^{-6})(150)} + \frac{2\rho 110}{(1.1x10^{-6})(5.7)} + \frac{\rho 14}{(1.1x10^{-6})(30)}$$

$$\cong 1.0\Omega.$$

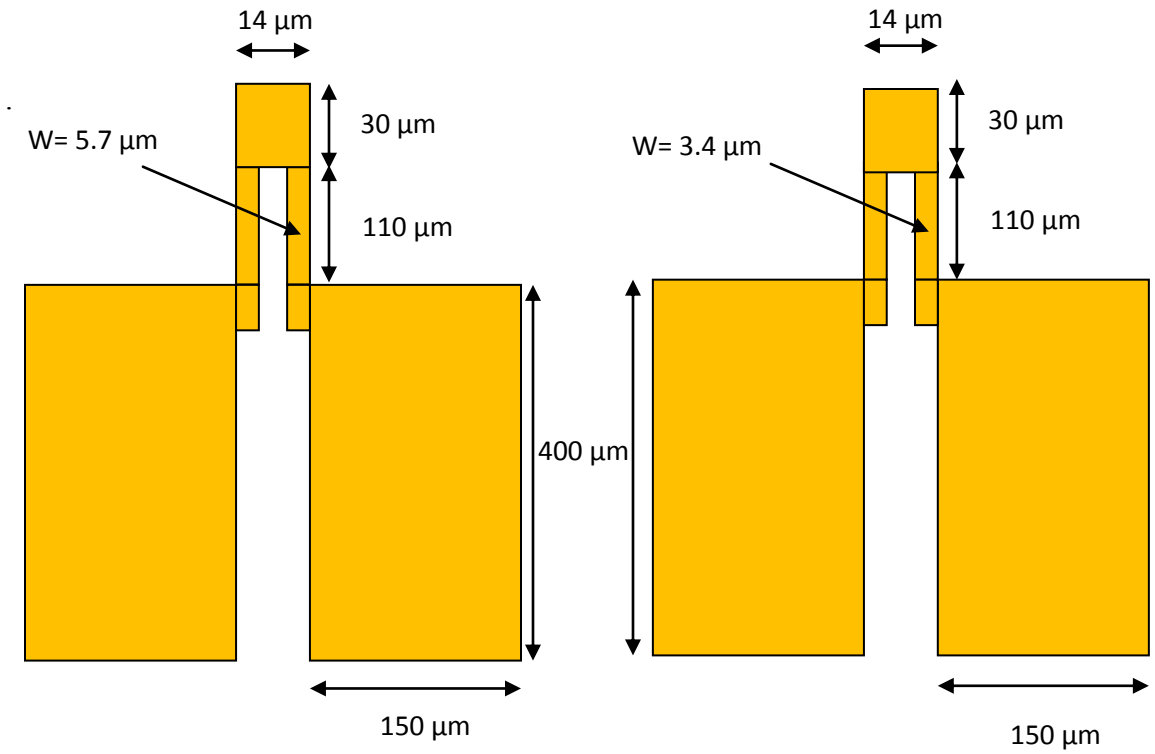

Figure 6-8: Loop 1(left electrode) and Loop 2 (right electrode) dimensions.

The theoretical dc resistance of the Loop 2 electrode in Fig. 6-8 is

$$R_{Loop2} \cong \frac{2\rho 400}{(1.1x10^{-6})(150)} + \frac{2\rho 110}{(1.1x10^{-6})(3.4)} + \frac{\rho 10}{(1.1x10^{-6})(30)}$$

$$\cong 1.6\ \Omega..$$

The series resistance of the fabricated loop electrodes corresponding to Loops 1 and 2 was measured using a vector network analyzer and a Cascade Microtech ACP40 Ground-Signal probe. Calibration was first performed using a short circuit/open circuit/ matched load calibration chip. Using a Hewlett Packard 8753E network analyzer, the series resistance of the electroplated electrodes was determined by measuring the return loss at 30 kHz to 1 MHz so that each electrode behaved as a lumped element resistor. Return loss can be expressed as

$$RL = -20log_{10}|\Gamma_L|(dB).$$

The low frequency return loss was measured at approximately 400 μm from the small portion of the loop, resulting in $RL_1 = 0.64(dB)\angle 180^{\circ}$ for Loop 1 and $RL_2 = 0.90\ (dB)\angle 180^{\circ}$ for Loop 2. The measured series resistance values for both loops were then determined as

$$R_{FabLoop1} = 50\frac{(-\Gamma_L - 1)}{(\Gamma_L - 1)} \cong 50\frac{(.929 - 1)}{(-.929 - 1)} \cong 1.8\ \Omega,$$

$$R_{FabLoop2} = 50\frac{(-\Gamma_L - 1)}{(\Gamma_L - 1)} \cong 50\frac{(.901 - 1)}{(-.901 - 1)} \cong 2.6\ \Omega.$$

The measured series resistance values for the loops are higher than the theoretical values. This could be attributed to higher resistivity of the gold produced by electrochemical

deposition. Taking an average of the ratio of the fabricated loop resistance to the theoretical loop resistance for both loops, the conductivity of the electroplated gold can be estimated as

$$R_{FabLoop1}/R_{Loop1} = 1.8\ \Omega/1.0\ \Omega \cong 1.8$$

$$R_{FabLoop2}/R_{Loop2} = 2.6\ \Omega/1.6\ \Omega \cong 1.6$$

$$\sigma_{FabAu} = \frac{2}{1.8+1.6}\sigma_{Au} = \frac{45x10^6}{1.7}\ Sm^{-1} \cong 27x10^6\ Sm^{-1}.$$

Chapter 7

Half-Wave Resonator Design and Fabrication

7.1 Introduction

A schematic of the resonator is shown in Fig. 7-1. The centre transmission line of the coupled-line resonator acts as a half-wavelength resonator and is used to detect inductance changes in the loop electrode in the microfluidic channel. The centre line consists of a short-circuit terminated section of microstrip transmission line, an SMA microstrip to coax transition, a 50 Ω transmission line inside the coaxial probe, and is terminated at the microfluidic loop electrode. The centre line is designed to act as a half-wavelength ($\lambda/2$) at 1.49 GHz. Two microstrip lines are broadside-coupled to the microstrip section of the centre line. As a magnetic bead flows over the planar loop electrode, the bead induces a load inductance change at the termination of the centre transmission line, causing a change in the resonant frequency of the resonator.

The centre line of the resonator can be thought of as a continuous 50Ω transmission line terminated by a load resistance and a variable inductance as shown in Fig. 7-2. The resistor and variable inductor model the planar electrode loop. This line behaves like a series RLC resonant circuit. Approximating the loop by a perfect short, the line has an input impedance minimum at the resonant frequency and a current maximum at the input and load end. Because the resonator is terminated by a short, it is insensitive to capacitance changes in the microfluidic channel.

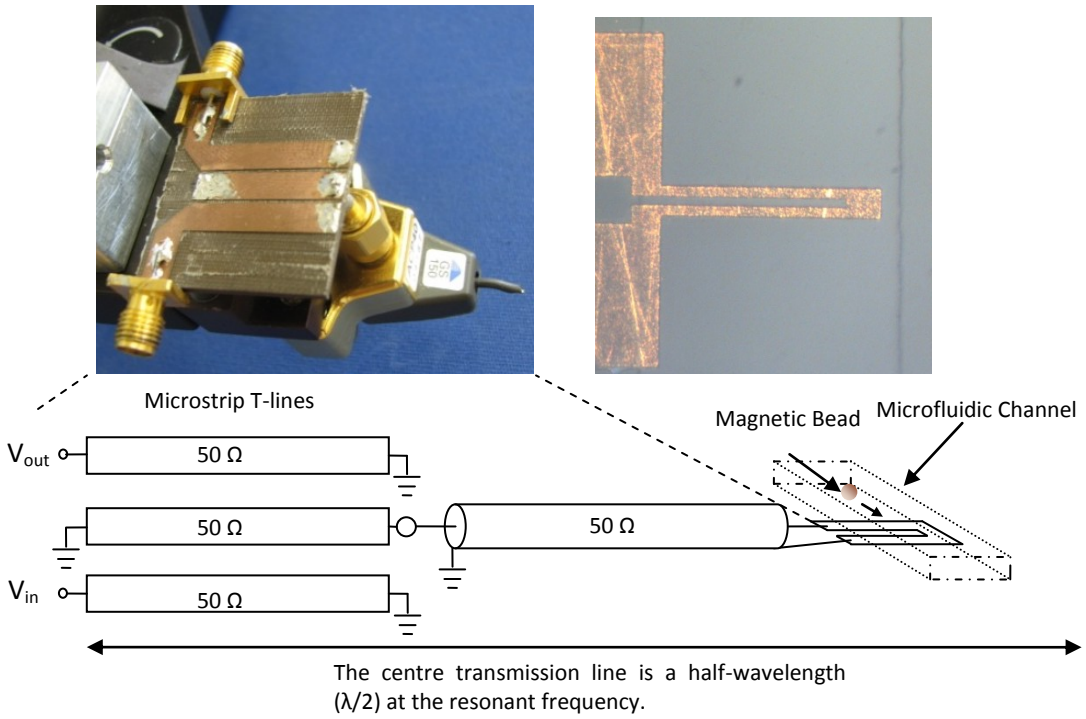

Figure 7-1: Three broadside-coupled microstrip transmission lines (left side of diagram). The centre microstrip line together with the SMA connector, GS probe, and Au electrode are a half-wavelength at the resonant frequency. A flowing magnetic bead changes the load inductance of the centre transmission line, causing a shift in resonant frequency.

The first section of this chapter will derive a theoretical equation for the change in phase with inductance to which the output signal of the sensor is proportional. The theoretical transmission line model will be related to a lumped RLC resonant circuit. Section 7.2 will describe the resonator design as well as the different parameters affecting its performance. The fabrication and response of the fabricated resonator will be covered in section 7.3 along with a comparison with the Ansoft circuit model simulation results. Finally, a value will be given for the change of phase with inductance for the fabricated resonator.

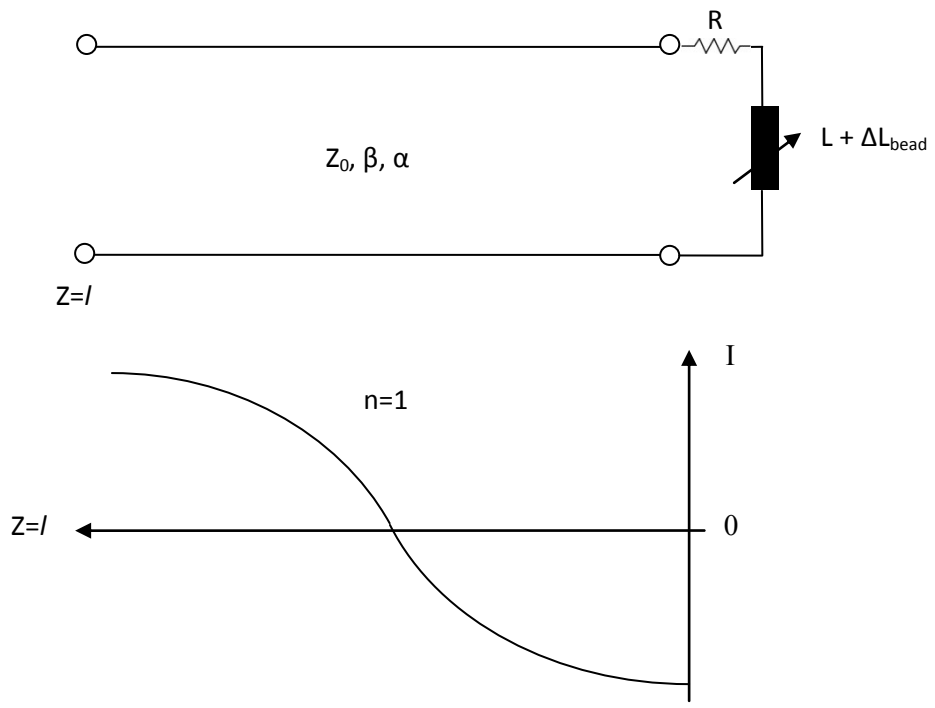

Figure 7-2: The centre resonator line can be approximated by a transmission line terminated by a small series resistance and variable inductance (top). The centre line behaves like a series RLC resonator. The current is a maximum at the input and load end if the loop is approximated as a perfect short (bottom).

7.2 Theoretical Rate of Change of Phase with Inductance

The rate of change of phase with inductance at the resonant frequency, f_0, for the coupled-line resonator, shown in Fig. 7-1, can be estimated by considering only the centre transmission line of the resonator. This model will assume no coupling loss between the centre line and the outer microstrip lines.

The change in phase with inductance for the $\lambda/2$ transmission line can be expressed as the product of partial derivatives

$$\frac{\partial \varphi}{\partial L}\Big|_{f_0} = \frac{\partial \varphi}{\partial f}\Big|_{f_0} \frac{\partial f}{\partial L}\Big|_{f_0} , \tag{7.1}$$

where $(\partial\varphi/\partial f)|f_0$ is the rate of change of phase with frequency at the resonant frequency, and $(\partial f/\partial L)|f_0$ is the rate of change of frequency with inductance at the resonant frequency. The half-wavelength $(\lambda/2)$ resonator is modeled as a $\lambda/2$ transmission line, which is terminated by a series load resistance R_L. The small load inductance of the loop will be approximated by a short. The load inductance would change the resonant frequency by a small amount if it were included. The input impedance is expressed as

$$Z_{in} = Z_0 \frac{R_L + Z_0 \tanh[(\propto + j\beta)l]}{Z_0 + R_L tanh[(\propto + j\beta)l]}. \tag{7.2}$$

The characteristic impedance is Z_o, $\propto$ is the attenuation constant, and $\beta = 2\pi/\lambda = 2\pi f/v$ is the phase contant (where λ and v are the wavelength and phase velocity, respectively). Using a hyperbolic tangent identity [Poz98b]

$$Z_{in} = Z_0 \frac{R_L + Z_0 \frac{[\tanh(\propto l) + j tan(\beta l)]}{[1 + j tan(\beta l) tanh(\propto l)]}}{Z_0 + R_L \frac{[\tanh(\propto l) + j tan(\beta l)]}{[1 + j tan(\beta l) tanh(\propto l)]}}.$$

Assuming a low-loss transmission line (i.e. $\alpha l \ll 1$), $\tanh(\propto l) \cong \propto l$. The length of the transmission line is a half-wavelength ($l = \lambda/2$) at the resonant frequencyf_0. Let a new resonant frequency $\omega = \omega_0 + \Delta\omega$, where $\Delta\omega$ is small. Furthermore, $\beta l \cong \pi + \frac{\Delta\omega\pi}{\omega_0}$ [Poz98b]. Therefore

$$\tan(\beta l) = \tan(\pi + \Delta\omega\pi/\omega_0) = \tan(\Delta\omega\pi/\omega_0) \cong \Delta\omega\pi/\omega_0 .$$

Equation (7.2) is now expressed as

$$Z_{in} = Z_0 \left[R_L + Z_0 \frac{(\propto l + j\Delta\omega\pi/\omega_0)}{(1 + j\Delta\omega\pi/\omega_0 \propto l)}\right] \left[Z_0 + R_L \frac{(\propto l + j\Delta\omega\pi/\omega_0)}{(1 + j\Delta\omega\pi/\omega_0 \propto l)}\right]^{-1} \tag{7.3}$$

Since $1 \gg j\Delta\omega\pi/\omega_0 \propto l$,

$$Z_{in} \cong Z_0 \frac{[R_L + Z_0(\propto l + j\Delta\omega\pi/\omega_0)]}{[Z_0 + R_L(\propto l + j\Delta\omega\pi/\omega_0)]} \tag{7.4}$$

$$= \frac{[R_L + Z_0(\propto l + j\Delta\omega\pi/\omega_0)]}{[1 + (R_L/Z_0)(\propto l + j\Delta\omega\pi/\omega_0)]} \quad . \tag{7.5}$$

Since $\left(\frac{R_L}{Z_0}\right)\left(\propto l + \frac{j\Delta\omega\pi}{\omega_0}\right) \ll 1$, Z_{in} simplifies to

$$Z_{in} \cong R_L + Z_0 \propto l + j(\Delta\omega\pi/\omega_0)Z_0 \; . \tag{7.6}$$

This is a series RLC resonant circuit since it is of the form [Poz98b]

$$Z_{in} = R + 2jL\Delta\omega \; ,$$

where the lumped elements are

$$R = R_L + Z_0 \propto l \tag{7.7}$$

$$L = Z_0\pi/\omega_0 \tag{7.8}$$

$$C = \frac{1}{{\omega_0}^2 L} \; . \tag{7.9}$$

The change in phase near resonance,$\Delta\varphi$, for the resonator is

$$tan\Delta\varphi = \frac{-\mathrm{Im}\{Z_{in}\}}{\mathrm{Re}\{Z_{in}\}} = \frac{-(\Delta\omega\pi/\omega_0)Z_0}{(R_L + Z_0 \propto l)} = \frac{-(\Delta f\pi/f_0)Z_0}{(R_L + Z_0 \propto l)}. \tag{7.10}$$

For small$\Delta\varphi$, as $\Delta f \to 0$ [Nik09]

$$\frac{\partial\varphi}{\partial f}\Big|_{f_0} = \frac{-\pi Z_0}{f_0(R_L + Z_0 \propto l)} \; . \tag{7.11}$$

The second partial derivative in Eq. 7.1, $\partial f/\partial L\,|_{f_0}$, is estimated by considering a low-loss transmission line of length $l = \lambda/2 = v/(2f_0)$ at the resonant frequency f_0. The phase velocity $v = 1/\sqrt{L'C'}$, and the characteristic impedance $Z_0 = \sqrt{L'/C'}$, where $L'$and C' are the inductance and capacitance per unit length of the line, respectively. We can define the new resonant frequency due to a load inductance change $\Delta L = L'\Delta l$ as

$$f = \frac{v}{2(l+\Delta l)}\,. \tag{7.12}$$

Since the phase velocity v does not change,

$$2(l + \Delta l)f = 2lf_0\,. \tag{7.13}$$

Rearranging,

$$f = f_0 \frac{l}{(l+\Delta l)}$$

$$= f_0 \frac{1}{\left(1+\frac{\Delta l}{l}\right)}$$

$$f \cong f_0\left(1 - \frac{\Delta l}{l}\right), \tag{7.14}$$

since Δl is small. We can now define the resonant frequency in terms of the load inductance as

$$f \cong f_0\left(1 - \frac{\Delta L}{L'l}\right)$$

$$f \cong f_0\left(1 - \frac{\Delta L}{L'[v/(2f_0)]}\right)$$

$$f \cong f_0 - \frac{2{f_0}^2\Delta L}{Z_0}\,. \tag{7.15}$$

The change in resonant frequency is expressed as

$$\Delta f = f - f_0 \cong -\frac{2{f_0}^2 \Delta L}{Z_0}. \tag{7.16}$$

The change in resonant frequency over the change in load inductance is

$$\Delta f/\Delta L = -\frac{2{f_0}^2}{Z_0},$$

and as ΔL goes to zero, the rate of change of frequency with load inductance becomes

$$\partial f/\partial L\,|_{f_0} \cong -\frac{2{f_0}^2}{Z_0}. \tag{7.17}$$

Finally, using Eq. 7-11 and Eq. 7-17, the rate of change of phase with inductance can now be expressed as

$$\frac{\partial \varphi}{\partial L}|_{f_0} = \frac{\partial \varphi}{\partial f}|_{f_0} \frac{\partial f}{\partial L}|_{f_0},$$

$$\frac{\partial \varphi}{\partial L}|_{f_0} = \frac{2\pi f_0}{(R_L + Z_0 \propto l)}\ . \tag{7.18}$$

The loaded rate of change of phase with inductance of the coupled-line resonator will be lower than shown in Eq. 7.18 due to the coupling between the centre transmission line and the input and output microstrip lines. This will increase the effective loss, which would be incorporated as a loss factor in the denominator of Eq. (7-18).

7.3 Half-Wave Resonator Design

This section presents the equivalent circuit model of the resonator sensor and its solution using the Ansoft circuit simulator. Two microstrip transmission lines (one for the input, the other for the output) are broadside-coupled to the half-wave transmission line, depicted schematically in Fig. 7-3. The broadside-coupled design was based on a previous quarter-wave resonator design [Tran01] used to detect capacitance changes. The electrode inside the microfluidic channel, which terminates the $\lambda/2$ transmission line, is a planar gold loop (described in Chapter 6). The loop resistance was minimized to achieve the highest possible quality factor for the resonator. It was observed that using a custom-made probe (two brass wires) at the end of the centre transmission line to make contact with the loop electrode resulted in high contact resistance that made the quality factor very low. Instead, a commercial Ground-Signal (GS) probe (Cascade Microtech, ACP40, 150 pitch) was used, which enabled precise movement control and very low contact resistance with the gold electrode loop. Furthermore it enabled the testing of multiple loops without the need to solder each connection. The centre line was designed to be 50 Ω to match to the 50 Ω SMA connector and commercial 50 Ω GS probe.

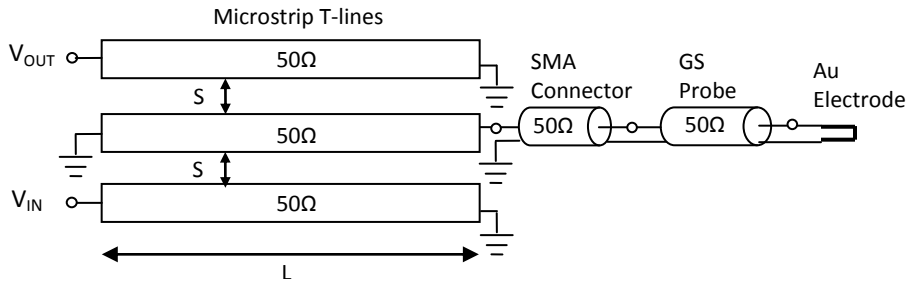

Figure 7-3: Three broadside-coupled microstrip transmission lines (left). Centre microstrip line together with the SMA connector, GS probe, and Au electrode are a half-wavelength at the resonant frequency. Spacing, S, determines the coupling between the centre line and the input and output lines, and affects the insertion loss. Length, L, affects the resonant frequency and, to a lesser extent, the insertion loss.

The physical length of the SMA connector is 12 mm. The connector is made of a piece of semi-rigid coaxial cable cut at one end and soldered to the middle copper trace of the microstrip board. The electrical length of a 23 cm long piece of semi-rigid coaxial cable was measured using a network analyzer (NA). The electrical length of the cable was 180° at 405 MHz. For a low-loss line, the phase constant $\beta \cong \omega\sqrt{\mu\epsilon_r\epsilon_0}$. Therefore the relative dielectric constant of the cable is

$$\beta l = \pi \cong \omega\sqrt{\mu\epsilon'}l,$$

$$\epsilon_r \cong \left(\frac{\pi}{\omega l}\right)^2 \mu_0\epsilon_0 = \left(\frac{\pi}{\omega l}\right)^2 \mu_0\epsilon_0 \cong 2.59.$$

The connector was modeled in Ansoft Designer as a lossless coaxial cable with ϵ_r=2.59. The conductor losses of the coplanar probe and SMA connector were ignored since they would be much less than the series resistance of the loop electrode. The reflection

coefficient of the shorted GS probe was measured using a VNA. From the phase information,

$$2\beta l = \pi \cong 2\omega\sqrt{\mu\epsilon'}l$$

$$\sqrt{\epsilon_r}l \cong \frac{1/2}{2f\sqrt{\mu_0\epsilon_0}} \cong 4.92cm/\sqrt{\epsilon_r}.$$

The GS probe was therefore modeled as a 4.92 cm long transmission line with a dielectric constant $\epsilon_r = 1$ (a dielectric loss coefficient of 0.16 dB/m was chosen).

The loop electrode was modeled by a section of 50 Ω transmission line with $\epsilon_r = 1$ (the true $\epsilon_{reff}$of the loop electrode feed line is accounted for in the effective length), terminated with a load resistance (a load inductance can be included to simulate the resonator response to inductance changes, ΔL). The resistance of the gold electrodes Loop 1 and Loop 2 was measured (see section 6.5) to be 1.8 Ω and 2.6 Ω, respectively. The electrical length was determined by measuring the return loss using the VNA. The electrical length at 1.5 GHz for Loop 1 and Loop 2 were both approximately 1.7°. Therefore

$$\beta l = \frac{1.7}{180}\pi \cong (2\pi)(1.5x10^9)\sqrt{\mu_0\epsilon_0}l$$

$$l = 1.04mm \cong 1mm.$$

The return loss for Loop 1 was -.63 dB at 1.5 GHz, corresponding to load resistances of 1.8 Ω. The return loss for Loop 2 was -.89 dB at 1.5 GHz, corresponding to load resistances of 2.6 Ω.

The Ansoft model for the resonator is shown in Fig. 7.4. The microstrip board is modeled as a grounded 1.57 mm thick Cu-clad (17 μm Cu thickness) board with $\epsilon_r = 2.54$, $tan\delta = .0009$, with 4.4mm (50 Ω) line widths.

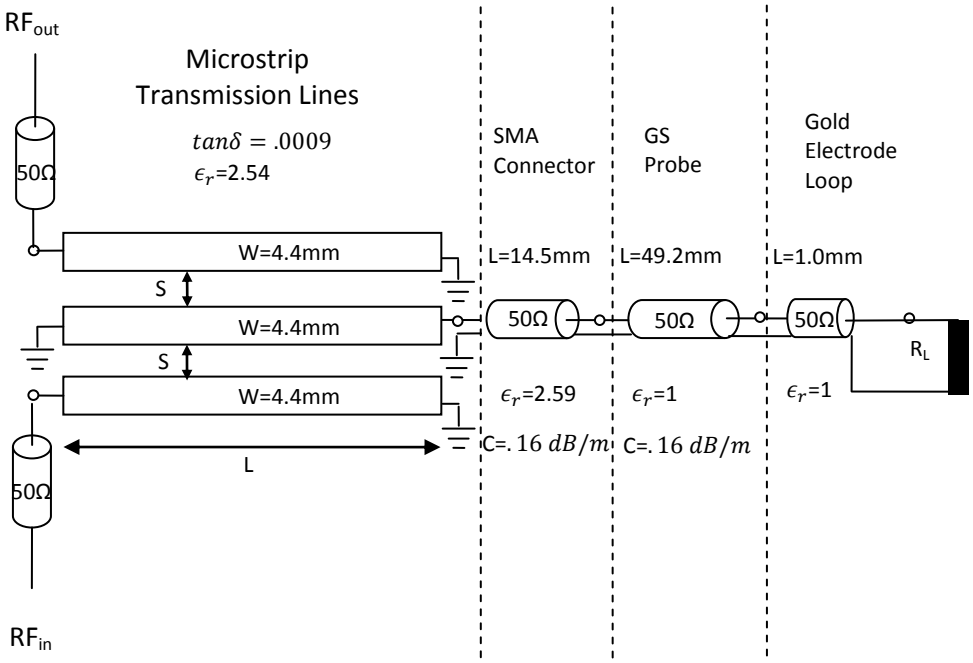

Figure 7-4: Half-wave coupled-line resonator model used for Ansoft Designer simulation.

With these components added to the Ansoft model, the resonator design involves choosing the spacing (S in Fig. 7-4) between the broadside-coupled microstrip lines and choosing an overall length (L in Fig. 7-4). The simulated load resistance was 2.6 Ω (Loop 2 resistance). Table 7-1 summarizes the simulation results for different values of S and L. Figure 7-5 shows that the resonant frequency increases linearly as L decreases. As shown in Fig. 7-6, as S increases, the insertion loss also increases. However, as shown in Fig. 7-7, the quality factor increases as S increases. Because the microwave components used in the interferometer are optimized to work at frequencies above 1 GHz (rated from 1 GHz),

the maximum length that was simulated was 35 mm (corresponding to $f_0 \cong$1.2 GHz). The sensor output

$$S \cong G|V_{REF}||V_{RES}|\left(\frac{\partial\varphi}{\partial f}\right)|_{f_o}\left(\frac{\partial f}{\partial L}\right)|_{f_o}(\Delta L)$$

is proportional to the quality factor of the resonator ($\partial\varphi/\partial f$) as well as the magnitude of the voltage at the output of the resonator. This voltage magnitude is affected by the insertion loss of the resonator. Therefore, to compare the different designs in Table 7-1, the product of Q and V_2/V_1 is shown as an approximate measure, and is shown graphically in Fig. 7-8.

Although a number of different designs could have been used, the fabricated resonator was designed to have S = 0.5 mm and L = 20 mm. The actual fabricated dimensions were S = 0.6 mm and L= 19.5 mm due to imperfect milling of the microstrip traces. The fabricated resonator had a quality factor, Q = 13.0, and an insertion loss, IL = 6.8 dB, when terminated by a 2.6 Ω series resistance loop (see section 7.4). A resonant frequency of 1.48 GHz represents a good design trade-off because the noise performance of the microwave circuitry used in the sensor worsened at frequencies closer to 1 GHz, while the insertion loss increases significantly at higher frequencies.

S=2mm					
L (mm)	f_o(GHz)	$20\log_{10}\|S_{21}\|$(dB)	$\|V_2/V_1\|$	Q	$\|V_2/V_1\|$xQ
35	1.21	-13.0	.22	17.9	3.9
25	1.37	-14.1	.20	17.8	3.6
20	1.46	-15.4	.17	18.7	3.2
15	1.57	-17.7	.13	19.6	2.5
10	1.70	-22.0	.08	20.2	1.6
S=1mm					
L (mm)	f_o(GHz)	$20\log_{10}\|S_{21}\|$(dB)	$\|V_2/V_1\|$	Q	$\|V_2/V_1\|$xQ
35	1.22	-7.2	.44	14.2	6.2
25	1.38	-8.2	.39	14.5	5.7
20	1.47	-9.3	.34	15.3	5.2
15	1.58	-11.5	.27	16.0	4.3
10	1.71	-15.4	.08	18.2	3.1
S=0.75mm					
L (mm)	f_o(GHz)	$20\log_{10}\|S_{21}\|$(dB)	$\|V_2/V_1\|$	Q	$\|V_2/V_1\|$xQ
35	1.22	-5.8	.51	12.6	6.4
25	1.38	-6.7	.46	12.8	5.9
20	1.48	-7.9	.40	13.3	5.3
15	1.58	-9.8	.32	14.5	4.6
10	1.71	-13.5	.21	16.6	3.5
S=0.5mm					
L (mm)	f_o(GHz)	$20\log_{10}\|S_{21}\|$(dB)	$\|V_2/V_1\|$	Q	$\|V_2/V_1\|$xQ
35	1.23	-4.3	.61	9.8	6.0
25	1.39	-5.2	.55	10.9	6.0
20	1.48	-6.2	.49	11.6	5.7
15	1.59	-8.0	.40	13.2	5.3
10	1.72	-11.5	.27	15.6	4.2

Table 7-1: Ansoft Designer simulation results of the coupled-line resonator, for different spacing distances (S in Fig. 7-1) and different lengths (L in Fig. 7-1).

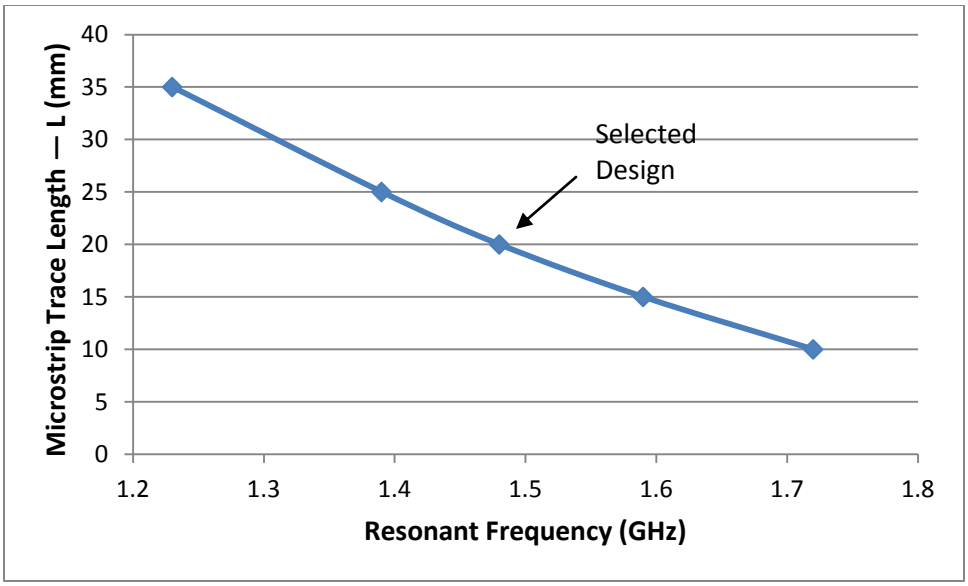

Figure 7-5: Resonator simulation showing resonant frequency as a function of microstrip trace length L.

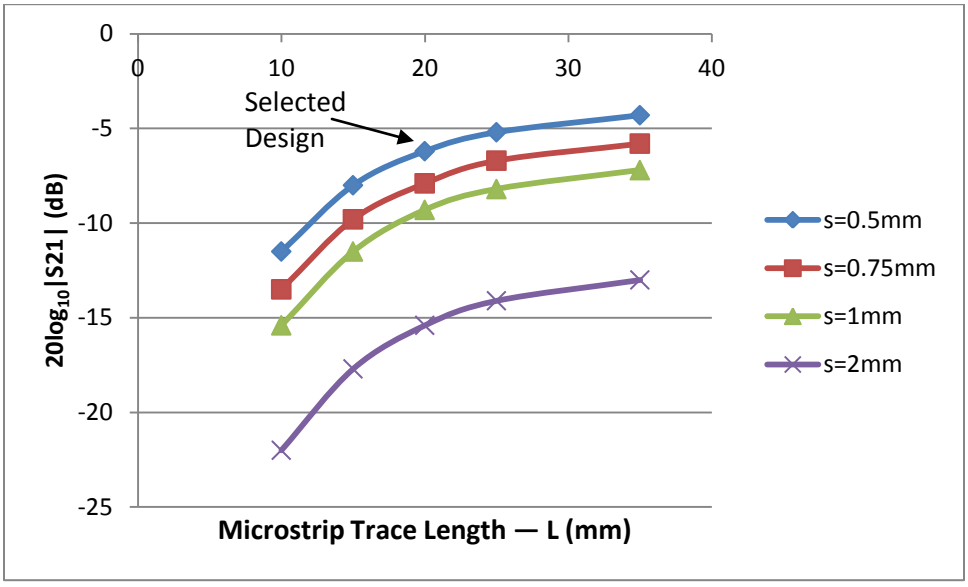

Figure 7-6: Resonator simulation showing effect of L on $20\log_{10}|S21|$ for various values of trace spacing, s.

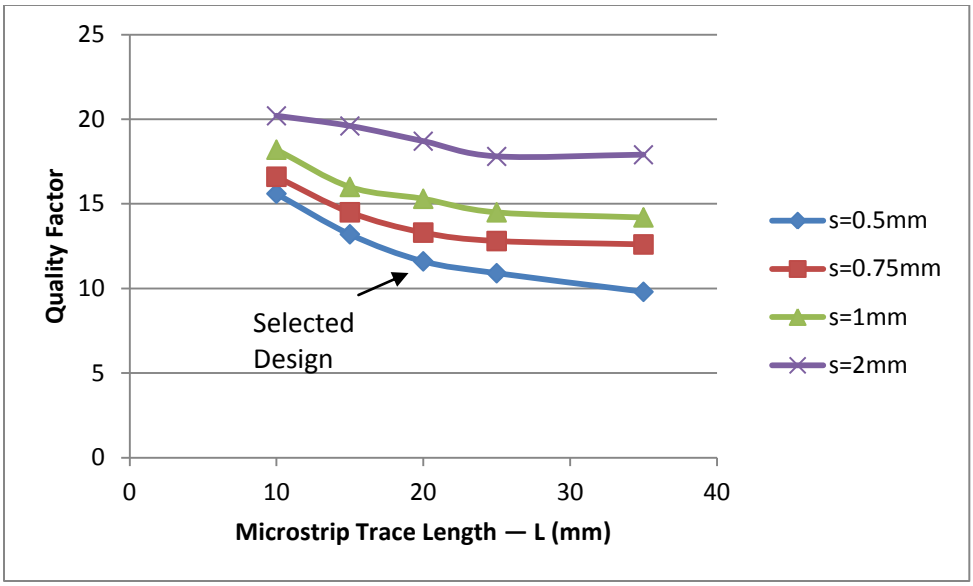

Figure 7-7: Resonator simulation showing effect of L on resonator quality factor.

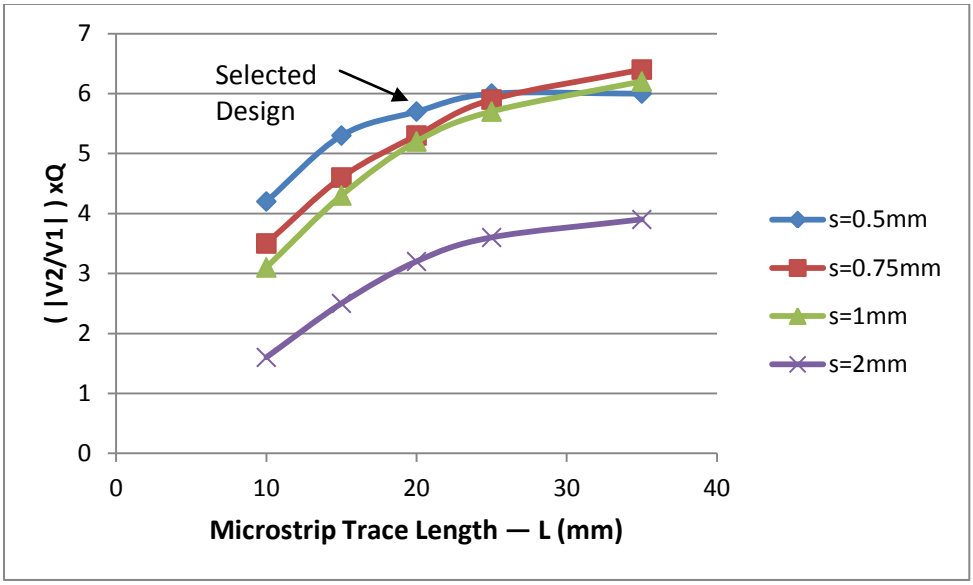

Figure 7-8: Resonator simulation comparing various design dimensions by the product |V2/V1| x Q.

7.4 Half-wave Resonator Fabrication and Measurement

After simulating the resonator in Ansoft Designer, the broadside-coupled microstrip lines were fabricated on a grounded Cu-Clad TLX-9 (Taconic) Laminate board. The board thickness was 1.57 mm, with a relative dielectric constant of $\epsilon_r = 2.54$, and a loss tangent of $tan\delta = .0009$ at 2GHz. The copper thickness was 17 mm, and the traces were 4.4 mm wide (50 Ω), with 0.6 mm spacing (designed for 0.5 mm), and a length of 19.5 mm. The traces were milled using a T-Tech Quick Circuit/HF milling machine. The fabricated resonator is shown in Fig. 7.9.

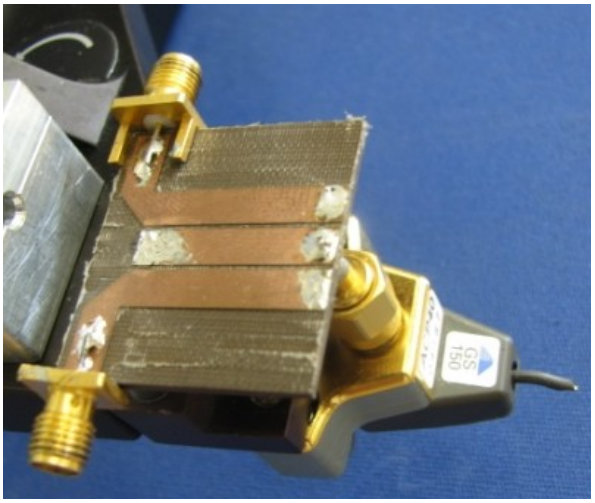

Figure 7-9: Fabricated λ/2 resonator. Three broadside-coupled microstrip transmission lines milled out on a 1/16" Cu-Clad TLX-9 Taconic Laminate board. Centre microstrip line together with the SMA connector, GS probe, and Au electrode (not shown) are a half-wavelength at the resonant frequency.

Figure 7.10 shows a comparison of the negative insertion loss response between the measured resonator (terminated by Loop 1 and Loop 2) and the simulated Ansoft model (using 2 Ω and 3 Ω for the load resistance to model Loop 1 and Loop 2, respectively).

The insertion loss responses are in good agreement; however, the measured response for each loop has a greater insertion loss and a slightly lower Q at the resonant frequency than the simulation. The simulation did not taking into account radiation losses from the microstrip lines. Moreover, the resonant frequencies and quality factors were also sensitive to the probe position on the electrode. Table 7-2 summarizes the resonant frequencies, insertion loss at resonant frequency, and quality factors for the measured and simulated resonators terminated by Loop 1 and Loop 2.

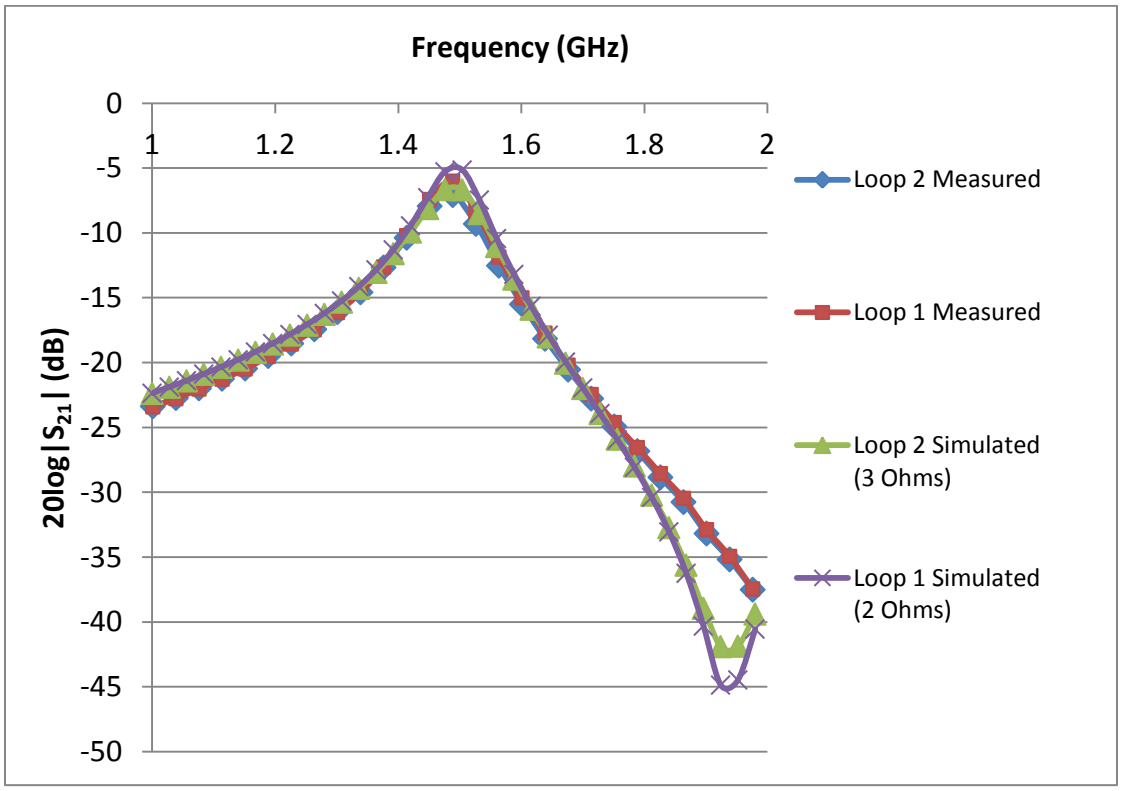

Figure 7-10: Power transmission response of measured resonator (terminated by Loop 1 and Loop 2) and simulated Ansoft model (R_L=2 Ω, and R_L =3 Ω).

	f_0 (GHz)	Insertion Loss (dB)	Quality Factor
Loop 1 measured	1.494	5.9	14.4
Loop 2 measured	1.495	6.8	13.0
Loop 1 simulated (2 Ω)	1.492	4.9	15.7
Loop 2 simulated (3 Ω)	1.492	6.4	13.1

Table 7-2: Comparison of measured resonator response (terminated by Loop 1 and Loop 2) and simulated Ansoft model (R_L=2 Ω, and R_L =3 Ω).

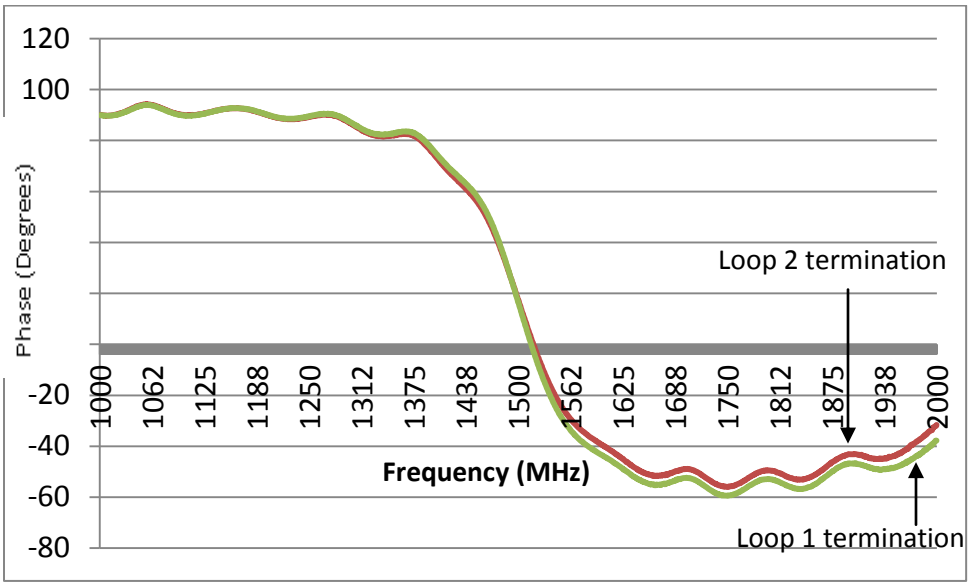

Figure 7-11: Measured phase response of the resonator terminated by Loop 1 (green) and Loop 2 (red). The path length phase dependence has been subtracted from the phase response.

The measured phase response, with the linear phase dependence of the test cable path lengths subtracted, for the resonator terminated by Loop 1 and Loop 2, is shown in Fig. 7-11. The measured rate of change of phase with frequency for the resonator terminated by Loop 1 was

$$\frac{\partial \varphi}{\partial f}|_{f_0} \cong -19.5x10^{-9}\ \text{rad/Hz},$$

and the measured rate of change of phase with frequency for the resonator terminated by Loop 2 was

$$\frac{\partial \varphi}{\partial f}|_{f_0} \cong -17.0x10^{-9} \text{ rad/Hz.}$$

These values are in very close agreement with the simulated values. For a 1 fH change in inductance, the simulated change in resonant frequency was -80 Hz. Therefore

$$\frac{\partial f}{\partial L}|_{f_0} \cong -80 \text{ Hz/fH.}$$

The simulated rates of change of phase with inductance for the resonator terminated by Loop 1 and Loop 2 are

$$\frac{\partial \varphi}{\partial L}|_{f_0} = \frac{\partial \varphi}{\partial f}|_{f_0} \frac{\partial f}{\partial L}|_{f_0},$$

$$\frac{\partial \varphi}{\partial L}|_{f_0(Loop\ 1)} \cong 1.6\ x\ 10^{-6} \text{ rad/fH,}$$

and

$$\frac{\partial \varphi}{\partial L}|_{f_0(Loop\ 2)} \cong 1.4\ x\ 10^{-6} \text{ rad/fH.}$$

Chapter 8

Single 4.5 µm Dynabead® Measurements and Results

This chapter focuses on the measured signals caused by single 4.5 µm magnetic Dynabeads® flowing over the microfluidic loop electrode sensor. Section 8.1 will describe the sample preparation, interferometer settings and measurement results using Loop 1. The sample preparation, interferometer settings and measurement results using Loop 2 will be presented in Section 8.2. The chapter will be concluded with an estimation of the real part of the magnetic permeability and susceptibility of a 4.5µm Dynabead® based on power level measurements and the results from section 8.2. Finally, the sensor sensitivity and resolution is estimated at the end of section 8.3.

8.1 Single 4.5 µm Dynabead® Detection Using Loop 1

Single 4.5 µm Dynabead® detection was achieved with both loops. Loop 1, which was approximately 5.7 µm wide with 2.3 µm spacing, was first used to detect single 4.5 µm Dynabeads® that were mixed with 4.5 µm polystyrene spheres (PSSs) in a DI water solution. The PSSs were included in the solution to experimentally verify that the signal obtained from a bead was due only to its magnetic properties. The fluid-flow in the channel was not consistent, and as a result the concentration of the two types of bead in the solution varied throughout the experiment; It was observed that the magnetic beads seemed to be getting clogged in the channel (possibly due to their epoxy coating) and were not always flowing past the electrode in as great a number as the PSSs.

Figure 8-10 shows a schematic of the inductance sensor system. For this experiment, the input power from the signal generator was set to 8 dBm. The resonant frequency of the resonator was 1.493 GHz, which was determined by using a peak detector (shown in Fig. 8-10). The phase difference between the two interferometer paths (see Fig. 8-10) was set to 90° in order to zero the output signal, and to ensure that the sensor output was proportional to the change in phase caused by a magnetic bead. The phase difference between the two paths was later confirmed to be -90°, which added a 180° phase reversal to the output signal. A negative sign was added to the data to correct for this phase reversal. The LIA bandwidth was set to 42 Hz by choosing a 3 ms time constant with 12 dB roll-off. The LIA sensitivity was set to 100 µV/V, the phase reference was set to 0°, and the square-wave modulation frequency was set to 91.5 kHz. The flow rate for this experiment was only maintained for a short period of time before the channel leaked.

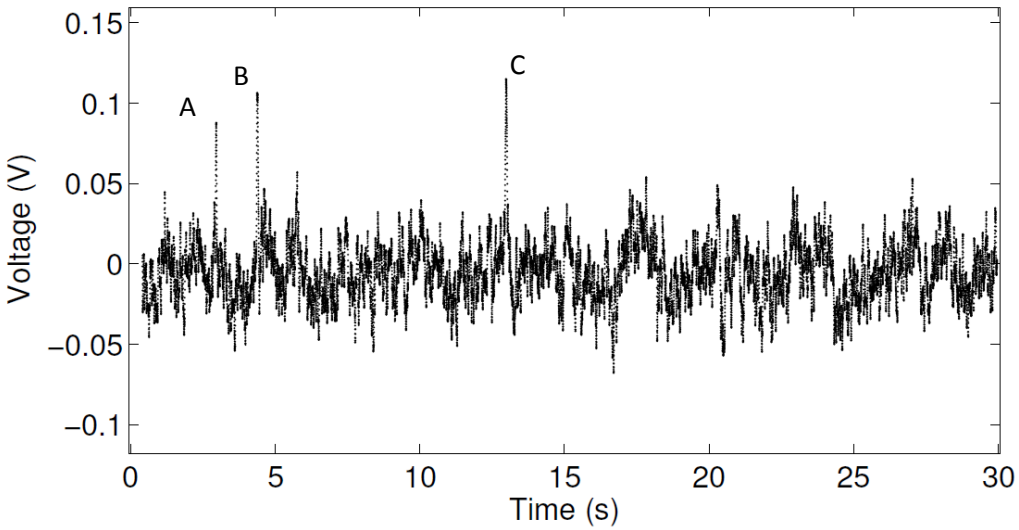

Figure 8-1: Signals due to 3 single 4.5 µm Dynabeads®. Average bead flow rate is 280 µm/s. The RMS noise is 20 mV for a 5 sec window between 6 s and 11 s.

Figure 8-1 shows the signals obtained from 3 individual Dynabead® crossing events, while the video snapshots of these events are shown in Fig.8-2. The RMS noise was 20 mV for a 5 sec window. The peak signal of the first crossing event was 85 mV, while the next two beads produced 105 mV and 110 mV signals. The signal-to-noise ratios (SNRs) for the three signals are 11.5 dB, 14.8 dB, and 14.8 dB, respectively. The average bead flow rate was 280 μm/s. The first bead flowed close the end of the loop, which could explain the smaller magnitude. Alternatively, because the high magnetic field gradient above the loop causes the signal to be very sensitive to bead elevation, the first bead could have been at a higher elevation inside the channel. PSSs flowed past the electrode region within the 30 second window shown in Fig. 8-1 but did not produce any signals. All other experiments confirmed that PSSs do not produce signals as they passed over the loop. Figure 8-3 shows a few close-up video snapshots, where a clear difference is seen between magnetic beads and polystyrene spheres as they pass over the electrode. The magnetic beads are seen as semi-transparent spheres with a red tinge while the PSSs are black and opaque as they pass over the electrode. The two bead types were therefore visually distinguishable during the experiment.

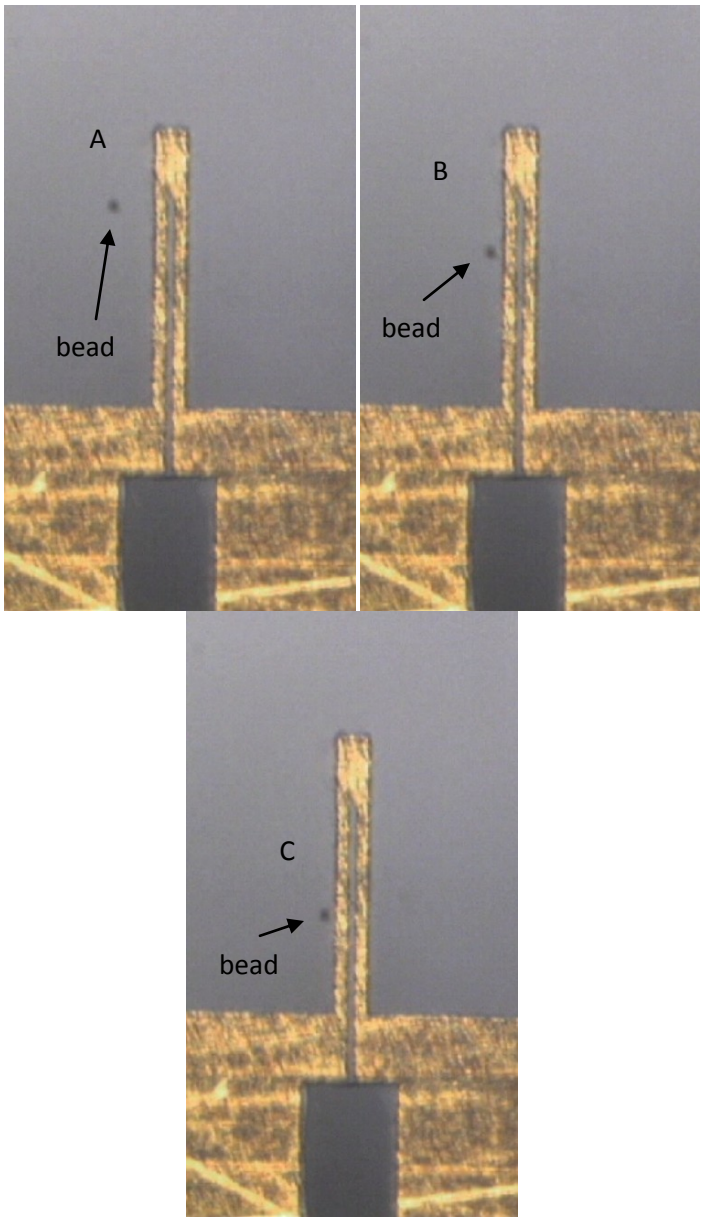

Figure 8-2: Video snapshot of magnetic bead crossing events corresponding to beads A, B, and C from Fig. 8-1.

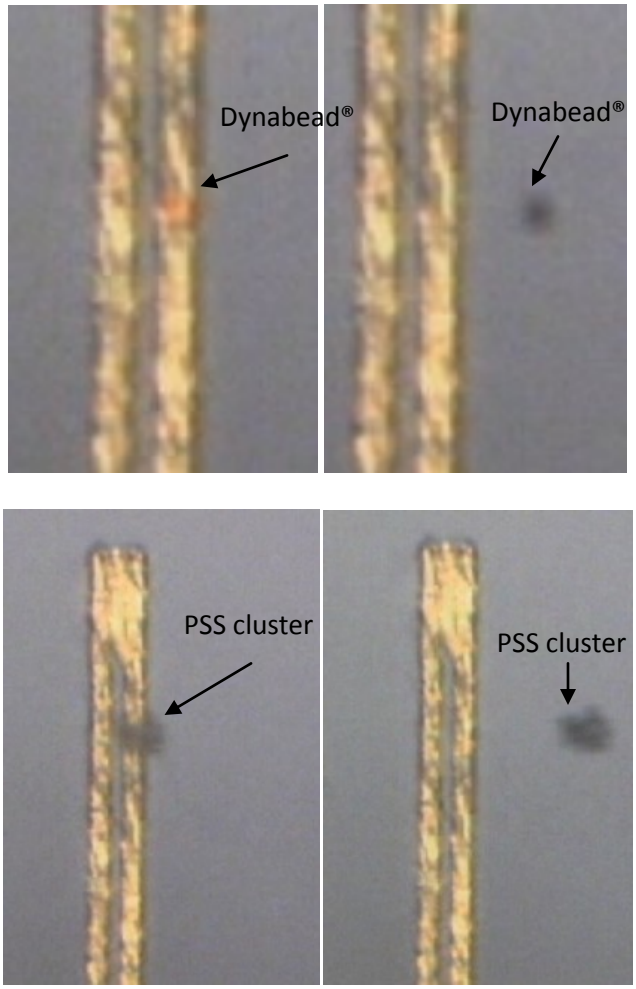

Figure 8-3: Close-up of video snapshots showing the different colour and transparency of a magnetic Dynabead® (top two snapshots) compared to an aggregate of PSSs (two bottom snapshots). All PSSs look dark and opaque as they pass over the electrode loop, while the Dynabeads® look semi-transparent.

Figure 8-4 shows a 155 mV signal due to 2 closely-spaced Dynabeads® followed by a 110 mV signal due to a single Dynabead®. The signal suggests that scaling occurs with multiple beads, but because the beads were not simultaneously at the inner edges of the electrode, the first signal is not expected to be twice the amplitude of the second signal. Furthermore, the bead elevations are also unknown. The video snapshots of the bead crossing events are shown in Fig. 8-5. A more

detailed plot of the signal due to a single magnetic bead (corresponding to signal C in Fig. 8-1) is shown in Fig. 8-6 (top). The shape was predicted to follow the variation of the square of the magnetizing field above the loop as was simulated using Comsol in chapter 5. The simulated field is shown in Fig. 8-6 (bottom) for an elevation of 2.5 μm above the top of Loop 1 (see Fig. 5-5 for a plot of simulated profiles of the square of the magnetizing field for various bead elevations above Loop 1).

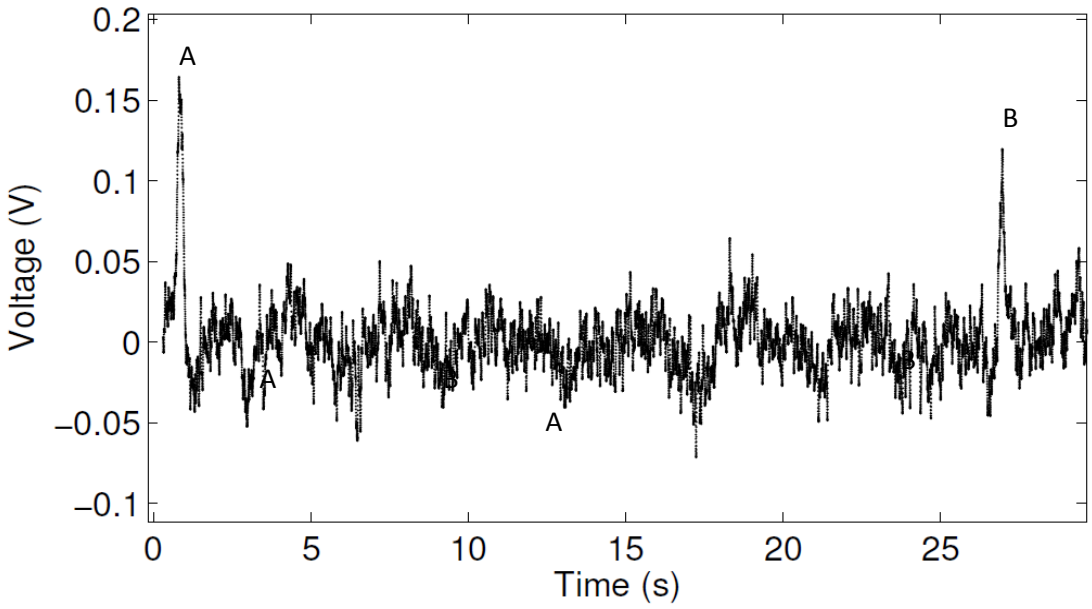

Figure 8-4: 155 mV signal due to 2 closely-spaced single 4.5 µm Dynabeads® followed by a 110 mV single due to a single 4.5 µm Dynabead®. Average bead flow rate is 80 µm/s. The RMS noise is 20 mV for a 5 sec window between 5 s and 10 s.

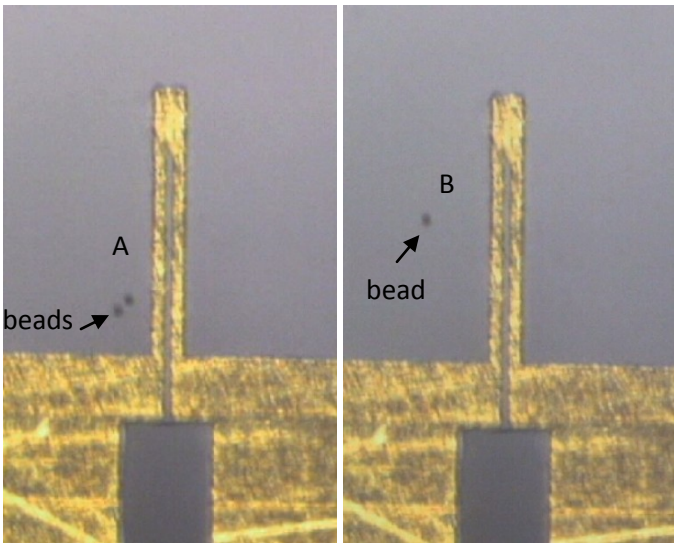

Figure 8-5: Video snapshots of bead crossing events corresponding to A and B in Fig. 8-4.

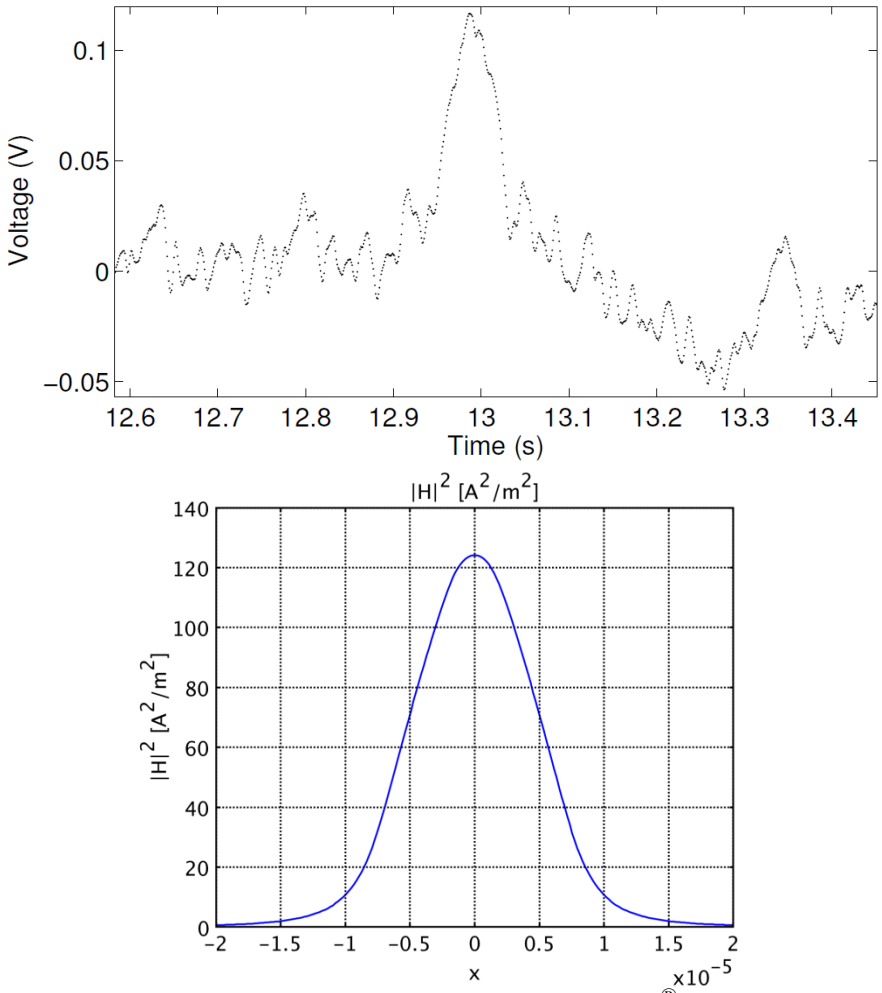

Figure 8-6: Signal due to a single 4.5 µm Dynabead® (top). Square of the magnetizing field above Loop 1 for an elevation of 2.5 µm (bottom), as simulated using Comsol (see Fig. 5-5). The shape of the signal follows the square of the magnetizing field above the loop.

8.2 Single 4.5 µm Dynabead® Detection Using Loop 2

The loop electrode that provided the highest signal-to-noise ratio for detecting single 4.5 µm Dynabeads® was Loop 2 (3.4 µm width and 2.8 µm spacing). To prevent fluid leakage caused by the breaking of the reversible seal between the PDMS and the glass slide, two clamps were used to apply downward pressure on the polyethylene tubing

to ensure a proper seal around the port openings. This only prevented leaking from occurring for a certain period of time, however. A solution of 3 drops (using 1 mL syringe) of 4.5 μm Dynabeads® and 2 drops (using 1 cc syringe) of 6 μm PSSs inside 10 mL of DI water was injected into the channel using a syringe. The 6 μm PSSs were used in this experiment to more easily distinguish the two bead types when examining the microscope images.

Referring to Fig. 8-10, the input power for this experiment was 8 dBm, and the resonant frequency of the resonator was measured at 1.485 GHz, using a peak detector. The phase difference between the two interferometer paths was set to 90° to zero the output signal. Similar to the experiments in section 8.1, the phase difference was later confirmed to have been -90°, which added a 180° phase reversal to the output signal in the following experiments. A negative sign was later added to the data. The LIA bandwidth was set to 42 Hz by choosing a 3 ms time constant with 12 dB roll-off. The LIA sensitivity was set to 200 μV/V, the phase reference was set to 0°, and the square-wave modulation frequency was set to 91.5 kHz.

The measured signals showed greater variability in their magnitude than was seen for Loop 1. The increased variability was expected, given the greater magnetic field gradient above Loop 2, and thus greater sensitivity to bead elevation. The signals shown in Fig. 8-7 are due to single Dynabeads®. The RMS noise is approximately 10 mV, calculated using a 2 s window. The signal peaks are 166 mV and 207 mV, with approximately 80 μm/s bead flow rates. The corresponding video snapshots in Fig. 8-7 show the positions of the beads relative to the end of the electrode loop. The 207 mV

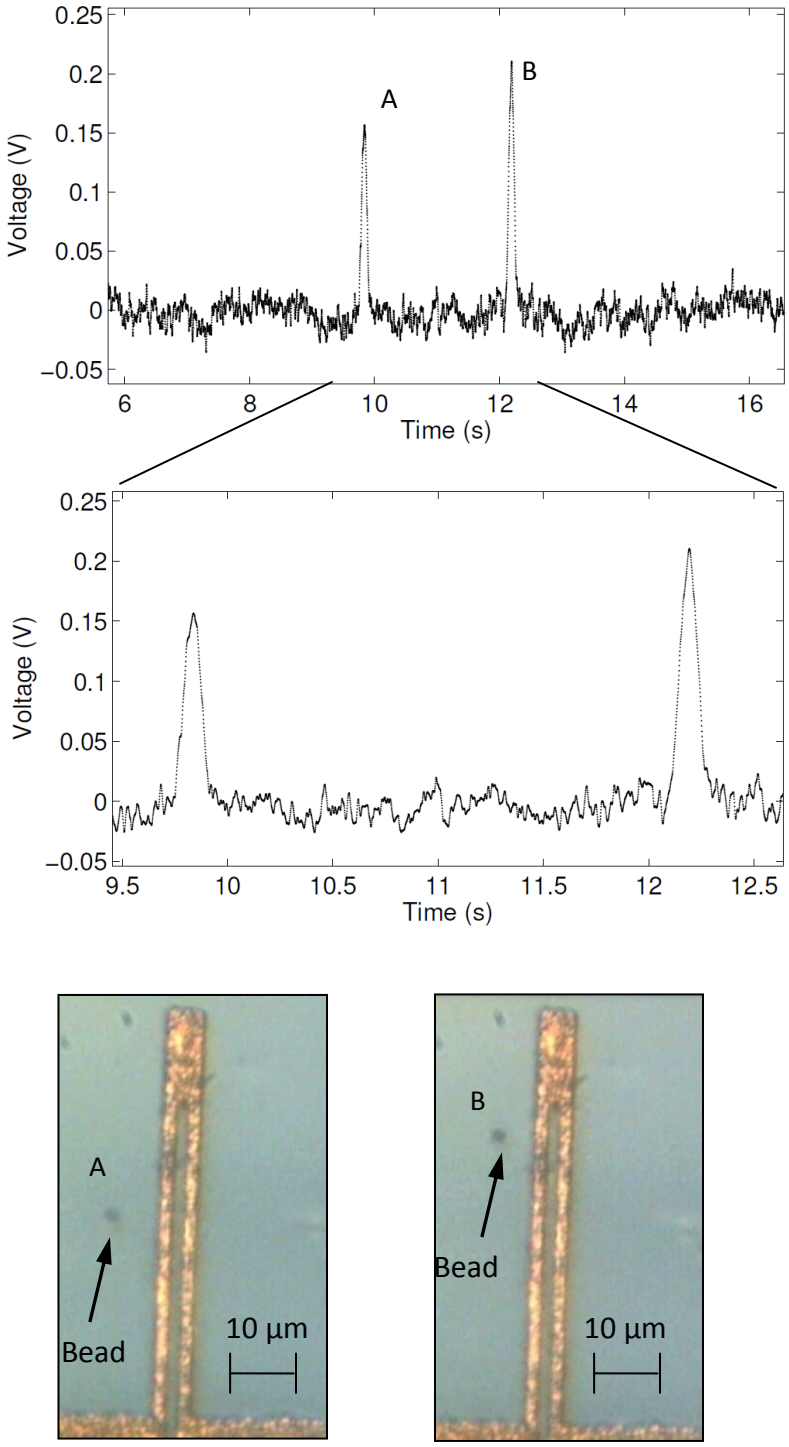

Figure 8-7: Signals and video snapshot of two single 4.5 µm Dynabeads®. The 207 mV signal from the bead labeled B was the strongest signal obtained in this experiment, possibly due to a higher magnetization or due to the low elevation at which it was flowing (100 mV signals were also recorded, suggesting that some beads were flowing at higher elevations).

signal was the strongest signal obtained for a single magnetic bead using Loop 2, suggesting that the bead was flowing right above the electrode. Alternatively, that particular bead could have had greater effective magnetization. The SNRs of the two signals, A and B, in Fig. 8-7 are 24.4 dB and 26.3 dB, respectively. Figure 8-8 shows images of a PSS flowing near the bottom of the channel. PSSs did not produce any signals, as was the case in the Loop 1 experiments and all other experiments.

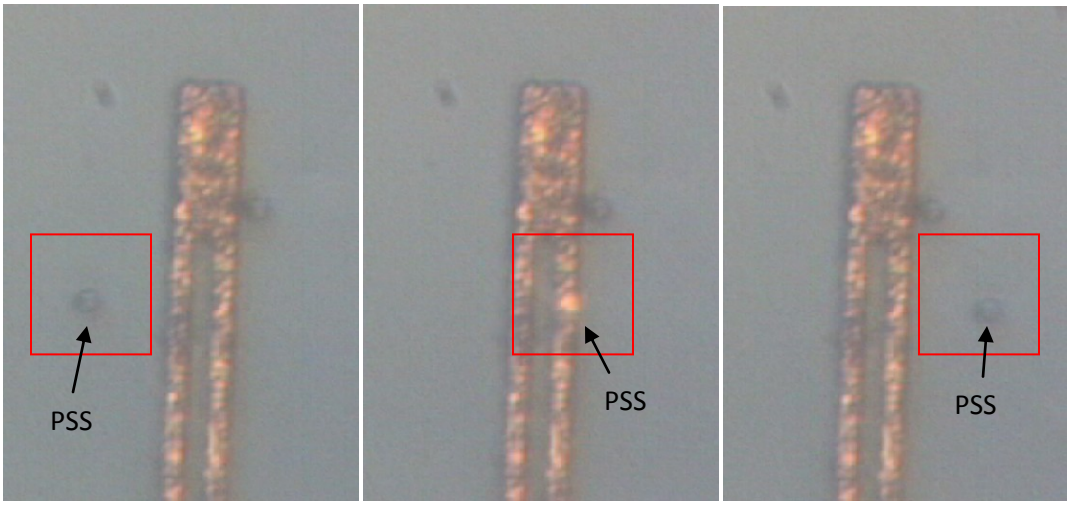

Figure 8-8: Video snapshots of a single PSS flowing near the electrode. PSSs did not produce any signals.

Figure 8-9 shows the signal caused by a single Dynabead® attached to a 6 µm PSS. The signal peak is 154 mV with a bead flow rate of approximately 80 µm/s. The RMS noise for a 4 s window between 25 and 29 s was approximately 10 mV, giving an SNR of 23.8 dB for the Dynabead® attached to the PSS. This signal demonstrates the ability of detecting a marker when it is attached to an analyte particle, in this case, simulated by the PSS.

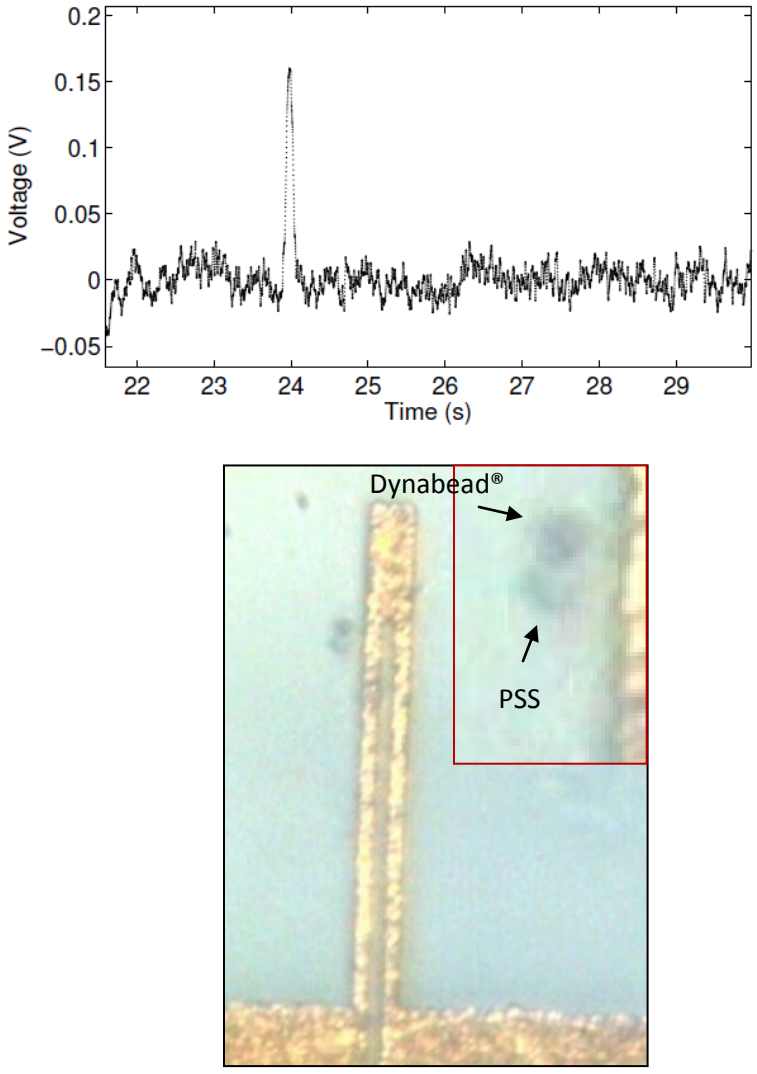

Figure 8-9: Signal and video snapshot of a 4.5 µm Dynabead® attached to a 6 µm PSS. The signal peak was 154 mV with a flow rate of approximately 80 µm/s. The RMS noise was approximately 10 mV (for a 4 second window between 25 s and 29 s).

8.3 Estimation of Sensor Sensitivity, Resolution, and the Real Part of the Magnetic Permeability of a Single Bead

With the resonator terminated by Loop 2, the power levels at various locations in the interferometer signal paths were measured using an HP 438A power meter. The power meter was first warmed up and calibrated. The input power to the interferometer was set to 8 dBm at a frequency of 1.4885 GHz. The power levels are shown in Fig. 8-10. The conversion factor, g_c, of the mixer was calculated by first measuring the rms power levels P_{REF} and P_{RES}. The phase difference between the two paths was set to zero to remove any output signal phase dependence. The square wave signal amplitude of the output of the mixer was measured using an oscilloscope with a 50 Ω input impedance. Based on Eq. 3-3, with φ = 90°, the IF port voltage can then be expressed as

$$|V_{IF}| = g_C|V_{REF}||V_{RES}|\cos(0) = g_C|V_{REF}||V_{RES}|, \tag{8-1}$$

where g_C is the mixer conversion factor. The conversion loss of the mixer is expressed as

$$L_C = 10log_{10}\frac{available\ RF\ input\ power}{available\ IF\ output\ power} = 10log_{10}\frac{P_{RES}}{P_{IF}}. \tag{8-2}$$

The measured conversion loss of the mixer for a 2.14 dBm LO port power was $L_C = 5.9$ dB, which corresponds to a voltage gain of $|V_{IF}|/|V_{RES}| = 0.507$. Therefore, the mixer conversion factor, g_C, becomes

$$g_C = \frac{|V_{IF}|}{|V_{RES}|}\frac{1}{|V_{REF}|} = \frac{0.507}{0.286} = 1.77.$$

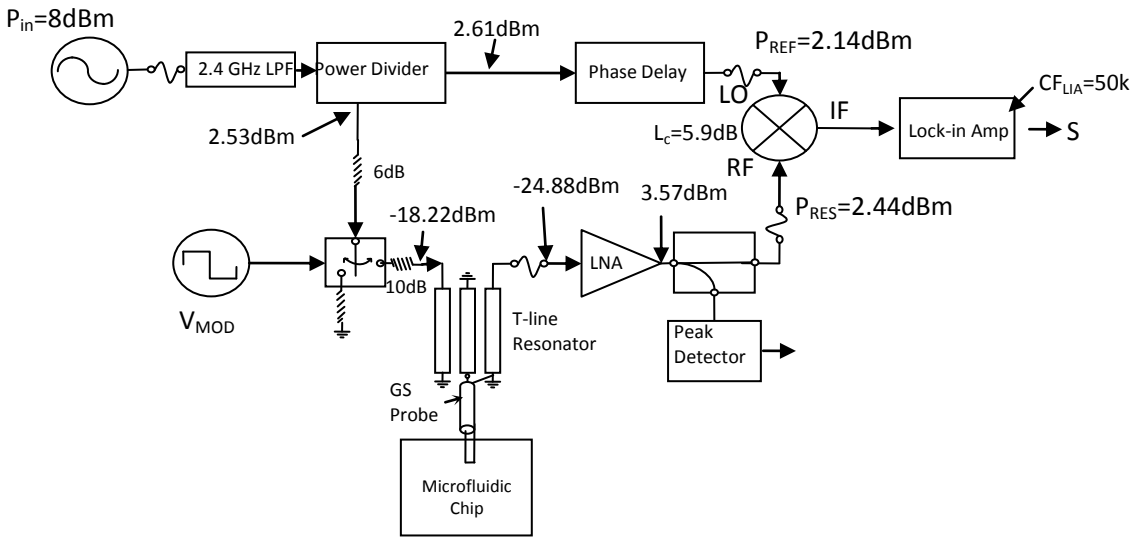

Figure 8-10: Sensor schematic showing power levels and gains.

Before solving for the real part of the permeability, the change in inductance is estimated, based on Eq. 3-8, as

$$S \cong G|V_{REF}||V_{RES}|\left(\frac{\partial \varphi}{\partial L}\right)|_{f_o}(\Delta L).$$

The gain, G, representing the product of the conversion factor of the mixer and the scaling factor of the lock-in-amplifier (LIA), is

$$G = g_C g_{LIA} = (1.77)(50\text{x}10^3) = 88.5\text{x}10^3.$$

The scaling factor of the LIA, for a 200 μV/V sensitivity, was measured using an oscilloscope, and is also specified in the LIA manual. The rms voltage magnitudes at the mixer are

$$|V_{REF}| = .286\,V,$$

$$|V_{RES}| = .296\,V.$$

From Chapter 7,

$$\frac{\partial \varphi}{\partial L}|_{f_0(Loop\ 2)} \cong 1.4\ x\ 10^{-6}\ \text{rad/fH}.$$

The maximum signal obtained using Loop 2 was approximately 207 mV$\pm$10 mV. The change in inductance for this signal can thus be approximated as

$$(\Delta L) \cong \frac{0.207 \pm 0.01}{(88.5)x10^3(.286)(.296)1.4x10^{-6}}[fH] = 19.7 \cong 20 \pm 1\ [fH].$$

A certain bead flow elevation has to be assumed for this signal in order to relate it to the appropriate simulated magnetic field profile ($|\bar{H}|^2$ profiles previously simulated in Chapter 5), for a current magnitude I = 0.25 mA. A 2.25 μm bead centre elevation is assumed since, in all our experiments, the Dynabeads® were observed to flow very near the channel bottom for low flow rates. The low flow elevation can be attributed to the beads' high mass density, which is approximately 1600 kg/m^3 [Fon05].

From Fig. 5-6, $|H_o|^2$=165 A^{2}m^{-2} for Loop 2, at a 2.25 μm elevation, for a current magnitude, I = 0.25 mA. The real part of the relative magnetic permeability for this single bead can now be approximated using Eq. (4-25):

$$\text{Re}\left\{\frac{(\mu_r - 1)}{(\mu_r + 2)}\right\} \cong \frac{(\mu_r{}' - 1)}{(\mu_r{}' + 2)} = \frac{\Delta L \text{I}^2}{4\pi\mu_o \text{R}^3 {H_o}^2} \cong \frac{(19.7)\text{x}10^{-15}(.25\text{x}10^{-3})^2}{4\pi\mu_o(2.25x10^{-6})^3 165} = 0.042$$

yielding

$$\mu_r' = 1.13.$$

The real part of the susceptibility is therefore

$$\chi_r' = \mu_r' - 1 = 0.13.$$

This value is 0.52 times the dc susceptibility value, $\chi_r = 0.25$, quoted by Dynal Inc. [Red96] and 0.08 times the zero-field dc susceptibility value, $\chi_r(0) = 1.63$ quoted by Fonnum et al. [Fon05]. The susceptibilities for the various beads within a sample are not necessarily uniform and can in fact vary from one bead to the other [Shev07].

The output signals from the sensor, using Loop 1 and Loop 2, were negative due to a 180° phase reversal caused by the phase shifter setting in the reference path of the interferometer. This was confirmed by swapping out the resonator for a quarter-wave resonator and touching down onto a planar open-circuit electrode underneath a water-filled microfluidic channel [Nik09]. The two resonators had measured resonant frequencies within 10 MHz of each other and had transmission phases that had the same slope and were within 20° of each other at 1.5 GHz. The quarter-wave resonator set-up detected capacitance changes, and a negative signal due to passing PSSs was expected. The signal obtained from PSSs using the quarter-wave resonator set-up was positive, however, confirming that there was a phase reversal in our experiments. Therefore, the inductance change caused by each magnetic bead was confirmed to be positive, and adding 180° to the output signal phase was justified.

Estimation of the real part of the relative permeability of the superparamagnetic beads is difficult due to a lack of calibration data for the 4.5 μm magnetic Dynabeads® at 1.5 GHz. The elevation of the bead inside the channel is unknown, making it difficult to know the exact field to which the bead is subjected. In addition, the topographical profile of the two loops was not investigated, and the current densities of the fabricated loops could be different than the loops that were modeled using Comsol®. The electrodes could, for instance, have lips at the edges or have smaller thicknesses at the inner electrode

edges due to the electroplating process. Finally, the beads were considered to be magnetically homogeneous with a radius of 2.25 μm. This represents the full radius of the beads and does not take into account the thickness of the non-magnetic coating. Taking this polystyrene coating into account, and subtracting it from the radius used in Eq. 4-25 would lead to a larger estimate for the real part of the relative magnetic permeability.

The RMS noise of the signal using Loop 2 is approximately 10 mV. A 207 mV signal was related to a change in inductance of 20 fH. Treating the noise as white noise, the sensor resolution for an LIA bandwidth of 42 Hz can be determined as

$$\Delta L_{min}/\sqrt{Hz} = \frac{\left(\frac{10mV}{207mV}\right)(20fH)}{\sqrt{42}} \cong 0.15\ fH/\sqrt{Hz}.$$

Finally, the sensitivity of the sensor is determined as

$$S/\Delta L = G|V_{REF}||V_{RES}|\left(\frac{\partial\varphi}{\partial L}\right)|_{f_o} \cong (88500)(.286)(.296)(1.4x10^{-6}) \cong 10\ mV/\text{fH}.$$

Chapter 9
Conclusion and Recommended Future Work

9.1 Conclusion

An inductance sensor has been developed that is capable of detecting single 4.5 μm superparamagnetic Dynabeads® in flow. As the detection is done in flow, this sensor could be used in many applications requiring automated separation and counting of biological cells. The microfabrication recipe of the electrode is simple and the bench-top microwave components comprising the interferometer can be miniaturized into an integrated circuit (IC). The sensor could be incorporated into a lab-on-a-chip device and could act as a trigger for various on-chip processes. The sensor does not require an external biasing magnetic field, which distinguishes it from many other magnetic-bead sensors. The sensitivity of this sensor is not as good as other technologies such as GMR, spin valve, or hall-effect sensors; however this is a prototype sensor and further signal sensitivity improvements could be expected.

The fabricated microfluidic chip had problems with fluid leakage. The decision not to irreversibly bond the PDMS channel to the glass meant that fluid leaked more easily. However, only one sample of electroplated electrodes provided sufficiently low series resistance, which enabled the detection of single Dynabeads®. Therefore, the PDMS was bonded reversibly to the glass to reuse the good sample repeatedly.

By approximating the M-450 Dynabeads® as homogeneous magnetic spheres with a single effective moment, the time-averaged inductance change caused by a single

magnetic bead was shown through simulations to be proportional to the volume of the bead, the real part of the bead's magnetic Clausius-Mossotti factor, and the square of the applied magnetic field at the centre of the bead to the square of the applied loop electrode current.

Single 4.5 μm Dynabead® detection was achieved using two microfabricated electrodes: one electrode, which had a 5.7 μm width and 2.3 μm spacing, was used to achieve single bead detection with an SNR as high as 14.8 dB for a 280 μm/s bead flow rate; the other electrode loop, which had a 3.4 μm width with 2.8 μm spacing, was used to produce an SNR as high as 26.3 dB for a single bead flowing at 80 μm/s. It was confirmed experimentally that non-magnetic polystyrene beads did not produce any signals. A single magnetic bead attached to a 6 μm PSS produced a 23.8 dB SNR at a 80 μm/s flow rate; in this experiment, the attached polystyrene sphere (PSS) simulated a bioparticle bound to a functionalized magnetic bead.

The real part of the magnetic permeability of a particular 4.5 μm Dynabead® at 1.49 GHz was estimated to be 1.13. The inductance change above the 3.4 μm wide loop was estimated to be 20 ± 1 fH for a bead flowing at an approximate elevation of 2.25 μm. The resolution of the sensor, for an LIA bandwidth of 42 Hz, was approximately $0.15 fH/\sqrt{Hz}$. The overall sensor sensitivity, when terminated by the 3.4 μm wide loop, was $10\ mV$/fH.

9.2 Recommended Future Work

Although this sensor does not distinguish between bound and unbound magnetic beads, this sensor could potentially be modified to provide this distinction. This could be

achieved by employing a gap (open-circuit) electrode capacitance sensor [Fer09, Nik09] in conjunction with this inductance sensor, which would be used to detect the capacitance signature of the passing magnetic bead or bead/bioparticle pair. An unbound bead would produce a known capacitance signature and would not be counted. Alternatively, before detection of the bound magnetic beads, magnetic separation of bound and unbound beads could be achieved by applying a magnetophoretic (MAP) force [Jon95] using planar dc current electrodes and multiple channels [Pam04, Ton01].

The fabrication of the microfluidic chip could be made more robust in the future to prevent fluid leakage. For instance, the microfluidic channels could be fabricated in glass or PDMS and could be irreversibly bonded to the glass substrate. The microwave interferometer has previously been microfabricated on printed-circuit boards by Tim Cabel, demonstrating that the interferometer can be miniaturized, which is an important step toward developing a lab-on-a-chip sensor.

Finally, in order to investigate the magnetic properties of the superparamagnetic beads, different resonators with higher and lower resonant frequencies could be used to achieve the highest possible signal. A separate dc biasing magnetic field could also be used to investigate any change in the signal strength, providing more information on the high frequency magnetic properties of the beads. With further knowledge of the microwave magnetic properties of the superparamagnetic beads together with improved sensor sensitivity, single Dynabeads® smaller than 4.5 μm could potentially be detected in the future.

References

[Cur79] R.E. Curry, H. Heitzman, D.H. Riege, R.V. Sweet, and M.G. Simonsen, "A Systems Approach to Fluorescent Immunoassay: General Principles and Representative Applications," Anal. Sys.Clin.Chem., vol. 25, no. 9, pp. 1591-1595, 1979.

[Du10] L. Du, J. Zhe, J.E. Carletta, and R.J. Veillette, "Inductive Coulter counting: detection and differentiation of metal wear particles in lubricant," Smart Mater. Struct., vol. 19, 057001, 2010; doi:10.1088/0964-1726/19/5/057001.

[Ebe08] D. Eberbeck, A.P. Astalan, K. Petersson, F. Wiekhorst, C. Bergemann, C. Johansson, U. Steinhoff, H. Richter, A. Krozer, and L. Trahms, "AC susceptometry and magnetorelaxometry for magnetic nanoparticle basedbiomolecule detection," IFMBE Proceedings, vol. 22, pp. 2317–2321, 2008.

[Fan95] P.C. Fannin and S.W. Charles, "Frequency of ferromagnetic resonance in ferrofluids," Phys. Rev. B, vol. 52, no. 22, pp. 16055-16057, 1995.

[Fan99] P.C. Fannin, P.A. Perov, and S.W. Charles, "Complex susceptibility measurements of magnetic fluids over the frequency range 50 MHz to 18 GHz," J. Phys. D: Appl. Phys., vol. 32, pp. 1583-1586, 1999.

[Fan06] P.C. Fannin, L. Cohen-Tannoudji, E. Bertrand, A.T. Giannitsis, C. Mac Oireachtaigh, and J. Bibette "Investigation of the complex susceptibility of magnetic beads containing maghemite nanoparticles," J. Magn. Magn.Mater., vol. 303, pp. 141-152, 2006.

[Fer09] G.A. Ferrier, S.F. Romanuik, D.J. Thomson, G.E. Bridges, and M.R. Freeman,"A microwave interferometric system for simultaneous actuation and detection of single biological cells," Lab Chip, vol. 9, pp. 3406–341, 2009; doi: 10.1039/b908974.

[Fon05] G. Fonnum, C. Johansson, A. Molteberg, S. Mørup, and E. Aksnes, "Characterization of Dynabeads by magnetization measurements and Mössbauer spectroscopy," J. Magn. Magn.Mater., vol. 293, pp. 41-47, 2005.

[Fuh00] C.B. Fuh, L.Y. Lin, and M.H. Lai, "Analytical magnetophoresis of magnetically susceptible particles," Journ.Chromat.A, vol. 874, pp. 131–142, 2000.

[Gas04] P.R.C. Gascoyne, and J.V. Vykoukal, "Dielectrophoresis-Based Sample Handling in General-Purpose Programmable Diagnostic Instruments," Proceedings of the IEEE, vol. 92, no. 1, 2004.

[Gra93] P. Gravesen, J. Branebjerg, and O.S. Jensen, "Microfluidics−a review," J. Micromech. Microeng., vol. 3, pp. 168-182, 1993.

[Hao11] L. Hao, C. Assman, J.C. Gallop, D. Cox, F. Ruede, O. Kazakova, P. Josephs-Franks, D. Drung, and T. Schurig, "Detection of single magnetic nanobead with a nano-superconducting quantum interference device," Appl. Phys. Lett., vol. 98, 092504, 2011; doi: 10.1063/1.3561743.

[Hsi07] I.M. Hsing, Y. Xu, and W. Zhao, "Micro- and Nano- Magnetic Particles for Applications in Biosensing," Electoanal, vol. 19, no. 7-8, pp. 755-768, 2007.

[Jac75] J.D. Jackson, "Time-Varying Fields, Maxwell Equations, Conservation Laws," in *Classical Electrodynamics*, 2nd ed., New York: Wiley, 1975, ch. 6, sect. 6.2, pp. 213-217.

[Jon95] T.B. Jones, "Dielectrophoresis and Magnetophoresis," in *Electromechanics of Particles.* New York: Cambridge University Press, 1995, ch. 3, sec. 3.5, pp. 62-74.

[Kal03] Y.P. Kalmykov and S.V. Titov, "Calculation of Longitudinal Susceptibility of Superparamagnetic Particles," Phys. Sol. Stat., vol. 45, no. 11, pp. 2140-2146, 2003.

[Kaz07] O. Kazakova, J.Gallop, G. Perkins, and L. Cohen, "Scanned micro-Hall microscope for detection of biofunctionalized magnetic beads," Appl. Phys. Lett., vol. 90, 162502, 2007.

[Kaz10] O. Kazakova, V. Panchal, J. Gallop, P. See, D.C. Cox, M. Spasova, and L.F. Cohen, "Ultrasmall particle detection using a submicron Hall sensor," J. Appl. Phys., vol. 107, 09E708, 2010; doi:10.1063/1.3360584.

[Kie07] J. Kiely, P. Hawkins, P. Wraith and R. Luxton, "Paramagnetic particle detection for use with an immunoassay based biosensor," IET Sci. Meas. Technol., vol. 1, no. 5, pp. 270-275, 2007.

[Koh09] I. Koh and L. Josephson, "Magnetic Nanoparticle Sensors," Sensors, vol. 9, pp. 8130-8145; doi: 10.3390/s91008130.

[Lan04] G. Landry, M. Miller, B. Bennett, M. Johnson, and V. Smolyaninova, "Characterization of single magnetic particles with InAs quantum-well

Hall Devices," Appl. Phys. Lett., vol. 85, no. 20, pp. 4693-4695, 2004; doi: 10.1063/1.1827328.

[Lou09] J. Loureiro, R. Ferreira, S. Cardoso, P. P. Freitas, J. Germano, C. Fermon, G. Arrias, M. Pannetier-Lecoeur, F. Rivadulla, and J. Rivas, "Toward a magnetoresistive chip cytometer: Integrated detection of magnetic beads flowing at cm/s velocities in microfluidic channels," Appl. Phys. Lett., vol. 95, 034104, 2009; doi: 10.1063/1.3182791.

[Mar09] D. Mark S. Haeberle, G. Roth, F.v. Stetten, and R.Zengerlez, "Microfluidic lab-on-a-chip platforms: requirements, characteristics and applications," Chem. Soc. Rev., vol. 39, pp. 1153-1182, 2010; doi: 10.1039/b820557b.

[Meg05] M. Megens and M. Prins, "Magnetic biochips: a new option for sensitive diagnostics," J. Magn. Magn.Mater., vol. 293, pp. 702-708, 2005.

[Mik05] Christian Mikkelsen and HenrikBruus, "Microfluidic capturing-dynamics of paramagnetic bead suspensions," Lab Chip, vol. 5, pp. 1293–1297, 2005.

[Mit01] Peter Mitchell, "Microfluidics—downsizing large-scale biology," Nat. Biotechnol., vol. 19, pp. 717-721, 2001.

[Neel49] L. Néel, "Théorie du traînage magnétique des ferromagnétiques en grains fins avec applications aux terres cuites". Ann. Géophys vol. 5, pp. 99–136, 1949.

[Neu07] A.A. Neurauter, M. Bonyhadi, E. Lien, L. Nøkleby, E. Ruud, S. Camacho, and T. Aarvak, "Cell Isolation and Expansion

UsingDynabeads®," AdvBiochem Engin/Biotechnol, vol.106, pp. 41–73, 2007; doi 10.1007/10_2007_072.

[Nik07] P.I. Nikitin, P.M. Vetoshko, and T.I. Ksenevich, "New type of biosensor based on magnetic nanoparticle detection," J. Magn.Magn.Mater., vol. 311, pp. 445-449, 2007.

[Nik09] M. Nikolic-Jaric, S.F. Romanuik, G.A. Ferrier, G.E. Bridges, M. Butler, K. Sunley, D.J. Thomson, and M.R. Freeman, "Microwave frequency sensor for detection of biological cells in microfluidic channels," Biomicrofluidics, vol. 3, 034103, 2009.

[Nik10] M. Nikolic-Jaric, "Automated Low Pressure Microfluidic Pumping System," [Online document], 2010 June. 7 (V1.0), [accessed 2011 Nov. 15], Available: https://www.cmc.ca/en/WhatWeOffer/Products/CMC-00200-00924.aspx.

[Pam04] N. Pamme and A. Manz, "On-Chip Free-Flow Magnetophoresis: Continuous Flow Separation of Magnetic Particles and Agglomerates," Anal. Chem., vol. 76, pp. 7250-7256, 2004.

[Per03] A. H. Peruski and L. F. Peruski Jr., "Immunological Methods for Detection and Identification of Infectious Disease and Biological Warfare Agents," Clin.Diagn. Lab. Immunol., vol. 10, no. 4, pp. 506–613, 2003.

[Pil10] M.A. Pilapil, "Systematic Development and Characterization of a Polypyrrole Hybrid for Dynamic Random Access Memory," M.Sc. Thesis, University of Manitoba, 2010.

[Poz98a] D.M. Pozar, "Electromagnetic Theory," in *Microwave Engineering,* 2nd ed. New York: Wiley, 1998, ch. 1, sec. 1.6, pp. 26-30.

[Poz98b] D.M. Pozar, "Microwave Resonators," in *Microwave Engineering,* 2nd ed. New York: Wiley, 1998, ch. 6, sec. 6.2, pp. 306-313.

[Rai75] Y. L. Raikher and M.I. Shliomis, "Theory of dispersion of the magnetic susceptibility of fine ferromagnetic particles," Sov. Phys. JETP, vol. 40, no. 3, pp. 526-532, 1975.

[Red96] S. Reddy, L.R. Moore, L. Sun, M. Zborowski, and J.J. Chalmers, "Determination of the magnetic susceptibility of labeled particles by video imaging," Chem. Eng. Sci., vol. 51, no.6, pp. 947-956, 1996.

[Saf99] I. Safarik and M. Safarikova, "Use of magnetic techniques for the isolation of cells," J. Chromatogr. B, vol. 722, pp. 33-53, 1999.

[Tam08] C.R. Tamanaha, S.P. Mulvaney, J.C. Rife, and L.J. Whitman., "Magnetic labeling, detection, and system integration," Biosens.Bioelectron., vol. 24, pp. 1–13, 2008.

[Ton01] M. Tondra, M. Granger, R. Fuerst, M. Porter, C. Nordman, J. Taylor, and S. Akou, "Design of Integrated Microfluidic Device for Sorting Magnetic Beads in Biological Assays," IEEE Tran. Magn., vol. 37, no. 4, pp. 2621-2623, July, 2001.

[Tran01] T.D. Tran, D.R. Oliver, D.J. Thomson and G.E. Bridges, "Zeptofarad (10-21 F)
resolution capacitance sensor for scanning capacitance microscopy", *Rev. Sci. Inst.*, vol. 72, pp. 2618-2623, 2001.

[Vij03] A. Vijay and A. Venkataraman, "Dielectric, electrical and infrared studies of γ-Fe2O3 prepared by combustion method," Bull. Mater. Sci., vol. 26, no. 4, pp. 391–396, 2003.

[Wan09] H. Wang, Y. Chen, A. Hassibi, A. Scherer, and A. Hajimiri, "A frequency-shift CMOS magnetic biosensor array with single-bead sensitivity and no external magnet," presented at the IEEE International Solid-State Circuits Conference, 2009.

[Wil05] D. Wild, *The Immunoassay Handbook, 3rd ed.* Oxford, UK: Elsevier, 2005.